RUNX1 marks a luminal castration resistant lineage established at the onset of prostate development

AUTHORS

Renaud Mevel[1], Ivana Steiner[2], Susan Mason[3], Laura C.A. Galbraith[3], Rahima Patel[1], Muhammad ZH Fadlullah[1], Imran Ahmad[3,4], Hing Y. Leung[3,4], Pedro Oliveira[5], Karen Blyth[3,4], Esther Baena[2,6], Georges Lacaud[1,7]

AFFILIATIONS

[1] Cancer Research UK, Stem Cell Biology Group, Cancer Research UK Manchester Institute, The University of Manchester, Alderley Park, Alderley Edge, Macclesfield, SK10 4TG, UK.

[2] Cancer Research UK, Prostate Oncobiology Group, Cancer Research UK Manchester Institute, The University of Manchester, Alderley Park, Alderley Edge, Macclesfield, SK10 4TG, UK.

[3] Cancer Research UK Beatson Institute, Bearsden, Glasgow, G61 1BD, UK.

[4] Institute of Cancer Sciences, College of Medical, Veterinary and Life Sciences, University of Glasgow, Bearsden, Glasgow, G61 1QH, UK.

[5] Department of Pathology, The Christie NHS Foundation Trust, Manchester, UK.

[6] Belfast-Manchester Movember Centre of Excellence, Cancer Research UK Manchester Institute, The University of Manchester, Alderley Park SK10 4TG, UK.

[7] Correspondence: georges.lacaud@manchester.ac.uk

Phone: +44 (0) 161 446 6058, Fax: +44 (0) 161 446 3109

ABSTRACT

The characterization of prostate epithelial hierarchy and lineage heterogeneity is critical to understand its regenerative properties and malignancies. Here, we report that the transcription factor RUNX1 marks a specific subpopulation of proximal luminal cells (PLCs), enriched in the periurethral region of the developing and adult mouse prostate, and distinct from the previously identified NKX3.1^{+} luminal castration resistant cells. Using scRNA-seq profiling and genetic lineage tracing, we show that RUNX1^{+} PLCs are unaffected by androgen deprivation, and do not contribute to the regeneration of the distal luminal compartments. Furthermore, we demonstrate that a transcriptionally similar RUNX1^{+} population emerges at the onset of embryonic prostate specification to populate the proximal region of the ducts. Collectively, our results reveal that RUNX1^{+} PLCs is an intrinsic castration-resistant and self-sustained lineage that emerges early during prostate development and provide new insights into the lineage relationships of the prostate epithelium.

35 **INTRODUCTION**

36 The prostate is a glandular organ of the mammalian male reproductive system. In mice,
37 prostate development starts during embryogenesis at embryonic day (E) 15.5-16.5 with the
38 emergence of the first prostatic buds from the rostral end of the urogenital sinus (UGS) (Bhatia-
39 Gaur et al., 1999; Georgas et al., 2015; Keil et al., 2012; Toivanen & Shen, 2017). These initial
40 buds grow into the surrounding mesenchyme to develop postnatally and through puberty into
41 a branched ductal network organized in distinct pairs of lobes, known as the anterior prostate
42 (AP), dorsolateral prostate (DLP) and ventral prostate (VP) (Sugimura et al., 1986a). Each lobe
43 has distinct branching patterns, histopathological characteristics, and is thought to contribute
44 differently to the physiological function of the prostate. The differentiated epithelium of the
45 adult prostate gland is mainly composed of basal and luminal cells, interspersed with rare
46 neuroendocrine cells (Shen & Abate-Shen, 2010; Toivanen & Shen, 2017; Y. Wang et al., 2001).
47 Luminal cells form a layer of polarized tall columnar cells that depend on androgen signaling
48 and produce the prostatic secretions. Basal cells act as a supportive layer located between the
49 luminal cells and the surrounding stroma.

50 Despite being mostly quiescent under homeostatic conditions, the prostate gland
51 encompasses incredible plasticity. In mice, surgical castration-induced prostate involution has
52 proven an invaluable tool to identify progenitor castration-resistant cell populations,
53 characterized by their ability to survive in the absence of androgens, and to fully regenerate an
54 intact adult prostate after re-administration of testosterone (Barros-Silva et al., 2018; Kwon et
55 al., 2016; McAuley et al., 2019; Tsujimura et al., 2002; B. Wang et al., 2015; X. Wang et al.,
56 2009; Yoo et al., 2016). Such plasticity has also been shown in defined experimental conditions

57 to stimulate regenerative properties of epithelial subpopulations, including transplantations
58 (Barros-Silva et al., 2018; Burger et al., 2005; Lawson et al., 2007; Lukacs et al., 2010;
59 Richardson et al., 2004; X. Wang et al., 2009; Xin et al., 2005; Yoo et al., 2016), injury repair
60 (Centonze et al., 2020; Horton et al., 2019; Kwon et al., 2014; Toivanen et al., 2016), and
61 organoid assays (Chua et al., 2014; Höfner et al., 2015; Karthaus et al., 2014). In addition,
62 several studies have proposed that progenitor populations with distinct physiological roles and
63 regenerative capacity reside at different locations within the prostate (Burger et al., 2005;
64 Crowell et al., 2019; Goldstein et al., 2008; Goto et al., 2006; Kwon et al., 2016; Leong et al.,
65 2008; McNeal, 1981; Tsujimura et al., 2002). However, the precise cellular hierarchy and how it
66 is established during development remains controversial.
67 RUNX transcription factors (TF) are master regulators of lineage commitment and cell
68 fate (Mevel et al., 2019). In particular, RUNX1 is essential for the ontogeny of the hematopoietic
69 system and alterations of RUNX1 have been associated with a broad spectrum of hematological
70 malignancies. Interestingly, increasing evidence implicates RUNX1 in the biology and pathology
71 of hormone-associated epithelia (Lie-A-Ling et al., 2020; Riggio & Blyth, 2017; Scheitz &
72 Tumbar, 2013), including breast (Browne et al., 2015; Chimge et al., 2016; Ferrari et al., 2014;
73 van Bragt et al., 2014), uterine (Planagumà et al., 2004, 2006), ovarian (Keita et al., 2013), and
74 prostate cancers (Banach-Petrosky et al., 2007; Scheitz et al., 2012; Takayama et al., 2015).
75 Despite the documented importance of RUNX TFs and reports of RUNX1 in PCa, its expression
76 in the normal prostate gland during development, homeostasis, and regeneration has not been
77 explored.

78 In this study, we found that *Runx1* marks a discrete subset of luminal cells located in the
79 proximal region of the prostatic ducts. Using mouse models, combined with lobe-specific single-
80 cell transcriptomic profiling of adult, castrated, and developing prostates, we show that RUNX1^{+}
81 proximal luminal cells represent a distinct lineage established at the onset of prostate
82 development, displaying intrinsic castration-resistant and self-sustaining properties.

83 **RESULTS**

84 **RUNX1 marks a subpopulation of prostate proximal luminal cells (PLCs)**

85 We initially sought to characterize the expression pattern of *Runx1* in adult mouse
86 prostate. While RUNX1 was detected in basal cells at multiple spatial locations, its expression
87 was specifically high in a subset of luminal cells found in the proximal region of all three lobes,
88 also known as periurethral (Figures 1A, B; Figure 1–figure supplement 1A, B). Sections were co-
89 stained with NKX3.1, a master regulator of prostate development broadly expressed in luminal
90 cells. Using quantitative image-based cytometry (QBIC), we found that RUNX1 and NKX3.1 had
91 a largely mutually exclusive expression pattern, with a sharp transition from RUNX1^{+} NKX3.1^{-} to
92 RUNX1^{-} NKX3.1^{+} cells in the proximal region (Figures 1A, B; Figure 1–figure supplement 1A, B).
93 These proximal luminal cells had a unique histological profile, with a compact organization,
94 intense nuclear hematoxylin staining, and increased nuclear-to-cytoplasmic ratio (Figure 1–
95 figure supplement 1C). In contrast, distal luminal cells had a large cytoplasm with intense pink
96 eosin staining, likely reflecting their secretory function. These observations suggest that RUNX1
97 marks a subset of proximal luminal cells, distinct from the abundant NKX3.1^{+} luminal population
98 lining the rest of the prostate epithelium.

99 The proximal site of the prostate has been proposed to be enriched in cells with
100 stem/progenitor properties (Goldstein et al., 2008; Kwon et al., 2016; Tsujimura et al., 2002;
101 Yoo et al., 2016). In order to study the regenerative potential of *Runx1* expressing cells *ex vivo*,
102 we took advantage of isoform-specific fluorescent reporter mouse models of *Runx1* (Draper et
103 al., 2018; Sroczynska et al., 2009). *Runx1* expression is controlled by two promoters, P1 and P2,
104 that respectively drive the expression of the *Runx1c* and the *Runx1b* isoform (Mevel et al.,

105 2019). We found that *Runx1* expression in the prostate was exclusively mediated by the
106 proximal P2 promoter, in up to 30% of all epithelial EPCAM$^+$ prostate cells (Figure 1–figure
107 supplement 2A-C). Flow-cytometry profiling confirmed the enrichment of P2-*Runx1*:RFP in both
108 basal (EPCAM$^+$ CD49f^{high}) and luminal (EPCAM$^+$ CD24^{high}) lineages of the proximal compared to
109 the distal prostate (Figures 1C, D; Figure 1–figure supplement 2D). Mirroring our QBIC spatial
110 analysis (Figure 1–figure supplement 1B), P2-*Runx1*:RFP was also detected in a large fraction of
111 the VP epithelium (Figure 1–figure supplement 2D).

112 We therefore used the P2-*Runx1*:RFP mouse line to isolate *Runx1* positive (RFP$^+$) and
113 negative (RFP$^-$) epithelial cells from the basal and luminal compartments of all three prostate
114 lobes and evaluated their regenerative potential in organoid culture assays (Drost et al., 2016)
115 (Figure 1E). The proximal and distal regions of the AP were analyzed separately. In line with
116 previous reports, basal cells were more efficient at forming organoids compared to all luminal
117 fractions (Drost et al., 2016, Kwon et al., 2015). Importantly, in the luminal fraction, proximal
118 RFP$^+$ luminal cells of the AP consistently displayed higher Organoid Formation Capacity (OFC)
119 than the RFP$^-$ fraction (Figure 1F). Luminal RFP$^+$ sorted cells of the DLP and VP also had a greater
120 OFC than RFP$^-$ cells (Figure 1–figure supplement 3A). In contrast, no significant differences in
121 OFC were observed between basal enriched subsets and distal luminal RFP$^+$ and RFP$^-$ cells.
122 Brightfield assessment revealed that virtually all organoids had a 'solid' aspect, except for the
123 predominantly 'hollow' organoids derived from proximal RFP$^+$ luminal cells (Figure 1–figure
124 supplement 3B). To further characterize their lineage potential, we classified organoids into
125 three types based on the expression of specific lineage markers: unipotent "basal-like" Keratin
126 5$^+$ (K5$^+$), unipotent "luminal-like" Keratin 8$^+$ (K8$^+$), or multipotent K5$^+$ K8$^+$ (Figures 1G, H; Figure

127 1–figure supplement 3C). Interestingly, AP proximal luminal RFP$^+$ derived organoids were
128 predominantly small unipotent K8$^+$, while the remainder fraction mainly gave larger unipotent
129 K5$^+$ organoids (Figures 1H; Figure 1–figure supplement 3D-E). Few multipotent K5$^+$ K8$^+$
130 organoids were also identified in nearly all populations.

131 Together, our results show that RUNX1 marks a specific subset of proximal luminal cells
132 (PLCs), and that its expression in the prostate is mediated by the P2 promoter. RUNX1$^+$ PLCs
133 have a particular predisposition to form unipotent K8$^+$ hollow organoids, suggesting a lineage
134 bias towards the luminal identity, and highlighting differences within the luminal compartment
135 of proximal and distal regions.

136

137 ***Runx1* expressing cells are enriched in the castrated prostate epithelium**

138 In mice, androgen-deprivation can be modelled by surgical castration which leads to
139 prostate regression and enriches for castration-resistant cells (Toivanen & Shen, 2017; Zhang et
140 al., 2018). This process is accompanied by the death of luminal androgen-dependent cells and a
141 small proportion of basal cells (English et al., 1987; Sugimura et al., 1986b). To track changes in
142 *Runx1* expression following androgen withdrawal, we surgically castrated P2-*Runx1*:RFP mice
143 and harvested tissue ≥ 4 weeks post-surgery (Figure 2A). While intact prostates contained 22.8
144 ± 6.0% RFP$^+$ epithelial cells, their frequency increased to 87 ± 6.0% following castration (Figures
145 2B, C). High RUNX1 levels were no longer restricted to the proximal region, and RFP was
146 detected in virtually all basal cells of the AP, DLP and VP, as well as more than 75% of the
147 luminal castration-resistant cells (Figures 2D; Figure 2–figure supplement 1A). RUNX1
148 expressing cells often co-expressed TROP2 (Figure 2E), known to be widely expressed in

149 castrated prostate epithelium (Goldstein et al., 2008; X.-D. Wang et al., 2007). Several
150 castration-resistant luminal populations have been identified in mice (Barros-Silva et al., 2018;
151 Kwon et al., 2016; McAuley et al., 2019; Tsujimura et al., 2002; B. Wang et al., 2015; X. Wang et
152 al., 2009; Yoo et al., 2016), including rare castration-resistant *Nkx3-1* expressing cells (CARNs).
153 Accordingly, we observed low, but detectable, levels of NKX3.1 in some luminal cells, but only
154 occasional RUNX1$^+$ NKX3.1$^+$ luminal cells in the distal regions of the castrated prostate (Figures
155 2D; Figure 2–figure supplement 1B, C). Importantly, the clear transition from RUNX1$^+$ to
156 NKX3.1$^+$ cells identified in the proximal luminal layer of intact mice was conserved after
157 castration (Figure 2D, ii).
158 Together, these results show that RUNX1 is expressed in the majority of the castration-
159 resistant cells. The RUNX1$^+$ NKX3.1$^-$ subset identified in the proximal luminal epithelium of the
160 intact prostate remain NKX3.1$^-$ following castration, supporting the notion that RUNX1$^+$ PLCs
161 constitute a distinct lineage from distal NKX3.1$^+$ cells.
162
163 **scRNA-seq profiling of *Runx1*$^+$ and *Runx1*$^-$ cells in individual lobes of the intact and castrated**
164 **prostate**
165 To further characterize the RUNX1$^+$ and RUNX1$^-$ fractions residing at different
166 anatomical locations of the prostate, we performed droplet-based single cell (sc)RNA-seq. We
167 sorted EPCAM$^+$ RFP$^+$ and RFP$^-$ cells from individually dissected lobes of intact and castrated
168 prostates isolated from P2-*Runx1*:RFP reporter mice (Figure 3A). Sorted populations were
169 multiplexed using MULTI-seq lipid-tagged indices to minimize technical confounders such as
170 doublets and batch effects (McGinnis, Patterson, et al., 2019). We retrieved a total of 3,825

171 prostate epithelial cells from all sorted populations, with a median of 2,846 genes per cell (see
172 Methods; Figure 3–figure supplement 1, 2A-G). We identified 9 *in silico* computed clusters
173 expressing canonical epithelial, basal, and luminal markers (Figure 3–figure supplement 2H-J). A
174 large population of basal cells was annotated by merging 3 tightly connected subclusters
175 broadly expressing *Krt5*, *Krt14,* and *Trp63* (Figures 3B-D; Figure 3–figure supplement 2E, J).
176 Luminal populations expressed surprisingly heterogeneous levels of canonical luminal markers
177 such as *Cd26*/*Dpp4, Cd24a*, *Krt8, and Krt18* (Figure 3–figure supplement 2I). We annotated
178 those distinct clusters as Luminal-A (Lum-A), Lum-B, Lum-C, Lum-D, Lum-E and Lum-F (Figure
179 3B). Differential gene expression analysis revealed genes strongly associated with each luminal
180 subpopulation (Figures 3C, 3D; Figure 3–figure supplement 3A; Supplementary file 2).
181 Initially, we sought to evaluate the effect of androgen withdrawal on lobe-specific
182 cellular heterogeneity. Lum-A/B/C/D were largely enriched in luminal cells originating from
183 intact prostates, whereas Lum-E/F contained mainly castrated luminal cells (Figures 3E; Figure
184 3–figure supplement 3B). Interestingly, Lum-A/C/F mainly contained VP cells, while Lum-B/D/E
185 had a majority of AP and DLP cells, indicating that the lobular identity of luminal cells in the
186 intact prostate is conserved following castration (Figures 3F; Figure 3–figure supplement 3C).
187 These results suggest that a subset of intact Lum-A/C might undergo partial reprogramming
188 during castration-induced regression and gives rise to the Lum-F cluster. Similarly, surviving
189 Lum-B/D may predominantly reprogram into Lum-E cells upon castration. Alternatively, the
190 small fraction of intact cells observed in Lum-E and Lum-F clusters might give rise to the
191 expanded Lum-E/F clusters upon castration. In contrast to luminal cells, castrated basal cells
192 were minimally affected by androgen-deprivation and clustered together with intact basal cells

193 (Figure 3E). Overall, these results highlight the dramatic changes occurring upon androgen
194 deprivation in the representation of distinct luminal subpopulations.
195
196 ***Runx1* expressing luminal cells are transcriptionally similar to castration-resistant cells**
197 We next specifically focused our attention on RUNX1$^+$ luminal cells. The Lum-D cluster
198 predominantly consisted of AP derived RFP$^+$ cells, as well as a small number of RFP$^+$ DLP and VP
199 cells (Figure 3F, H; Figure 3–figure supplements 2E, 3B, 3C). High *Runx1* expression in Lum-D
200 correlated with higher levels of *Tacstd2*/*Trop2*, Ly6 family members as well as *Runx2* (Figures
201 3D, G; Figure 3–figure supplements 3D, E). In contrast, *Runx1* was barely detected in clusters
202 Lum-B/C which expressed high levels of *Nkx3-1* while Lum-A cells expressed low levels of both
203 *Runx1* and *Nkx3-1*. These results suggest that the Lum-D cluster corresponds to the distinct
204 RUNX1$^+$ luminal cells identified in the proximal region of all three prostate lobes (Figure 1).
205 To further characterize the specificities of those populations, we performed gene
206 ontology analysis. In line with the secretory role of distal luminal cells, clusters Lum-A/B/C were
207 enriched in enzymatic activity and protein synthesis functions. In contrast, the Lum-D cluster
208 was enriched in terms related to epithelial developmental processes, similar to Lum-E/F (Figure
209 3–figure supplements 4A-I). This was supported by partition-based graph abstraction (Wolf et
210 al., 2019), which uncovered a strong degree of connectivity between the mainly intact Lum-D
211 and castrated Lum-E population (Figure 3B). Additionally, the Lum-D cluster contained a small,
212 but defined, subpopulation of castrated epithelial cells, suggesting the preservation of its
213 identity upon androgen deprivation (Figures 3E, F). In this population, we found very few genes
214 significantly differentially expressed between intact and castrated cells (n=103; Supplementary

215 file 3). As expected, androgen-regulated genes including *Psca* and *Tspan1* were downregulated
216 in the castrated subset, while strong contributors of the Lum-D identity such as *Tacstd2*/*Trop2*,
217 *Krt4* and *Runx1* did not vary (Figure 3–figure supplement 4J). These observations further
218 support the hypothesis that Lum-D/RUNX1^{+} PLCs maintain their identity following androgen-
219 deprivation.

220 Overall, our single-cell transcriptomic analysis highlighted a vast degree of
221 heterogeneity within and between the luminal compartments of both intact and castrated
222 mouse prostates. The tight transcriptional relationship observed between high *Runx1*
223 expressing clusters Lum-D and Lum-E/F suggest that the Lum-D population, which corresponds
224 to PLCs, may contain intrinsically castration-resistant luminal cells
225

226 **Lineage-tracing of *Runx1* expressing cells establishes the intrinsic castration resistant**
227 **properties of the proximal luminal lineage**

228 To determine if RUNX1^{+} PLCs were enriched in castration-resistant cells, we combined
229 prostate regression-regeneration assays with genetic lineage-tracing using *Runx1*$^{\text{mER-CRE-mER}}$
230 *Rosa*$^{\text{flox-stop-flox-tdRFP}}$ mice (Luche et al., 2007; Samokhvalov et al., 2007), henceforth *Runx1*^{CreER}
231 *Rosa26*$^{LSL\text{-}RFP}$ (Figure 4A). Using this model, we could genetically label an average of 4.70 ± 2.8%
232 prostate epithelial *Runx1* expressing cells with RFP upon tamoxifen injection (Figures 4B, C;
233 Figure 4–figure supplement 1A). This corresponded to 0.54 ± 0.2‰ of the total epithelium
234 (Figure 4E). Consistent with the expression pattern of *Runx1*, the majority of labelled cells were
235 located in the proximal region of the prostate (Figure 4C), and co-expressed Keratin 4 (K4)
236 (Figure 4–figure supplements 1D, E), previously found enriched in Lum-D cells (Figure 3D).

237 Following surgical castration, we found that the absolute number of RFP$^+$ marked cells
238 remained stable (Figure 4–figure supplements 1C, D). However, the frequency of RFP$^+$ cells in
239 the epithelial compartment increased by ~4.3 fold (Figures 4E; Figure 4–figure supplement 1B)
240 indicating that *Runx1* expressing cells have an enhanced capacity to survive castration
241 compared to *Runx1* negative cells. Next, we investigated whether these intrinsically castration-
242 resistant *Runx1* expressing cells were involved in epithelial regeneration upon testosterone
243 addback (Figure 4B, bottom). Surprisingly, only 0.71 ± 0.2‰ RFP$^+$ epithelial cells were found in
244 the regenerated prostate, which was comparable to the intact state (Figures 4E; Figure 4–figure
245 supplements 1B-D). Although the majority of RFP$^+$ clones consisted of single cells, we did
246 observe a minor ~2-fold increase in the frequency of larger clones (2-4 cells) after regeneration,
247 highlighting a modest contribution of RFP labeled cells during prostate regeneration (Figures 4F,
248 G). We found that most RFP marked cells were luminal K8$^+$ in intact, castrated, and regenerated
249 prostates (Figures 4F, H), with only a few basal K5$^+$ RFP$^+$ cells detected in distal areas (Figure
250 4F). Strikingly, more than 90% of all RFP$^+$ cells remained negative for NKX3.1 in all experimental
251 arms (Figure 4I).
252 Thus, these results indicate that RFP$^+$ cells, including PLCs, are mostly unaffected by
253 fluctuations in androgen levels during regression-regeneration assays. RUNX1 expression marks
254 intrinsically castration-resistant luminal cells that do not contribute substantially to the
255 expansion of luminal NKX3.1$^+$ cells during prostate regeneration.
256
257 ***Runx1* marks proximal cells during prostate development**

258 Given the singular identity of proximal luminal *Runx1* expressing cells in the adult
259 prostate, we then asked if this luminal lineage was already emerging during prostate
260 development. At E18.5, once the first prostate buds have emerged, RUNX1 was mainly found in
261 the K8^{high} inner layers of the stratified urogenital epithelium (UGE) (Figure 5A). Interestingly,
262 these cells also co-expressed K4 (Figure 5–figure supplement 1A), previously found in the Lum D
263 population (Figure 3D), as well as LY6D, recently shown to mark a subset of adult luminal
264 progenitors (Barros-Silva et al., 2018) (Figure 5–figure supplement 1B). In contrast, RUNX1
265 expression was low in p63^{+} and K5^{+} cells, either lining the outer UGE or found in the tips of
266 premature NKX3.1^{+} prostate buds (Figures 5A-C). At postnatal day 14 (P14), a prepubescent
267 stage when most of the initial branching events have already occurred (Sugimura et al., 1986a;
268 Tika et al., 2019), RUNX1 was broadly expressed in the proximal region (Figure 5D), mainly in
269 K4^{+} luminal cells and in some K5^{+} or p63^{+} cells (Figure 5–figure supplement 1C-E). Conversely,
270 NKX3.1^{+} cells were found in distal locations, largely distinct from RUNX1^{+} cells. The specific
271 spatial expression pattern of RUNX1 in proximal luminal cells, largely mutually exclusive with
272 NKX3.1, suggests that these two transcription factors already mark distinct cellular lineages
273 during embryonic prostate organogenesis.
274 To study the dynamic emergence of RUNX1^{+} cells during prostate development, we
275 utilized an explant culture system (Berman et al., 2004; Doles et al., 2005; Kruithof-de Julio et
276 al., 2013; Lopes et al., 1996). Dissected E15.5 UGS were cultured for up to 7 days in the
277 presence of dihydrotestosterone (Figures 5E, F). Bud formation was initiated within 2 days of
278 culture (Figure 5G) and composed of a double positive K5^{+} K8^{+} stratified epithelium, partially
279 diversifying by day 7 (Figure 5–figure supplement 2A, B). On day 0 (E15.5), RUNX1 was detected

280 at the rostral end of the UGE, particularly within the inner layers of the stratified epithelium.
281 After 1 day in culture, NKX3.1 expression emerged in RUNX1$^+$ cells located in the outer layers of
282 the UGE, while defined budding was yet to be observed. On day 2, NKX3.1$^+$ prostate buds were
283 evident and had reduced or absent RUNX1 expression. This pattern was conserved in the
284 mature explant, in which distal tips were mainly NKX3.1$^+$, whereas the proximal area remained
285 RUNX1$^+$ (Figures 5G, H), and co-expressed LY6D and K4 (Figure 5–figure supplements 2C, D).
286 Cellular proliferation marked by Ki67 was more substantial in distal regions, suggesting that
287 most of the expansion did not take place in the RUNX1$^+$ compartment (Figure 5–figure
288 supplement 2E).
289 These results suggest that prostate budding originates from a subset of cells located in
290 the outer layers of the stratified UGE, transiently marked by RUNX1 and NKX3.1. During
291 embryonic prostate development, *Runx1* expression is already primarily confined to the
292 proximal region of the prostatic ducts, in a distinct compartment from NKX3.1$^+$ cells.
293
294 **scRNA-seq of explant cultures reveals the specification of the proximal luminal lineage during**
295 **embryonic prostate development**
296 The characterization by immunostainings of continuous developmental processes is
297 generally constrained to a small number of markers at a time. To further study the specification
298 of RUNX1 and NKX3.1 lineages, we performed scRNA-seq on UGS explant cultures collected at
299 successive time points: E15.5 (D0), day 1 (D1), day 3 (D3), and day 6 (D6) (Figure 6A). After data
300 processing, 3,937 developing prostatic cells were retained, with a median of 3,608 genes per
301 cell (see Methods; Figure 6–figure supplement 1).

302 Visualization of the dataset using a force-directed layout highlighted the progressive
303 cellular diversification taking place from D0 to D6 (Figure 6B). Cellular populations were divided
304 into 9 clusters, annotated C0 to C8 (Figures 6C-E). C0/C1 contained the majority of D0 and D1
305 derived cells, while C2-C8 emerged and expanded at later time points. Due to the primitive
306 nature of the UGE at these time points, the classical basal and luminal lineages were not fully
307 established yet (Figures 6F; Figure 6–figure supplements 2A-E; Supplementary file 4).
308 Nevertheless, C4-C6 had a more pronounced 'basal' identity compared to the other clusters.
309 *Krt5*/*Krt14* marked mainly C4, and additional basal markers including *Trp63, Dcn*, *Apoe,* or *Vcan*
310 were higher in C5/C6. Overall, known regulators of prostate development (Toivanen & Shen,
311 2017) displayed a variable expression pattern across the different clusters. For example, *Foxa1*
312 and *Shh* were strongly expressed in C0/C1, *Notch1* was higher in C3, and *Sox9* in C7 (Figure 6–
313 figure supplement 2C), highlighting the potential of this dataset to interrogate specific features
314 of prostate development.
315 Consistent with our previous results, *Runx1* was highly expressed in clusters having
316 lower *Nkx3-1* levels, including C0, C1, C2 and C4 (Figure 6G). To determine how these clusters
317 relate to differentiated prostate lineages, we interrogated population-specific gene signatures
318 previously identified in the adult (Figure 3). The 'Basal' signature was enriched across all
319 clusters, especially in C4/C6 (Figures 6I; Figure 6–figure supplement 2F, G). Strikingly, the 'Lum-
320 D' derived signature was highly enriched in C2 compared to all the other adult luminal
321 population signatures, suggesting that the 'Lum-D' fate is determined early during prostate
322 development. The singular identity of C2 was characterized by genes previously found highly

323 expressed in the adult 'Lum-D' population, including *Tacstd2*/*Trop2*, *Krt4*, *Psca*, as well as *Ly6d*
324 and *Nupr1* (Figure 6H; Figure 6–figure supplement 2A).
325 Collectively, our scRNA-seq analysis show that adult 'Lum-D'/PLCs share strong
326 similarities with the unique C2 population identified in embryonic explant cultures. This
327 suggests that the distinct proximal luminal lineage is established at the very onset of prostate
328 specification.
329
330 **RUNX1$^+$ cells contribute to the establishment of the proximal luminal lineage during**
331 **embryonic prostate development**
332 To trace the fate of RUNX1$^+$ cells during embryonic prostate specification, we cultured
333 UGS explants isolated from the *Runx1^{CreER} Rosa26$^{LSL-RFP}$* lineage tracing model. We performed 2
334 pulses of tamoxifen treatment on day 0 and 1 of culture and analyzed the explants on day 2 and
335 day 7 (Figure 7A). The majority of the RFP labeled cells were in the most proximal RUNX1$^+$
336 subset and rarely found in the distal area of the branches, where RUNX1$^-$ cells reside (Figures
337 7B, C). Accordingly, the proportion of RFP$^+$ RUNX1$^+$ cells remained stable between day 2 and 7
338 (Figure 7D). Also, the fraction of RFP$^+$ cells co-expressing p63 remained unchanged throughout
339 the culture (Figure 7–figure supplements 1A-C), while a small fraction diversified into either K5$^+$
340 or K8$^+$ cells (Figure 7–figure supplements 1D, E). The scattered RFP$^+$ RUNX1$^-$ cells detected in
341 distal branches by day 7 often co-expressed NKX3.1 (Figures 7E, F). Overall, this indicates that
342 *Runx1* expressing cells only marginally contribute to the expansion of the NKX3.1 compartment
343 (Figure 7G). Finally, we wondered whether RUNX1$^+$ cells contributed to the establishment of
344 the proximal luminal lineage. We evaluated the proportion of RFP labelled cells co-expressing

345 K4, previously identified as a marker of the developing C2 and adult Lum-D populations (Figures
346 3D and 6H). Interestingly, the fraction of $K4^+$ RFP labeled cells increased from 56.9 ± 10.6% to
347 74.1 ± 3.0% between day 2 and 7 (Figures 7F, G). There was also an increase of RFP^+ cells
348 expressing *Nupr1*, another marker of the C2 cluster (Figure 7–figure supplements 1F-H). Taken
349 together, these results show that only a small subset of *Runx1* expressing cells contributes to
350 the expansion of $NKX3.1^+$ lineage, found in the distal region of the developing prostatic buds.
351 Instead, the majority of *Runx1* expressing cells preferentially remain in the proximal region of
352 the premature buds, where the proximal luminal lineage is established.

353 **DISCUSSION**

354 In this study, we identified RUNX1 as a new marker of a luminal population enriched in
355 the proximal region of the prostatic ducts. By combining scRNA-seq profiling and genetic
356 lineage tracing of *Runx1* expressing cells, we show that RUNX1^{+} PLCs present in the intact
357 prostate constitute a developmentally distinct and intrinsically castration-resistant luminal
358 lineage. We propose that proximal and distal lineages are separate luminal entities from the
359 earliest stages of prostate development. As such, our study provides novel insights into the
360 cellular composition and developmental hierarchy of the mouse prostate epithelium.

361

362 Until the recent advances in single-cell technologies, the prostate epithelial hierarchy
363 was mainly defined based on anatomical features of the basal and luminal layers, their
364 histological characteristics and the expression of a small subset of markers (Shen & Abate-Shen,
365 2010; Toivanen & Shen, 2017). Here we present two comprehensive scRNA-seq dataset
366 covering both the adult and the developing prostate. To our knowledge, this constitutes the
367 first comprehensive single-cell atlas covering both intact and castrated adult mouse prostates,
368 annotated by their lobe of origin. These datasets can be browsed interactively at
369 http://shiny.cruk.manchester.ac.uk/pscapp/. In particular, our adult scRNA-seq dataset
370 highlighted an extensive degree of cellular heterogeneity, in particular within the luminal
371 epithelia. Several studies recently made similar observations either focusing on the AP
372 (Karthaus et al., 2020), the intact prostate (Crowley et al., 2020; Joseph et al., 2020), or both the
373 intact and castrated prostates (Guo et al., 2020). Integration of these multiple datasets will
374 provide a more global view of the transcriptional landscape of the prostate epithelium.

375 Although mainly known as a master regulator of hematopoiesis, RUNX1 is increasingly
376 implicated in hormone-associated epithelia including malignant conditions such as prostate
377 cancer (Banach-Petrosky et al., 2007; Lie-A-Ling et al., 2020; Scheitz et al., 2012; Takayama et
378 al., 2015). Here, we identified a subset of RUNX1$^+$ luminal cells located in the proximal region of
379 the developing and adult prostate, referred to as RUNX1$^+$ PLCs, and corresponding to the Lum-D
380 cluster identified in our adult scRNA-seq dataset. Of note, this subset appears to be the
381 equivalent of the 'L2' (Karthaus et al., 2020) or 'LumP' (Crowley et al., 2020), or 'Lum-C' (Guo et
382 al., 2020) clusters identified in recent studies. In light of the extensive contribution of RUNX
383 transcription factors to developmental processes (Mevel et al., 2019), our study suggests that
384 *Runx1*, but also *Runx2*, may be involved in the development and maintenance of specific
385 subpopulations of the prostate epithelium. Future work should therefore aim at characterizing
386 the functional role played by RUNX factors in the prostate, in particular in PLCs.
387 We demonstrate that these RUNX1$^+$ PLCs exhibit a greater organoid forming potential
388 compared to the remaining luminal fraction, consistent with previous reports isolating similar
389 proximal populations using different markers such as SCA-1, TROP2 or CD26 (Crowley et al.,
390 2020; Goldstein et al., 2008; Guo et al., 2020; Karthaus et al., 2020; Kwon et al., 2016).
391 Furthermore, RUNX1$^+$ PLCs predominantly formed unipotent K8$^+$ hollow organoids
392 demonstrating their preferential commitment to the luminal fate. The greater clonogenicity of
393 RUNX1$^+$ PLCs may in fact be linked to the gene expression profile of the corresponding Lum-D
394 population, suggesting a more immature epithelial state, committed to the luminal lineage but
395 not the secretory function of the prostate. Similar to the enhanced regenerative potential of
396 glandular basal cells under specific regenerative conditions (Centonze et al., 2020), it is

397 tempting to speculate that these cells act as a latent niche of 'facultative' luminal stem cells
398 (Clevers & Watt, 2018), primed to generate a structured prostatic epithelium under defined
399 conditions.

400 Further characterization of RUNX1 expression in prostate development revealed a
401 consistent expression pattern with the adult. RUNX1$^+$ luminal cells were restricted to the most
402 proximal region of the developing prostate buds, both in embryos and UGS explant cultures.
403 Our scRNA-seq of the developing prostate revealed a broad basal identity, supporting the
404 presence of multipotent basal progenitors during embryonic development (Ousset et al., 2012;
405 Pignon et al., 2013), switching to unipotency postnatally (Tika et al., 2019). However, we
406 observed a distinct cluster (C2) that strongly resembled the adult Lum-D population, suggesting
407 an early branching event towards the proximal luminal fate at the onset of prostate
408 development. Subsequent lineage tracing experiments indicated that *Runx1* expressing cells
409 preferentially populate the emerging proximal luminal identity. It would be interesting to
410 determine if the adult Lum-A, Lum-B, and Lum-C derive from multipotent-basal progenitors or
411 from any specific clusters identified in the developing prostate. This appears to be the case at
412 least for the adult Lum-D/RUNX1$^+$ PLCs which already emerges during embryonic specification.

413 Our data also sheds a light on the regenerative potential of specific epithelial
414 populations. Basal and luminal lineages have previously been shown to be largely self-sustained
415 using generic basal and luminal *Cre* drivers (Choi et al., 2012; Ousset et al., 2012). However,
416 whether distinct subpopulations of luminal cells contribute to the regeneration of the others
417 remains poorly understood (X. Wang et al., 2009; Yoo et al., 2016). Our characterization of
418 RUNX1$^+$ PLCs and the detection of a wide variety of luminal populations in our adult prostate

419 scRNA-seq data highlights the possible existence of multiple self-contained luminal populations.
420 Indeed, *Runx1* driven genetic tracing experiments in regression-regeneration assays revealed
421 that RUNX1$^+$ PLCs did not contribute substantially to the regeneration of distal NKX3.1$^+$ cells. It
422 was however evident that RUNX1$^+$ PLCs are intrinsically castration resistant and capable of
423 sustaining their own lineage in the regenerated prostate. Recently, it was proposed that
424 prostate epithelial regeneration is driven by almost all luminal cells persisting in castrated
425 prostates (Karthaus et al., 2020). Our results are compatible with this model, but we further
426 demonstrate that not all luminal subsets retain the same *in vivo* regenerative potential in
427 response to androgen stimulation. Thus, we suggest that the model of self-sustained basal and
428 luminal populations might be extended to individual luminal subpopulations. This hypothesis
429 should be tested in the future using a more specific Lum-D *Cre* driver (e.g. *Krt4*/*Psca*). It will also
430 be of interest to investigate the self-sustenance of other luminal compartments using Lum-A,
431 Lum-B and Lum-C specific *Cre* drivers.
432 Finally, our study suggests that the emerging C2/Lum-D population retains a more
433 embryonic-like program, which may relate to their intrinsic castration-resistant potential and
434 have broader relevance to cancer treatment. Along these lines, recent work by Guo and
435 colleagues indicates that *Pten* loss induced in *Psca* expressing cells of the proximal prostate can
436 initiate prostatic intraepithelial neoplasia (Guo et al., 2020). These results warrant future
437 investigation of this luminal subset in the context of cancer development, tumor aggressiveness
438 and treatment responses.
439

440 In conclusion, we characterized the expression pattern of *Runx1* in the developing,
441 normal and castrated mouse prostate. We observed that *Runx1* marks proximal luminal cells,
442 which is a distinct luminal lineage emerging early during prostate specification, displaying
443 intrinsic castration-resistant and self-sustaining properties. Our results therefore reveal strong
444 intrinsic lineage differences within the luminal compartment of the prostate epithelium.

445 # MATERIALS AND METHODS

446 ## KEY RESOURCES TABLE

Reagent type (species) or resource	Designation	Source or reference	Identifiers	Additional information
Strain, strain background (*Mus musculus,* male)	ICR (CD-1) wild-type	Envigo	Hsd:ICR (CD-1)	7-15 week old males
Strain, strain background (*Mus musculus,* male)	P1-*Runx1*:GFP	Georges Lacaud lab		7-15 week old males
Strain, strain background (*Mus musculus,* male)	P2-*Runx1*:RFP	Georges Lacaud lab		7-15 week old males
Strain, strain background (*Mus musculus,* male)	*Runx1*$^{\text{mER-CRE-mER}}$ *Runx1*^{CreER} *Rosa26*$^{LSL\text{-}RFP}$	RIKEN (Japan) Samokhvalov et al., 2007	Runx1-MER-Cre-MER	C57Bl/6J background 7-15 week old males
Strain, strain background (*Mus musculus,* male)	*Rosa26*$^{\text{flox-stop-flox-tdRFP}}$ *Runx1*^{CreER} *Rosa26*$^{LSL\text{-}RFP}$	European Mouse Mutant Archive Luche et al., 2007	B6.Cg-Thy1 Gt(ROSA)26 Sortm1Hjf	C57Bl/6J background 7-15 week old males
Antibody	Anti-RUNX1 (rabbit monoclonal)	Cell Signaling	Cat: 8529 RRID:AB_10 950225	IHC/IF (1:100)

Antibody	Anti-NKX3.1 (rabbit polyclonal)	Athenaes	Cat: AES-0314	IHC/IF (1:200)
Antibody	Anti-CDH1 (goat polyclonal)	R&D Systems	Cat: AF748 AB_355568	IHC/IF (1:400)
Antibody	Anti-p63 (rabbit monoclonal)	Cell Signaling	Cat: 39692 RRID:AB_2799159	IHC/IF (1:800)
Antibody	Anti-K5 (rabbit monoclonal)	Abcam	Cat: ab52635 RRID:AB_869890	IHC/IF (1:400)
Antibody	Anti-K8 (rabbit monoclonal)	Abcam	Cat: ab53280 RRID:AB_869901	IHC/IF (1:400)
Antibody	Anti-K4 (mouse monoclonal)	Abcam	Cat: Ab9004 RRID:AB_306932	IHC/IF (1:100)
Antibody	Anti-LY6D (rabbit polyclonal)	Proteintech	Cat: 17361-1-AP	IHC/IF (1:100)
Antibody	Anti-TROP-2 (goat polyclonal)	R&D Systems	Cat: AF1122 RRID:AB_2205662	IHC/IF (1:200)
Antibody	Anti-BrdU (rat monoclonal)	Abcam	Cat: ab6326 RRID:AB_305426	IHC/IF (1:400)
Antibody	Anti-Ki67 (rabbit monoclonal)	Abcam	Cat: ab15580 RRID:AB_443209	IHC/IF (1:800)

Antibody	Anti-RFP (rabbit polyclonal)	Rockland	Cat: 600-402-379 RRID:AB_828391	IHC/IF (1:400)
Antibody	Anti-RFP (rabbit monoclonal)	MBL	Cat: PM005 RRID:AB_591279	IF (1:200)
Antibody	Anti-GFP (rabbit polyclonal)	MBL	Cat: 598 RRID:AB_591816	IF (1:200)
Antibody	EnVision+/HRP Anti-Rabbit	Dako (Agilent)	Cat: K4003 RRID:AB_2630375	IHC/IF Ready to use
Antibody	EnVision+/HRP Anti-Rabbit	Dako (Agilent)	Cat: K4001 RRID:AB_2827819	IHC/IF Ready to use
Antibody	ImmPRESS HRP Anti-Goat	Vector Laboratories	Cat: MP-7405 RRID:AB_2336526	IHC/IF Ready to use
Antibody	ImmPRESS HRP Anti-Rat	Vector Laboratories	Cat: MP-7444 RRID:AB_2336530	IHC/IF Ready to use
Antibody	Donkey anti-Goat IgG 647	ThermoFisher Scientific	Cat: A-21447 RRID:AB_141844	IF (1:400)
Antibody	Anti-CD16/32 Fc block	Biolegend	Cat: 101301 Clone: 93 RRID:AB_312800	FACS (1:200)
Antibody	Anti-CD45 SB436	ThermoFisher Scientific	Cat: 62-0451-82 Clone: 30-F11	FACS (1:200)

			RRID:AB_2744774	
Antibody	Anti-EPCAM BV421	Biolegend	Cat: 118225 Clone: G8.8 RRID:AB_2563983	FACS (1:200)
Antibody	Anti-EPCAM APC	Biolegend	Cat: 118214 Clone: G8.8 RRID:AB_1134102	FACS (1:200)
Antibody	Anti-CD49f FITC	Biolegend	Cat: 313606 Clone: GoH3 RRID:AB_345300	FACS (1:200)
Antibody	Anti-CD49f APC	Biolegend	Cat: 313616 Clone: GoH3 RRID:AB_1575047	FACS (1:200)
Antibody	Anti-CD24 BV786	BD Biosciences	Cat: 744470 Clone: M1/69 RRID:AB_2742258	FACS (1:200)
Sequence-based reagent	MULTI-seq reagents	Zev Gartner lab McGinnis, Patterson, et al., 2019		
Software, algorithm	R v3.6.3	CRAN R Project	SCR_001905	https://cran.r-project.org
Software, algorithm	deMULTIplex	McGinnis, Patterson, et al., 2019		https://github.com/chris-mcginnis-ucsf/MULTI-seq

Software, algorithm	DoubletFinder	McGinnis, Murrow, et al., 2019	SCR_018771	https://github.com/chris-mcginnis-ucsf/DoubletFinder
Software, algorithm	Seurat v3.1.5	Rahul Satija lab	SCR_016341	https://github.com/satijalab/seurat
Software, algorithm	Scanpy v1.4.6 PAGA	Wolf et al., 2019	SCR_018139	https://scanpy.readthedocs.io/en/stable/
Software, algorithm	AUCell v1.8.0	Aibar et al., 2017		https://github.com/aertslab/AUCell
Software, algorithm	scater v1.14.6	Bioconductor	SCR_015954	https://bioconductor.org/packages/release/bioc/html/scater.html
Software, algorithm	QuPath v0.2	Bankhead et al., 2017	SCR_018257	https://qupath.github.io/
Software, algorithm	Cellranger v3.1.0	10x Genomics	SCR_017344	
Software, algorithm	FlowJo v10	BD Life Sciences	SCR_008520	
Software, algorithm	Harmony	PerkinElmer	SCR_018809	
Software, algorithm	Graphpad Prism v8.4.2	Graphpad	SCR_002798	

447

448 **Animal work**

449 Animal experiments were approved by the Animal Welfare and Ethics Review Body
450 (AWERB) of the Cancer Research UK Manchester Institute and conducted according to the UK
451 Home Office Project Licence (PPL 70/8580). Genetic lineage-tracing experiments were
452 performed at the Beatson Biological Services Unit (PPL 70/8645 & P5EE22AEE) and approved by
453 the University of Glasgow AWERB. Mice were maintained in purpose-built facility in a 12-hour
454 light/dark cycle with continual access to food and water.

455

456 Immunocompetent wild-type ICR (CD-1) mice were purchased from Envigo. P1-*Runx1*:GFP
457 and P2-*Runx1*:RFP have been described previously (Draper et al., 2018; Sroczynska et al., 2009).
458 Colonies were maintained on a ICR (CD-1) background. C57Bl/6J *Runx1*$^{\text{mER-CRE-mER}}$ (Samokhvalov
459 et al., 2007) were provided by RIKEN (Japan). C57Bl/6J *Rosa26*$^{\text{flox-stop-flox-tdRFP}}$ mice (Luche et al.,
460 2007) were acquired from the European Mouse Mutant Archive (EMMA). For all transgenic
461 lines, routine genotyping was undertaken at weaning (3 weeks of age) by automated PCR
462 genotyping (Transnetyx). For timed mating experiments, vaginal plug detection was considered
463 as embryonic day (E) 0.5.

464

465 All animal procedures were performed on adult males at least 7 weeks of age. Surgical
466 castration was carried out under aseptic conditions. For prostate regeneration assays,
467 testosterone pellets (Belma Technologies) were implanted subcutaneously. For *in vivo* genetic
468 lineage-tracing experiments, tamoxifen (Sigma, T5648) was resuspended in ethanol and diluted

469 in corn oil at a concentration of 10 mg/mL and administered via intra-peritoneal injections daily
470 for 4 consecutive days using the following regimen: 3mg, 2mg, 2mg, 2mg.
471
472 **Isolation of mouse prostate cells**
473 All dissections were performed under a stereo microscope in sterile PBS. Dissociated murine
474 prostate cells were obtained by digesting pre-minced prostate tissue for 1h at 37˚C in digestive
475 medium prepared in prepared in ADMEM/F12 (Gibco), and containing 1mg/mL Collagenase
476 Type I (ThermoFischer Scientific, #17018029), 1mg/mL Dispase II (ThermoFischer Scientific,
477 #17105041), 10% Fetal Bovine Serum (Gibco), 1% Penicillin-Streptomycin-Glutamine (Sigma),
478 and 10 µM Y-27632 dyhydrochloride (Chemdea, #CD0141). For embryonic urogenital sinuses
479 (UGS), dissociation time was reduced to 30 min. Single cells were obtained after an additional
480 10 min incubation in TrypLE (Gibco) at 37˚C before mechanical dissociation with a syringe and
481 needle (25G). Cells were then filtered through a 50 µm cell strainer.
482
483 **Flow-cytometry and cell-sorting**
484 Single cell suspensions were kept in Advanced DMEM/F-12 (Gibco) containing 5% FBS
485 supplemented with 10 µM Y-27632. Cells were incubated for 10 min using unconjugated anti-
486 mouse CD16/32 antibody (Biolegend, C93, #101301) at 4˚C prior to labelling with specific
487 fluorochrome-labelled antibodies. Details of FACS reagents and antibodies are listed in the Key
488 Resources Table. Cells were filtered through a 50 µm cell strainer prior to acquisition. Hoechst
489 33258 or Sytox blue (ThermoFischer Scientific) were used as viability stains. Single-cell

490 suspensions were analyzed on a Fortessa (BD Biosciences) and sorts were performed on a
491 FACSAriaIII (BD Biosciences). FACS data were analyzed using FlowJo software (BD Life Sciences).
492
493 **Organoid formation assays**
494 *In vitro* organoid formation assays were performed as described in Drost et al., 2016. Single
495 cells were resuspended in 40 µL drops of phenol red-free Cultrex RGF BME Type 2 (BME 2,
496 Amsbio, #3533-005-02), and seeded in CellCarrier-96 Ultra Microplates (PerkinElmer,
497 #6055302). Defined organoid culture medium was prepared with Advanced DMEM/F-12
498 (Gibco), supplemented with 10 mM Hepes (Sigma), Gutamax (Gibco), Penicillin/Streptomycin
499 (Sigma), B27 (Life Technologies, 17504-044), 50 mg/mL EGF (PeproTech, #AF-100-15), 500
500 ng/mL R-spondin 1 (R&D Systems, #4645-RS), 100 ng/mL Noggin (R&D Systems, #6057-NG), 10
501 mM Y-27632 dyhydrochloride (Chemdea, #CD0141), 200nM A83-01 (Tocris Bioscience, #2939),
502 1.25 mM N-Acetylcystein (Sigma), and 1 nM Dihydrotestosterone (DHT, Sigma #730637).
503 Medium was refreshed every 2-3 days, and organoid cultures were scored after 7 days.
504
505 **UGS explant cultures**
506 UGS explant cultures were performed as described previously (Kruithof-de Julio et al.,
507 2013). Briefly, E15.5 embryos were obtained from timed matings. Urogenital sinuses (UGS)
508 were isolated from the embryos and cultured using a Durapore Membrane Filter 0.65 µm
509 (#DVPP02500) placed on a stainless-steel mesh for up to 7 days in Ham's F-12/DMEM (Gibco)
510 supplemented with Insulin-Transferrin-Sodium Selenite Supplement (Roche) and 10 µM
511 dihydrotestosterone (Sigma). Media were renewed every 2-3 days. For lineage-tracing

512 experiments, tamoxifen-induced labelling was performed using 0.5 µM 4-hydroxytamoxifen
513 (#T176, Sigma).
514
515 **Immunohistochemistry**
516 Prostate tissues were harvested and fixed in 10% buffered formalin for 24h. Fixed tissues
517 were processed using standard procedures and embedded in paraffin. Formalin-fixed paraffin-
518 embedded (FFPE) sections (4 µm) were cut and dried overnight at 37°C. Multiplexed
519 immunofluorescent stainings of FFPE sections were performed on an automated Leica BOND RX
520 platform using the Opal multiplexing workflow (PerkinElmer). In brief, sections were dewaxed,
521 and rehydrated, and endogenous peroxidase activity was quenched by 10 min pre-treatment
522 with 3% hydrogen peroxide diluted in TBS-T (Tris-Buffered Saline 0.05% Tween-20). Following
523 on-board heat-induced epitope retrieval with citrate buffer (pH 6.0) for 20 min, sections were
524 incubated for 10 min with 10% Casein (Vector Laboratories) diluted in TBS-T. Each staining cycle
525 included a primary antibody incubation for 30 min, followed by buffer washes, and 30 min
526 incubation with HRP labelled secondary antibodies (Key Resources Table). After further washes,
527 the Tyramide labeled with a fluorophore (Opal 520, Opal 570 or Opal 650, PerkinElmer) was
528 added for a final 10 min. Subsequent antibody stainings were performed by repeating the same
529 procedure, separated by heat-mediated antibody denaturation using citrate buffer (pH 6.0) for
530 5 min at 95°C. Nuclei were counterstained with DAPI (Sigma) and slides were sealed using
531 ProLong Gold Antifade Mountant (ThermoFischer Scientific). *In situ* hybridization (ISH) to detect
532 *Nupr1* (ACD, LS 2.5 Mm-Nupr1 #434818) was done using the Multiplex Fluorescent detection kit
533 (ACD) on the automated Leica BOND RX platform following the manufacturer's instructions.

534 Pre-treatment was done using an EDTA based pH 9.0 epitope retrieval solution for 15 min at
535 88°C followed by 10 min protease incubation. After ISH, antibody staining was carried out using
536 an anti-RFP antibody for 1h detected with EnVision HRP anti-rabbit secondary (Agilent)
537 followed by incubation with Tyramide-conjugated Opal 570 (PerkinElmer) as described above.
538 Anti-CDH1 antibody was applied for 1h and detected using an anti-goat Alexa Fluor 647
539 secondary antibody (ThermoFischer Scientific, #A-21447). Staining of frozen sections was
540 performed as described previously (Thambyrajah et al., 2016). The list of antibodies used is
541 available in the Key Resources Table.
542
543 **Image acquisition and analysis**
544 Whole-slide images were acquired on an Olympus VS120 slide scanner. Images were
545 analyzed using QuPath v0.2 (Bankhead et al., 2017). Briefly, annotations were drawn manually
546 to select areas of interest. Nuclear detection was achieved using the "cell detection" module on
547 the DAPI channel. A classifier was then trained for each batch of images using the random
548 forest algorithm, to detect the epithelial layers based on either CDH1 or K5/K8 stainings. Single-
549 cell intensity measurements were analyzed using R (3.6.3). For Quantitative Imaged-Based
550 Cytometry (QBIC), single-cell intensity measurements were $\log_{10}$ transformed and plotted using
551 the 'geom_hex' function of the ggplot2 R package. QuPath was used to extract representative
552 high-quality raw images of selected areas from whole slide images using the 'Send region to
553 ImageJ' tool. Images used for publication were processed with ImageJ (NIH Image, Maryland,
554 USA). Confocal images were acquired using a Leica TCS SP8 confocal microscope and LAS X Leica
555 software. Images of whole UGS explant culture were taken using a Leica MZ FLIII microscope.

556

557 **Whole-mount immunofluorescent staining of organoids**

558 Whole-mount staining was adapted from Yokomizo et al., 2012. Organoids were fixed
559 directly in 96-well plates using 4% paraformaldehyde for 1h at 4°C. After 3 washes of 5 min in
560 PBS, organoids were incubated in PBS-BST, containing PBS, 1% milk, 1% BSA, 10% goat serum
561 (Agilent, #X090710), 0.4% Triton X-100. Pre-conjugated primary antibodies, K5 Alexa Fluor 647
562 (#ab193895, Abcam) and K8 Alexa Fluor 488 (#ab192467, Abcam) were diluted at 1/400 in PBS-
563 BST and incubated with the organoids overnight at 4°C on a rocking platform. After 3 washes of
564 1h in PBS-BST at 4°C, organoids were stained with DAPI at 2 µg/mL diluted in PBS-BST and
565 incubated for another 30 min at 4°C on a rocking platform. Images were acquired on an Opera
566 Phenix High Content Screening System using the 10x air and 20x water lenses. Quantitative
567 analysis was performed using the Harmony software on maximum projection images.

568

569 **scRNA-seq sample preparation**

570 A detailed description of the samples, replicates, and the corresponding cellular populations
571 used for each sequencing run is provided in Supplementary file 1. For the adult mouse prostate
572 dataset, AP, DLP, and VP lobes were micro dissected and pooled from P2-*Runx1*:RFP reporter
573 mice after dissociation. Single live EPCAM^{+} cells from RFP^{+} and RFP^{-} fractions of each lobes were
574 sorted separately (containing a mix of CD49f^{high} basal and CD24^{high} luminal cells). For the UGS
575 explant culture dataset, the middle regions of the explants were micro dissected to enrich for
576 prostatic branching events and pooled by time point after dissociation. Single live EPCAM+ cells
577 were sorted for each independent time point.

578

579 **scRNA-seq sample multiplexing**

580 Individually sorted populations were multiplexed using the MULTI-seq protocol (McGinnis,
581 Patterson, et al., 2019). Reagents were kindly provided by Dr. Zev Gartner. In brief, after
582 sorting, cells were washed once in cold serum- and BSA-free PBS. A lipid-modified DNA
583 oligonucleotide and a specific sample barcode oligonucleotide were then mixed and added to
584 the cells at a final concentration of 200 nM each, and incubated in cold PBS for 5 min. Each
585 individual sample to be multiplexed received an independent sample barcode. Next, a common
586 lipid-modified co-anchor was added at 200 nM to each sample to stabilize the membrane
587 bound barcodes. After an additional 5 min incubation on ice, cells were washed 2 times with
588 PBS containing 1% FBS 1% BSA in order to quench unbound barcodes. Samples were then
589 pooled together and washed once with PBS 1% FBS 1% BSA. After cell counting, cells were
590 loaded in a Chromium Single Cell 3' GEM Library & Gel Bead Kit v3 (10x Genomics).

591

592 **scRNA-seq library preparation, sequencing and pre-processing**

593 Gene expression (cDNA) libraries were prepared according to the manufacturer's protocol.
594 MULTI-seq barcode libraries were separated from the cDNA libraries during the first round of
595 size selection, and PCR amplified prior to sequencing according to the MULTI-seq library
596 preparation protocol (McGinnis, Patterson, et al., 2019). For the adult mouse prostate dataset,
597 cDNA libraries of 'run 1' and 'run 2' were sequenced on Illumina NovaSeq 6000 System, and
598 'run 3' was sequenced on Illumina HiSeq 2500. The UGS mouse prostate explant run was also
599 sequenced on Illumina HiSeq 2500. Sequencing data of cDNA libraries were processed using

600 Cellranger v3.1.0 and mapped onto mm10 mouse reference genome. Pre-processing of the
601 MULTI-seq library fastq files was performed using the 'deMULTIplex' (v1.0.2) R package
602 (https://github.com/chris-mcginnis-ucsf/MULTI-seq) to generate a sample barcode UMI count
603 matrix. Detailed quality control metrics of each sequencing run are provided in Supplementary
604 file 1.
605
606 **Adult mouse prostate dataset analysis**
607 *Quality control and barcode demultiplexing of individual runs.* Each run was pre-processed
608 individually prior data integration. Cellranger outputs were loaded into the R package Seurat
609 (v3.1.5). Cells were kept if they had more than 750 detected genes, less than 7500 UMIs and
610 less than 10% mitochondrial transcripts. Sample barcodes were demultiplexed using the
611 HTODemux function implemented in Seurat. Briefly, a negative binomial distribution was used
612 to estimate the background levels based on *k*-means clustering of the barcode normalized
613 counts. Barcodes with values above the 99% quantile were considered 'positive' for a given
614 sample. Cells positive for more than one barcode were considered as 'doublets'. Doublets and
615 negative cells were excluded for all downstream analyses. Thresholds were empirically adjusted
616 to remove additional cells with possible ambiguous classification (Supplementary file 1). Of
617 note, in both 'run 1' and 'run 2', a large number of cells were classified 'negative' due to the
618 failed labelling of 'Bar3' (corresponding to 'Intact DLP RFP+' sample). For these runs, we used
619 DoubletFinder (McGinnis, Murrow, et al., 2019) to remove predicted doublets missed out as a
620 consequence of the failed labeling of 'Bar3'. After classification, barcodes were represented in

621 UMAP space to confirm the purity of the barcode assignment obtained for each sample (Figure
622 3–figure supplement 5A). We obtained a total of 4,499 cells from 3 independent experiments.
623
624 *Integration, low dimensional embedding and clustering.* Data aggregation was performed
625 according to the standard integration procedure implemented in Seurat. In brief, each dataset
626 was log normalized, and 3000 variable features were initially computed using the 'vst' method.
627 For integration, 2000 features and 50 dimensions were used as anchors. Integrated data were
628 scaled and the first 50 principal components (PC) were calculated for downstream analyses.
629 Uniform Manifold Approximation and Projection (UMAP) (McInnes et al., 2018) was used for
630 visualization. Graph-based louvain clustering was performed on a shared nearest neighbor
631 graph constructed using 20 nearest neighbors for every cell, and a resolution of 0.4, which gave
632 a reasonable segmentation of the data (Figure 3–figure supplement 5B,C). Extensive
633 exploration of each cluster based on known marker genes was then carried out to subset
634 prostate epithelial cells. We found 10 prostate epithelial clusters (*Epcam*, *Krt8*, *Cd24a*, *Spink1*,
635 *Krt19*, *Tacstd2*, *Psca*, *Krt4*, *Tgm4*, *Nkx3-1*, *Pbsn*, *Msmb*, *Piezo2*, *Trp63*, *Krt5*, *Krt14*), 3 clusters of
636 hematopoietic cells (*Vim*, *Ptprc*, *Cd74*, *Itgam*, *Cd3d*), 1 cluster of endothelial cells (*Pecam1*), 1
637 cluster of fibroblasts (*Vim*, *Col1a1*) and 1 cluster of mesonephric derivatives (*Svs2*, *Pax2*) (Figure
638 3–figure supplement 5D,E).
639
640 *Analysis of prostate epithelial populations.* The same dimension reduction approach described
641 above was performed on the selected prostate epithelial clusters, using a resolution of 0.3 for
642 graph-based louvain clustering. We annotated 1 large population of basal cells by merging 3

643 subclusters highly expressing *Krt5*, *Krt14* and *Trp63* as we did not discuss the heterogeneity of
644 the basal compartment in this study (Figures 3B-D; Figure 3–figure supplement 6F,I). We
645 annotated the different luminal clusters expressing higher levels of *Cd26*/*Dpp4, Cd24a*, *Krt8* and
646 *Krt18*, as Lum-A, Lum-B, Lum-C, Lum-D, Lum-E and Lum-F. Several genes specifically marked
647 each cluster, including *Sbp*/*Spink1* in Lum-A, *Tgm4* in Lum-B, *Msmb* in Lum-C, *Psca*/*Krt4* in Lum-
648 D, *Basp1*/*Lpl* in Lum-E, and *Crym* in Lum-F (Figures 3C, D; Figure 3–figure supplement 7A). Data
649 were then imported in Scanpy (v1.4.6) to infer lineage relationships between cellular
650 populations via partition-based graph abstraction (PAGA) implemented in the tl.paga function
651 (Wolf et al., 2019). Briefly, a single cell neighborhood graph (n_neighbors = 50) was computed
652 using the integrated principal components previously calculated in Seurat. PAGA was generated
653 based on our annotated clusters. The final UMAP representation was generated using PAGA-
654 initialised positions to better preserve the global topology of the data. All final data
655 visualizations were generated in R.
656
657 *Differential gene expression analysis and gene ontology.* Differential gene expression analyses
658 between clusters were performed using the MAST method (Finak et al., 2015) implemented in
659 Seurat within the 'FindAllMarkers' and 'FindMarkers' functions. Testing was limited to genes
660 detected in at least 25% of the tested populations (min.pct = 0.25) and showing at least ± 0.25
661 log fold change difference (logfc.threshold = 0.25). The 'g:GOSt' function of the gprofiler2 R
662 package was used to perform functional enrichment analysis on gene ontology terms (GO:BP,
663 biological processes). Genes showing at least 0.50 log fold change enrichment in the group
664 tested were kept.

665

666 **UGS explant cultures dataset**

667 A similar strategy was applied for the analysis of the UGS explant culture dataset, with some

668 alterations described below.

669

670 *Quality control and barcode demultiplexing.* Cells were kept if they had more than 1000

671 detected genes, and less than 7.5% mitochondrial transcripts. Barcode classification was

672 performed as above, using the 90% quantile in 'HTODemux' (Figure 6–figure supplement 12A).

673 We obtained a total of 5,122 cells that passed quality control from the 4 time points.

674

675 *Low dimensional embedding and clustering.* The first 50 principal components and 20 neighbors

676 were used for UMAP visualization. Graph-based clustering was done using a resolution

677 parameter of 0.3. We noticed a strong effect of cell cycle using cell cycles genes defined in

678 Tirosh et al., 2016. This was particularly evident using the 'CellCycleScoring' function

679 implemented in Seurat (Figure 6–figure supplement 12B). To minimize the impact of cell cycle

680 on downstream analyses, the cell cycle scores were regressed out during data scaling. We

681 identified 6 main clusters, that we annotated based on the expression of several marker genes

682 (Figure 6–figure supplement 12C-E). We identified 2 clusters of developing mesonephric

683 derivatives (*Hoxb7*, *Wfdc2*, *Gata3*, *Sox17*, *Pax2*, *Pax8*, *Lhx1*), 1 cluster of developing bladder

684 urothelium (*Upk3a*, *Foxq1*, *Plaur*, *Krt7*, *Krt20*), 1 cluster of mesenchymal cells (*Vim*, *Col3a1*,

685 *Col1a1*, *Pdgfra*, *Zeb1*) and 1 cluster corresponding to the developing prostatic epithelium

686 (*Epcam*, *Krt8*, *Krt5*, *Krt14*, *Krt15*, *Shh*, *Hoxb13*, *Hoxd13*, *Nkx3-1*). We also identified one cluster
687 largely associated with hypoxia and cellular stress ontologies (Figure 6–figure supplement 12F).
688
689 *Analysis of the developing prostatic epithelium.* The same dimension reduction approach was
690 initially applied on the developing prostatic cluster. After graph-based clustering using a
691 resolution of 0.5, 10 clusters were identified and visualized via UMAP (Figure 6–figure
692 supplement 12G-J). We computed diffusion components using 'runDiffusionMap'
693 (ncomponents = 20, k = 20) implemented in the scater (v1.14.6) R package. We found the small
694 cluster C9 to be largely diverging from the remainder fraction in diffusion space, therefore it
695 was excluded for downstream analysis (Figure 6–figure supplement 12K). We then imported
696 the data in Scanpy and used the first 10 diffusion components to compute a neighborhood
697 graph (n_neighbors = 20) which was used for PAGA. We finally computed a force-direct layout
698 (ForceAtlas2) using PAGA-initialised positions.
699
700 *Analysis of gene set activity.* Gene signatures were generated from the list of differentially
701 expressed genes by keeping those showing at least 0.50 log fold change enrichment in each
702 given group. Gene lists were used as custom gene sets (Supplementary file 5) in the AUCell
703 (Aibar et al., 2017) R package (v1.8.0). Briefly, AUCell uses the Area Under the Curve to evaluate
704 the enrichment of a given gene set in each cell, in a ranking based manner. It outputs an AUC
705 score for each individual cell, which is used to explore the relative expression of the signature.
706 Per cell AUC scores of each signatures were overlayed on the dimension reduction layout and
707 plotted as boxplots to visualize enrichments across the different cellular subsets.

708

709 **Data availability**

710 Raw sequencing files and processed gene expression matrices have been deposited in the
711 NCBI Gene Expression Omnibus under the accession number GSE151944. The processed
712 datasets for both mouse adult prostate and UGS prostate explant cultures can be accessed via a
713 searchable R Shiny application available at http://shiny.cruk.manchester.ac.uk/pscapp/. All
714 code used to process data and generate figures is available on a public GitHub repository at
715 https://github.com/glacaud/prostate-scRNAseq.

716

717 **Statistical analyses**

718 Statistical analyses were performed using Graphpad/Prism (v8.4.2). Data are
719 represented as mean ±SD. Unless otherwise specified in the corresponding figure legend, two-
720 tailed unpaired *t*-tests were used to compare means between two groups. Statistical
721 significance was set at $p < 0.05$. For animal model studies, no statistical method was used to
722 pre-determine the sample size. No randomization or blinding was used for *in vivo* studies.

723

ACKNOWLEDGEMENTS

We thank the laboratories' members for critical reading of the manuscript, in particular Dr. Michael Lie-a-ling, Dr. Alice Lallo and Catherine Winchester. We thank the staff at the Histology, Flow Cytometry, Advanced Imaging, Molecular Biology, and Breeding Unit Core facilities of CRUK Manchester Institute, as well as the CRUK Beatson Biological Services Unit and Flow Cytometry Core facility for technical support. We thank Dr. Zev Gartner for kindly providing the MULTI-seq reagents. We thank Dr. Kirsteen Campbell with assistance on the lineage tracing experiments. We thank Dr. Berenika Plusa and Dr. Roberto de la Fuente with assistance on timed matings experiments. We thank Professor Hans Jorg Fehling and the European Mouse Mutant Archive for providing the Rosa26$^{\text{flox-stop-flox-tdRFP}}$ mice.

COMPETING INTERESTS

The authors declare no competing interests.

REFERENCES

Aibar, S., González-Blas, C. B., Moerman, T., Huynh-Thu, V. A., Imrichova, H., Hulselmans, G., Rambow, F., Marine, J.-C., Geurts, P., Aerts, J., van den Oord, J., Atak, Z. K., Wouters, J., & Aerts, S. (2017). SCENIC: Single-cell regulatory network inference and clustering. *Nature Methods*, *14*(11), 1083–1086. https://doi.org/10.1038/nmeth.4463

Banach-Petrosky, W., Jessen, W. J., Ouyang, X., Gao, H., Rao, J., Quinn, J., Aronow, B. J., & Abate-Shen, C. (2007). Prolonged exposure to reduced levels of androgen accelerates prostate cancer progression in Nkx3.1; Pten mutant mice. *Cancer Research*, *67*(19), 9089–9096. https://doi.org/10.1158/0008-5472.CAN-07-2887

Bankhead, P., Loughrey, M. B., Fernández, J. A., Dombrowski, Y., McArt, D. G., Dunne, P. D., McQuaid, S., Gray, R. T., Murray, L. J., Coleman, H. G., James, J. A., Salto-Tellez, M., & Hamilton, P. W. (2017). QuPath: Open source software for digital pathology image analysis. *Scientific Reports*, *7*(1), 16878. https://doi.org/10.1038/s41598-017-17204-5

Barros-Silva, J. D., Linn, D. E., Steiner, I., Guo, G., Ali, A., Pakula, H., Ashton, G., Peset, I., Brown, M., Clarke, N. W., Bronson, R. T., Yuan, G.-C., Orkin, S. H., Li, Z., & Baena, E. (2018). Single-Cell Analysis Identifies LY6D as a Marker Linking Castration-Resistant Prostate Luminal Cells to Prostate Progenitors and Cancer. *Cell Reports*, *25*(12), 3504-3518.e6. https://doi.org/10.1016/j.celrep.2018.11.069

Berman, D. M., Desai, N., Wang, X., Karhadkar, S. S., Reynon, M., Abate-Shen, C., Beachy, P. A., & Shen, M. M. (2004). Roles for Hedgehog signaling in androgen production and prostate ductal morphogenesis. *Developmental Biology*, *267*(2), 387–398. https://doi.org/10.1016/j.ydbio.2003.11.018

760 Bhatia-Gaur, R., Donjacour, A. A., Sciavolino, P. J., Kim, M., Desai, N., Young, P., Norton, C. R.,
761 Gridley, T., Cardiff, R. D., Cunha, G. R., Abate-Shen, C., & Shen, M. M. (1999). Roles for
762 Nkx3.1 in prostate development and cancer. *Genes & Development*, *13*(8), 966–977.
763 Browne, G., Taipaleenmäki, H., Bishop, N. M., Madasu, S. C., Shaw, L. M., van Wijnen, A. J.,
764 Stein, J. L., Stein, G. S., & Lian, J. B. (2015). Runx1 is associated with breast cancer
765 progression in MMTV-PyMT transgenic mice and its depletion in vitro inhibits migration
766 and invasion. *Journal of Cellular Physiology*, *230*(10), 2522–2532.
767 https://doi.org/10.1002/jcp.24989
768 Burger, P. E., Xiong, X., Coetzee, S., Salm, S. N., Moscatelli, D., Goto, K., & Wilson, E. L. (2005).
769 Sca-1 expression identifies stem cells in the proximal region of prostatic ducts with high
770 capacity to reconstitute prostatic tissue. *Proceedings of the National Academy of*
771 *Sciences of the United States of America*, *102*(20), 7180–7185.
772 https://doi.org/10.1073/pnas.0502761102
773 Centonze, A., Lin, S., Tika, E., Sifrim, A., Fioramonti, M., Malfait, M., Song, Y., Wuidart, A., Van
774 Herck, J., Dannau, A., Bouvencourt, G., Dubois, C., Dedoncker, N., Sahay, A., de
775 Maertelaer, V., Siebel, C. W., Van Keymeulen, A., Voet, T., & Blanpain, C. (2020).
776 Heterotypic cell–cell communication regulates glandular stem cell multipotency. *Nature*,
777 *584*(7822), 608–613. https://doi.org/10.1038/s41586-020-2632-y
778 Chimge, N.-O., Little, G. H., Baniwal, S. K., Adisetiyo, H., Xie, Y., Zhang, T., O'Laughlin, A., Liu, Z.
779 Y., Ulrich, P., Martin, A., Mhawech-Fauceglia, P., Ellis, M. J., Tripathy, D., Groshen, S.,
780 Liang, C., Li, Z., Schones, D. E., & Frenkel, B. (2016). RUNX1 prevents oestrogen-

781 mediated AXIN1 suppression and β-catenin activation in ER-positive breast cancer.
782 *Nature Communications*, *7*, 10751. https://doi.org/10.1038/ncomms10751
783 Choi, N., Zhang, B., Zhang, L., Ittmann, M., & Xin, L. (2012). Adult murine prostate basal and
784 luminal cells are self-sustained lineages that can both serve as targets for prostate
785 cancer initiation. *Cancer Cell*, *21*(2), 253–265. https://doi.org/10.1016/j.ccr.2012.01.005
786 Chua, C. W., Shibata, M., Lei, M., Toivanen, R., Barlow, L. J., Bergren, S. K., Badani, K. K.,
787 McKiernan, J. M., Benson, M. C., Hibshoosh, H., & Shen, M. M. (2014). Single luminal
788 epithelial progenitors can generate prostate organoids in culture. *Nature Cell Biology*,
789 *16*(10), 951–961, 1–4. https://doi.org/10.1038/ncb3047
790 Clevers, H., & Watt, F. M. (2018). Defining Adult Stem Cells by Function, not by Phenotype.
791 *Annual Review of Biochemistry*, *87*(1), 1015–1027. https://doi.org/10.1146/annurev-
792 biochem-062917-012341
793 Crowell, P. D., Fox, J. J., Hashimoto, T., Diaz, J. A., Navarro, H. I., Henry, G. H., Feldmar, B. A.,
794 Lowe, M. G., Garcia, A. J., Wu, Y. E., Sajed, D. P., Strand, D. W., & Goldstein, A. S. (2019).
795 Expansion of Luminal Progenitor Cells in the Aging Mouse and Human Prostate. *Cell*
796 *Reports*, *28*(6), 1499-1510.e6. https://doi.org/10.1016/j.celrep.2019.07.007
797 Crowley, L., Cambuli, F., Aparicio, L., Shibata, M., Robinson, B. D., Xuan, S., Li, W., Hibshoosh, H.,
798 Loda, M., Rabadan, R., & Shen, M. M. (2020). A single-cell atlas of the mouse and human
799 prostate reveals heterogeneity and conservation of epithelial progenitors. *ELife*, *9*.
800 https://doi.org/10.7554/eLife.59465

801 Doles, J. D., Vezina, C. M., Lipinski, R. J., Peterson, R. E., & Bushman, W. (2005). Growth,
802 morphogenesis, and differentiation during mouse prostate development in situ, in renal
803 grafts, and in vitro. *The Prostate*, *65*(4), 390–399. https://doi.org/10.1002/pros.20321
804 Draper, J. E., Sroczynska, P., Fadlullah, M. Z. H., Patel, R., Newton, G., Breitwieser, W., Kouskoff,
805 V., & Lacaud, G. (2018). A novel prospective isolation of murine fetal liver progenitors to
806 study in utero hematopoietic defects. *PLoS Genetics*, *14*(1), e1007127.
807 https://doi.org/10.1371/journal.pgen.1007127
808 Drost, J., Karthaus, W. R., Gao, D., Driehuis, E., Sawyers, C. L., Chen, Y., & Clevers, H. (2016).
809 Organoid culture systems for prostate epithelial and cancer tissue. *Nature Protocols*,
810 *11*(2), 347–358. https://doi.org/10.1038/nprot.2016.006
811 English, H. F., Santen, R. J., & Isaacs, J. T. (1987). Response of glandular versus basal rat ventral
812 prostatic epithelial cells to androgen withdrawal and replacement. *The Prostate*, *11*(3),
813 229–242.
814 Ferrari, N., Mohammed, Z. M. A., Nixon, C., Mason, S. M., Mallon, E., McMillan, D. C., Morris, J.
815 S., Cameron, E. R., Edwards, J., & Blyth, K. (2014). Expression of RUNX1 Correlates with
816 Poor Patient Prognosis in Triple Negative Breast Cancer. *PLoS ONE*, *9*(6), e100759.
817 https://doi.org/10.1371/journal.pone.0100759
818 Finak, G., McDavid, A., Yajima, M., Deng, J., Gersuk, V., Shalek, A. K., Slichter, C. K., Miller, H. W.,
819 McElrath, M. J., Prlic, M., Linsley, P. S., & Gottardo, R. (2015). MAST: A flexible statistical
820 framework for assessing transcriptional changes and characterizing heterogeneity in
821 single-cell RNA sequencing data. *Genome Biology*, *16*(1), 278.
822 https://doi.org/10.1186/s13059-015-0844-5

823 Georgas, K. M., Armstrong, J., Keast, J. R., Larkins, C. E., McHugh, K. M., Southard-Smith, E. M.,
824 Cohn, M. J., Batourina, E., Dan, H., Schneider, K., Buehler, D. P., Wiese, C. B., Brennan, J.,
825 Davies, J. A., Harding, S. D., Baldock, R. A., Little, M. H., Vezina, C. M., & Mendelsohn, C.
826 (2015). An illustrated anatomical ontology of the developing mouse lower urogenital
827 tract. *Development (Cambridge, England)*, *142*(10), 1893–1908.
828 https://doi.org/10.1242/dev.117903
829 Goldstein, A. S., Lawson, D. A., Cheng, D., Sun, W., Garraway, I. P., & Witte, O. N. (2008). Trop2
830 identifies a subpopulation of murine and human prostate basal cells with stem cell
831 characteristics. *Proceedings of the National Academy of Sciences of the United States of*
832 *America*, *105*(52), 20882–20887. https://doi.org/10.1073/pnas.0811411106
833 Goto, K., Salm, S. N., Coetzee, S., Xiong, X., Burger, P. E., Shapiro, E., Lepor, H., Moscatelli, D., &
834 Wilson, E. L. (2006). Proximal Prostatic Stem Cells Are Programmed to Regenerate a
835 Proximal-Distal Ductal Axis. *STEM CELLS*, *24*(8), 1859–1868.
836 https://doi.org/10.1634/stemcells.2005-0585
837 Guo, W., Li, L., He, J., Liu, Z., Han, M., Li, F., Xia, X., Zhang, X., Zhu, Y., Wei, Y., Li, Y., Aji, R., Dai,
838 H., Wei, H., Li, C., Chen, Y., Chen, L., & Gao, D. (2020). Single-cell transcriptomics
839 identifies a distinct luminal progenitor cell type in distal prostate invagination tips.
840 *Nature Genetics*, *52*(9), 908–918. https://doi.org/10.1038/s41588-020-0642-1
841 Höfner, T., Eisen, C., Klein, C., Rigo-Watermeier, T., Goeppinger, S. M., Jauch, A., Schoell, B.,
842 Vogel, V., Noll, E., Weichert, W., Baccelli, I., Schillert, A., Wagner, S., Pahernik, S., Sprick,
843 M. R., & Trumpp, A. (2015). Defined Conditions for the Isolation and Expansion of Basal

844 Prostate Progenitor Cells of Mouse and Human Origin. *Stem Cell Reports*, *4*(3), 503–518.
845 https://doi.org/10.1016/j.stemcr.2015.01.015
846 Horton, C., Liu, Y., Yu, C., Xie, Q., & Wang, Z. A. (2019). Luminal-contact-inhibition of epithelial
847 basal stem cell multipotency in prostate organogenesis and homeostasis. *Biology Open*,
848 *8*(10). https://doi.org/10.1242/bio.045724
849 Joseph, D. B., Henry, G. H., Malewska, A., Iqbal, N. S., Ruetten, H. M., Turco, A. E., Abler, L. L.,
850 Sandhu, S. K., Cadena, M. T., Malladi, V. S., Reese, J. C., Mauck, R. J., Gahan, J. C.,
851 Hutchinson, R. C., Roehrborn, C. G., Baker, L. A., Vezina, C. M., & Strand, D. W. (2020).
852 Urethral luminal epithelia are castration-insensitive cells of the proximal prostate. *The*
853 *Prostate*. https://doi.org/10.1002/pros.24020
854 Karthaus, W. R., Hofree, M., Choi, D., Linton, E. L., Turkekul, M., Bejnood, A., Carver, B.,
855 Gopalan, A., Abida, W., Laudone, V., Biton, M., Chaudhary, O., Xu, T., Masilionis, I.,
856 Manova, K., Mazutis, L., Pe'er, D., Regev, A., & Sawyers, C. L. (2020). Regenerative
857 potential of prostate luminal cells revealed by single-cell analysis. *Science*, *368*(6490),
858 497–505. https://doi.org/10.1126/science.aay0267
859 Karthaus, W. R., Iaquinta, P. J., Drost, J., Gracanin, A., van Boxtel, R., Wongvipat, J., Dowling, C.
860 M., Gao, D., Begthel, H., Sachs, N., Vries, R. G. J., Cuppen, E., Chen, Y., Sawyers, C. L., &
861 Clevers, H. C. (2014). Identification of multipotent luminal progenitor cells in human
862 prostate organoid cultures. *Cell*, *159*(1), 163–175.
863 https://doi.org/10.1016/j.cell.2014.08.017
864 Keil, K. P., Mehta, V., Abler, L. L., Joshi, P. S., Schmitz, C. T., & Vezina, C. M. (2012). Visualization
865 and quantification of mouse prostate development by in situ hybridization.

866 *Differentiation; Research in Biological Diversity*, *84*(3), 232–239.
867 https://doi.org/10.1016/j.diff.2012.07.005
868 Keita, M., Bachvarova, M., Morin, C., Plante, M., Gregoire, J., Renaud, M.-C., Sebastianelli, A.,
869 Trinh, X. B., & Bachvarov, D. (2013). The RUNX1 transcription factor is expressed in
870 serous epithelial ovarian carcinoma and contributes to cell proliferation, migration and
871 invasion. *Cell Cycle (Georgetown, Tex.)*, *12*(6), 972–986.
872 https://doi.org/10.4161/cc.23963
873 Kruithof-de Julio, M., Shibata, M., Desai, N., Reynon, M., Halili, M. V., Hu, Y.-P., Price, S. M.,
874 Abate-Shen, C., & Shen, M. M. (2013). Canonical Wnt signaling regulates Nkx3.1
875 expression and luminal epithelial differentiation during prostate organogenesis.
876 *Developmental Dynamics : An Official Publication of the American Association of*
877 *Anatomists*, *242*(10), 1160–1171. https://doi.org/10.1002/dvdy.24008
878 Kwon, O.-J., Zhang, L., Ittmann, M. M., & Xin, L. (2014). Prostatic inflammation enhances basal-
879 to-luminal differentiation and accelerates initiation of prostate cancer with a basal cell
880 origin. *Proceedings of the National Academy of Sciences of the United States of America*,
881 *111*(5), E592-600. https://doi.org/10.1073/pnas.1318157111
882 Kwon, O.-J., Zhang, L., & Xin, L. (2016). Stem Cell Antigen-1 Identifies a Distinct Androgen-
883 Independent Murine Prostatic Luminal Cell Lineage with Bipotent Potential. *STEM CELLS*,
884 *34*(1), 191–202. https://doi.org/10.1002/stem.2217
885 Lawson, D. A., Xin, L., Lukacs, R. U., Cheng, D., & Witte, O. N. (2007). Isolation and functional
886 characterization of murine prostate stem cells. *Proceedings of the National Academy of*

887 *Sciences of the United States of America*, *104*(1), 181–186.
888 https://doi.org/10.1073/pnas.0609684104
889 Leong, K. G., Wang, B.-E., Johnson, L., & Gao, W.-Q. (2008). Generation of a prostate from a
890 single adult stem cell. *Nature*, *456*(7223), 804–808.
891 https://doi.org/10.1038/nature07427
892 Lie-A-Ling, M., Mevel, R., Patel, R., Blyth, K., Baena, E., Kouskoff, V., & Lacaud, G. (2020). RUNX1
893 Dosage in Development and Cancer. *Molecules and Cells*, *43*(2), 126–138.
894 https://doi.org/10.14348/molcells.2019.0301
895 Lopes, E. S., Foster, B. A., Donjacour, A. A., & Cunha, G. R. (1996). Initiation of secretory activity
896 of rat prostatic epithelium in organ culture. *Endocrinology*, *137*(10), 4225–4234.
897 https://doi.org/10.1210/endo.137.10.8828481
898 Luche, H., Weber, O., Nageswara Rao, T., Blum, C., & Fehling, H. J. (2007). Faithful activation of
899 an extra-bright red fluorescent protein in 'knock-in' Cre-reporter mice ideally suited for
900 lineage tracing studies. *European Journal of Immunology*, *37*(1), 43–53.
901 https://doi.org/10.1002/eji.200636745
902 Lukacs, R. U., Goldstein, A. S., Lawson, D. A., Cheng, D., & Witte, O. N. (2010). Isolation,
903 cultivation and characterization of adult murine prostate stem cells. *Nature Protocols*,
904 *5*(4), 702–713. https://doi.org/10.1038/nprot.2010.11
905 McAuley, E., Moline, D., VanOpstall, C., Lamperis, S., Brown, R., & Vander Griend, D. J. (2019).
906 Sox2 Expression Marks Castration-Resistant Progenitor Cells in the Adult Murine
907 Prostate. *Stem Cells (Dayton, Ohio)*, *37*(5), 690–700. https://doi.org/10.1002/stem.2987

908 McGinnis, C. S., Murrow, L. M., & Gartner, Z. J. (2019). DoubletFinder: Doublet Detection in
909 Single-Cell RNA Sequencing Data Using Artificial Nearest Neighbors. *Cell Systems*, *8*(4),
910 329-337.e4. https://doi.org/10.1016/j.cels.2019.03.003
911 McGinnis, C. S., Patterson, D. M., Winkler, J., Conrad, D. N., Hein, M. Y., Srivastava, V., Hu, J. L.,
912 Murrow, L. M., Weissman, J. S., Werb, Z., Chow, E. D., & Gartner, Z. J. (2019). MULTI-
913 seq: Sample multiplexing for single-cell RNA sequencing using lipid-tagged indices.
914 *Nature Methods*, *16*(7), 619–626. https://doi.org/10.1038/s41592-019-0433-8
915 McInnes, L., Healy, J., & Melville, J. (2018). UMAP: Uniform Manifold Approximation and
916 Projection for Dimension Reduction. *ArXiv:1802.03426 [Cs, Stat]*.
917 http://arxiv.org/abs/1802.03426
918 McNeal, J. E. (1981). The zonal anatomy of the prostate. *The Prostate*, *2*(1), 35–49.
919 https://doi.org/10.1002/pros.2990020105
920 Mevel, R., Draper, J. E., Lie-a-Ling, M., Kouskoff, V., & Lacaud, G. (2019). RUNX transcription
921 factors: Orchestrators of development. *Development*, *146*(17), dev148296.
922 https://doi.org/10.1242/dev.148296
923 Ousset, M., Van Keymeulen, A., Bouvencourt, G., Sharma, N., Achouri, Y., Simons, B. D., &
924 Blanpain, C. (2012). Multipotent and unipotent progenitors contribute to prostate
925 postnatal development. *Nature Cell Biology*, *14*(11), 1131–1138.
926 https://doi.org/10.1038/ncb2600
927 Pignon, J.-C., Grisanzio, C., Geng, Y., Song, J., Shivdasani, R. A., & Signoretti, S. (2013). P63-
928 expressing cells are the stem cells of developing prostate, bladder, and colorectal

929 epithelia. *Proceedings of the National Academy of Sciences of the United States of*
930 *America*, *110*(20), 8105–8110. https://doi.org/10.1073/pnas.1221216110
931 Planagumà, J., Díaz-Fuertes, M., Gil-Moreno, A., Abal, M., Monge, M., García, A., Baró, T.,
932 Thomson, T. M., Xercavins, J., Alameda, F., & Reventós, J. (2004). A differential gene
933 expression profile reveals overexpression of RUNX1/AML1 in invasive endometrioid
934 carcinoma. *Cancer Research*, *64*(24), 8846–8853. https://doi.org/10.1158/0008-
935 5472.CAN-04-2066
936 Planagumà, J., Gonzalez, M., Doll, A., Monge, M., Gil-Moreno, A., Baró, T., García, A., Xercavins,
937 J., Alameda, F., Abal, M., & Reventós, J. (2006). The up-regulation profiles of
938 p21WAF1/CIP1 and RUNX1/AML1 correlate with myometrial infiltration in endometrioid
939 endometrial carcinoma. *Human Pathology*, *37*(8), 1050–1057.
940 https://doi.org/10.1016/j.humpath.2006.03.007
941 Richardson, G. D., Robson, C. N., Lang, S. H., Neal, D. E., Maitland, N. J., & Collins, A. T. (2004).
942 CD133, a novel marker for human prostatic epithelial stem cells. *Journal of Cell Science*,
943 *117*(16), 3539–3545. https://doi.org/10.1242/jcs.01222
944 Riggio, A. I., & Blyth, K. (2017). The enigmatic role of RUNX1 in female-related cancers—Current
945 knowledge & future perspectives. *The FEBS Journal*, *284*(15), 2345–2362.
946 https://doi.org/10.1111/febs.14059
947 Samokhvalov, I. M., Samokhvalova, N. I., & Nishikawa, S. (2007). Cell tracing shows the
948 contribution of the yolk sac to adult haematopoiesis. *Nature*, *446*(7139), 1056–1061.
949 https://doi.org/10.1038/nature05725

950 Scheitz, C. J. F., Lee, T. S., McDermitt, D. J., & Tumbar, T. (2012). Defining a tissue stem cell-
951 driven Runx1/Stat3 signalling axis in epithelial cancer. *The EMBO Journal*, *31*(21), 4124–
952 4139. https://doi.org/10.1038/emboj.2012.270
953 Scheitz, C. J. F., & Tumbar, T. (2013). New insights into the role of Runx1 in epithelial stem cell
954 biology and pathology. *Journal of Cellular Biochemistry*, *114*(5), 985–993.
955 https://doi.org/10.1002/jcb.24453
956 Shen, M. M., & Abate-Shen, C. (2010). Molecular genetics of prostate cancer: New prospects for
957 old challenges. *Genes & Development*, *24*(18), 1967–2000.
958 https://doi.org/10.1101/gad.1965810
959 Sroczynska, P., Lancrin, C., Kouskoff, V., & Lacaud, G. (2009). The differential activities of Runx1
960 promoters define milestones during embryonic hematopoiesis. *Blood*, *114*(26), 5279–
961 5289. https://doi.org/10.1182/blood-2009-05-222307
962 Sugimura, Y., Cunha, G. R., & Donjacour, A. A. (1986a). Morphogenesis of ductal networks in the
963 mouse prostate. *Biology of Reproduction*, *34*(5), 961–971.
964 https://doi.org/10.1095/biolreprod34.5.961
965 Sugimura, Y., Cunha, G. R., & Donjacour, A. A. (1986b). Morphological and histological study of
966 castration-induced degeneration and androgen-induced regeneration in the mouse
967 prostate. *Biology of Reproduction*, *34*(5), 973–983.
968 Takayama, K., Suzuki, T., Tsutsumi, S., Fujimura, T., Urano, T., Takahashi, S., Homma, Y.,
969 Aburatani, H., & Inoue, S. (2015). RUNX1, an androgen- and EZH2-regulated gene, has
970 differential roles in AR-dependent and -independent prostate cancer. *Oncotarget*, *6*(4),
971 2263–2276. https://doi.org/10.18632/oncotarget.2949

Thambyrajah, R., Mazan, M., Patel, R., Moignard, V., Stefanska, M., Marinopoulou, E., Li, Y., Lancrin, C., Clapes, T., Möröy, T., Robin, C., Miller, C., Cowley, S., Göttgens, B., Kouskoff, V., & Lacaud, G. (2016). GFI1 proteins orchestrate the emergence of haematopoietic stem cells through recruitment of LSD1. *Nature Cell Biology*, *18*(1), 21–32. https://doi.org/10.1038/ncb3276

Tika, E., Ousset, M., Dannau, A., & Blanpain, C. (2019). Spatiotemporal regulation of multipotency during prostate development. *Development*, dev.180224. https://doi.org/10.1242/dev.180224

Tirosh, I., Izar, B., Prakadan, S. M., Wadsworth, M. H., Treacy, D., Trombetta, J. J., Rotem, A., Rodman, C., Lian, C., Murphy, G., Fallahi-Sichani, M., Dutton-Regester, K., Lin, J.-R., Cohen, O., Shah, P., Lu, D., Genshaft, A. S., Hughes, T. K., Ziegler, C. G. K., … Garraway, L. A. (2016). Dissecting the multicellular ecosystem of metastatic melanoma by single-cell RNA-seq. *Science*, *352*(6282), 189–196. https://doi.org/10.1126/science.aad0501

Toivanen, R., Mohan, A., & Shen, M. M. (2016). Basal Progenitors Contribute to Repair of the Prostate Epithelium Following Induced Luminal Anoikis. *Stem Cell Reports*, *0*(0). https://doi.org/10.1016/j.stemcr.2016.03.007

Toivanen, R., & Shen, M. M. (2017). Prostate organogenesis: Tissue induction, hormonal regulation and cell type specification. *Development (Cambridge, England)*, *144*(8), 1382–1398. https://doi.org/10.1242/dev.148270

Tsujimura, A., Koikawa, Y., Salm, S., Takao, T., Coetzee, S., Moscatelli, D., Shapiro, E., Lepor, H., Sun, T.-T., & Wilson, E. L. (2002). Proximal location of mouse prostate epithelial stem

993 cells. *The Journal of Cell Biology*, *157*(7), 1257–1265.
994 https://doi.org/10.1083/jcb.200202067
995 van Bragt, M. P. A., Hu, X., Xie, Y., & Li, Z. (2014). RUNX1, a transcription factor mutated in
996 breast cancer, controls the fate of ER-positive mammary luminal cells. *ELife*, *3*, e03881.
997 https://doi.org/10.7554/eLife.03881
998 Wang, B., Wang, X., Long, J. E., Eastham-Anderson, J., Firestein, R., & Junttila, M. R. (2015).
999 Castration-Resistant Lgr5+ Cells Are Long-Lived Stem Cells Required for Prostatic
1000 Regeneration. *Stem Cell Reports*, *4*(5), 768–779.
1001 https://doi.org/10.1016/j.stemcr.2015.04.003
1002 Wang, X., Kruithof-de Julio, M., Economides, K. D., Walker, D., Yu, H., Halili, M. V., Hu, Y.-P.,
1003 Price, S. M., Abate-Shen, C., & Shen, M. M. (2009). A luminal epithelial stem cell that is a
1004 cell of origin for prostate cancer. *Nature*, *461*(7263), 495–500.
1005 https://doi.org/10.1038/nature08361
1006 Wang, X.-D., Wang, B.-E., Soriano, R., Zha, J., Zhang, Z., Modrusan, Z., Cunha, G. R., & Gao, W.-
1007 Q. (2007). Expression profiling of the mouse prostate after castration and hormone
1008 replacement: Implication of H-cadherin in prostate tumorigenesis. *Differentiation;*
1009 *Research in Biological Diversity*, *75*(3), 219–234. https://doi.org/10.1111/j.1432-
1010 0436.2006.00135.x
1011 Wang, Y., Hayward, S., Cao, M., Thayer, K., & Cunha, G. (2001). Cell differentiation lineage in the
1012 prostate. *Differentiation; Research in Biological Diversity*, *68*(4–5), 270–279.
1013 Wolf, F. A., Hamey, F. K., Plass, M., Solana, J., Dahlin, J. S., Göttgens, B., Rajewsky, N., Simon, L.,
1014 & Theis, F. J. (2019). PAGA: Graph abstraction reconciles clustering with trajectory

1015 inference through a topology preserving map of single cells. *Genome Biology*, *20*(1), 59.
1016 https://doi.org/10.1186/s13059-019-1663-x
1017 Xin, L., Lawson, D. A., & Witte, O. N. (2005). The Sca-1 cell surface marker enriches for a
1018 prostate-regenerating cell subpopulation that can initiate prostate tumorigenesis.
1019 *Proceedings of the National Academy of Sciences of the United States of America*,
1020 *102*(19), 6942–6947. https://doi.org/10.1073/pnas.0502320102
1021 Yokomizo, T., Yamada-Inagawa, T., Yzaguirre, A. D., Chen, M. J., Speck, N. A., & Dzierzak, E.
1022 (2012). Whole-mount three-dimensional imaging of internally localized immunostained
1023 cells within mouse embryos. *Nature Protocols*, *7*(3), 421–431.
1024 https://doi.org/10.1038/nprot.2011.441
1025 Yoo, Y. A., Roh, M., Naseem, A. F., Lysy, B., Desouki, M. M., Unno, K., & Abdulkadir, S. A. (2016).
1026 Bmi1 marks distinct castration-resistant luminal progenitor cells competent for prostate
1027 regeneration and tumour initiation. *Nature Communications*, *7*, 12943.
1028 https://doi.org/10.1038/ncomms12943
1029 Zhang, D., Zhao, S., Li, X., Kirk, J. S., & Tang, D. G. (2018). Prostate Luminal Progenitor Cells in
1030 Development and Cancer. *Trends in Cancer*, *4*(11), 769–783.
1031 https://doi.org/10.1016/j.trecan.2018.09.003
1032

1033 ## MAIN FIGURE LEGENDS

1034 **Figure 1. RUNX1 marks a subpopulation of mouse proximal prostate luminal cells (PLCs).**

1035 (**A**) Co-immunostaining of RUNX1, NKX3.1, CDH1 in the mouse Anterior Prostate (AP). Higher

1036 magnification images of (i) proximal AP and (ii) distal AP are shown. Arrows indicate RUNX1$^+$

1037 NKX3.1$^-$ cells, arrowheads show RUNX1$^-$ NKX3.1$^+$ cells. Scale bars: 500µm (yellow) and 50µm

1038 (white). (**B**) Quantification of RUNX1 and NKX3.1 nuclear intensity ($\log_{10}$) in CDH1$^+$ epithelial

1039 cells by QBIC in proximal and distal AP. *n* = 6-8 mice. (**C, D**) Flow-cytometry analysis of P2-

1040 *Runx1*:RFP mice, and corresponding quantification of the percentages of RFP$^+$ and RFP cells in

1041 the basal and luminal fractions of the proximal and distal AP. *n* = 7 mice. (**E**) Experimental

1042 strategy to grow organoids from sorted RFP$^+$ and RFP cells from the basal (CD49f^{high}) and

1043 luminal (CD24^{high}) lineages of P2-*Runx1*:RFP mouse reporters. (**F**) Organoid Forming Capacity

1044 (OFC) of RFP$^+$ and RFP$^-$ basal and luminal sorted cells after 7 days in culture. *n* = 4 mice. (**G**)

1045 Whole-mount immunostaining of unipotent K5$^+$, unipotent K8$^+$ or multipotent K5$^+$ K8$^+$

1046 organoids. Scale bar: 50 µm. (**H**) Quantification of the type of organoids characterized by whole-

1047 mount immunostaining, as in G. Numbers of organoids quantified are shown above the graph. *p*

1048 value is indicated for the proportion of K8$^+$ organoids between Proximal AP Luminal RFP$^+$ versus

1049 RFP$^-$ derived subset. Other comparisons were not statistically significant. *n* = 2 mice per group.

1050 Source files are available in Figure 1—source data 1.

1051

1052 **Figure 2. RUNX1 expressing cells are enriched in the castrated prostate epithelium.**

1053 (**A**) P2-*Runx1*:RFP reporter mice were surgically castrated between 6 to 12 weeks of age and

1054 analyzed at least 4 weeks post-castration. (**B**, **C**) Flow-cytometry analysis and corresponding

1055 quantification of the proportion of RFP$^+$ and RFP$^-$ cells in the EPCAM$^+$ fraction of intact and
1056 castrated prostates of P2-*Runx1*:RFP mice. *n* = 3 mice per group. Int: Intact, Cas: Castrated. (**D**)
1057 Co-immunostaining of RUNX1, NKX3.1, CDH1 in the castrated wild-type mouse prostate. Higher
1058 magnification images of (i) proximal, (ii) intermediate and (iii) distal AP are shown. Arrows
1059 indicate RUNX1$^-$ NKX3.1$^+$ cells, arrowheads show a luminal cell co-stained for RUNX1 and
1060 NKX3.1. Amp: ampullary gland. Scale bars: 500 µm (yellow) and 50 µm (white). Int: Intact, Cas:
1061 Castrated. (**E**) Co-immunostaining of RUNX1 and TROP2 showing colocalization of the 2 markers
1062 in both proximal (bottom) and distal (top) castrated AP. Scale bars: 50 µm (white). Source files
1063 are available in Figure 2—source data 1.
1064
1065 **Figure 3. scRNA-seq profiling of intact and castrated *Runx1*$^+$ cells reveals transcriptomic**
1066 **similarity between proximal luminal cells and castration-resistant cells.**
1067 (**A**) Experimental strategy for scRNA-seq on RFP$^+$ and RFP$^-$ cells individually dissected lobes of
1068 intact and castrated prostates isolated from P2-*Runx1*:RFP reporter mice. (**B**) UMAP
1069 visualization (left) and graph-abstracted representation (PAGA, right) of prostate epithelial cells
1070 (*n* = 3,825 cells from 3 independent experiments). Colors represent different clusters. In PAGA,
1071 clusters are linked by weighted edges that represent a statistical measure of connectivity. (**C**)
1072 Dot plot showing the expression of selected marker genes associated with each cluster. (**D-H**)
1073 UMAP visualization of prostate epithelial cells. Cells in **D** and **G** are colored by a gradient of log-
1074 normalized expression levels for each gene indicated. Cell colors in **E** represent the treatment of
1075 origin (intact, castrated), in **F** individual lobes of origin (AP, DLP, VP), and in **H** RFP FACS gate of
1076 origin (RFP$^+$, RFP$^-$).

1077

1078 **Figure 4. Lineage-tracing of *Runx1* expressing cells establishes the intrinsic castration-**

1079 **resistant properties of the proximal luminal lineage.**

1080 (**A**) Schematic summary of the genetic lineage tracing system employed. (**B**) Experimental

1081 strategy for lineage-tracing experiments. (**C**) Co-immunostaining of RFP, RUNX1, CDH1 in the

1082 proximal AP. Arrows indicate RFP labelled RUNX1$^+$ cells. Scale bar: 50 µm. (**D**) Quantification of

1083 the percentage of epithelial RFP$^+$ cells in proximal and distal regions of the prostate in intact (*n*

1084 = 5), castrated (*n* = 4) and regenerated (*n* = 4) mice. (**E**) Quantification of the percentage of

1085 epithelial RFP$^+$ cells in intact (*n* = 5), castrated (*n* = 5) and regenerated (*n* = 4) mice. (**F**) Co-

1086 immunostaining of RFP, K5, K8 in the proximal AP, distal AP, and DLVP (DLP + VP). Arrowheads

1087 indicate RFP labelled basal cells (K5$^+$) found in distal AP, the white arrow indicates a luminal

1088 (K8$^+$) RFP$^+$ clone made of 2 cells. Scale bar: 50 µm. (**G**) Quantification of the percentage of

1089 epithelial RFP$^+$ clones comprising between 2 to 4 cells in intact (*n* = 5), castrated (*n* = 5) and

1090 regenerated (*n* = 4) mice. (**H, I**) Quantification of the percentage of RFP$^+$ cells being K5$^+$ or K8$^+$ in

1091 **H**, or NKX3.1$^+$ or NKX3.1$^-$ in **I,** in intact (*n* = 5), castrated (*n* = 5) and regenerated (*n* = 4) mice. Int:

1092 Intact, Cas: Castrated, Rgn: Regenerated. Source files are available in Figure 4—source data 1.

1093

1094 **Figure 5. RUNX1 marks proximal cells during embryonic prostate development.**

1095 (**A-C**) Co-immunostainings of the mouse urogenital sinus at E18.5 for RUNX1, K5, K8 in **A**,

1096 RUNX1, p63, CDH1 in **B**, RUNX1, NKX3.1, CDH1 in **C**. Scale bar: 50 µm. (**D**) Co-immunostainings

1097 of RUNX1, NKX3.1, CDH1 at postnatal (P) day 14. Higher magnification images of (p) proximal,

1098 (i) intermediate, and (d) distal regions are shown. Scale bars: 200 µm (yellow) and 50 µm

1099 (white). Amp: ampullary gland; Sv: seminal vesicles; Ur: urethra; p: proximal; i: intermediate; d:
1100 distal. (**E**) Scheme of the protocol to culture *ex vivo* explants of mouse UGS harvested at E15.5.
1101 (**F**) Representative images of UGS explants at E15.5 (day 0), day 3, day 5 and day 7 of culture
1102 showing the formation of premature prostate buds. (**G**) Co-immunostaining of RUNX1, NKX3.1,
1103 CDH1 in UGS explants harvested at day 0, day 1, day 2 and day 7. Higher magnification images
1104 of each square (left) are shown for each time point. Chevron arrows show $RUNX1^+$ $NKX3.1^+$
1105 cells, closed arrows indicate $RUNX1^-$ $NKX3.1^+$ cells, arrowheads show $RUNX1^+$ $NKX3.1^-$ cells.
1106 Scale bars: 200 µm (yellow) and 50 µm (white). (**H**) Quantification of RUNX1 and NKX3.1 nuclear
1107 intensity (log_{10}) in $CDH1^+$ epithelial cells of UGS explants by QBIC. Quantification was performed
1108 within the boundaries delimited in **G** by dotted lines, at day 0 (*n* = 3 explants), day 1 (*n* = 7
1109 explants), day 2 (*n* = 6 explants) and day 7 (*n* = 6 explants). Source files are available in Figure
1110 5—source data 1.
1111
1112 **Figure 6. scRNA-seq of UGS explant cultures shows specification of the proximal luminal**
1113 **lineage during embryonic prostate development.**
1114 (**A**) Experimental strategy for scRNA-seq of UGS explant cultures at day 0, day 1, day 3 and day
1115 6. (**B**, **C**) Force directed visualization of the developing prostatic epithelium in UGS explant
1116 cultures. In **B** cells are colored by experimental time points, and in **C** cells are colored by
1117 clusters. (**D**) PAGA representation of the clusters as in **C**. Weighted edges between cluster
1118 nodes represent a statistical measure of connectivity. (**E**) Fraction of cells per cluster at each
1119 experimental time point, displaying a progressive cellular diversification. (**F-H**) PAGA
1120 representations with cluster nodes colored by a gradient representing the mean log-normalized

1121 expression levels of each gene. (**I**) Force directed visualization of the developing prostatic
1122 epithelium in UGS explant cultures. Color gradient represents AUC scores per cell. Per-cell AUC
1123 scores were calculated using the 'AUCell' package. Gene signatures for 'Lum-D' (left) and 'Basal'
1124 (right) were generated using the list of differentially upregulated genes previously obtained
1125 from our adult mouse prostate clusters.
1126
1127 **Figure 7. RUNX1$^+$ cells contribute to the establishment of the proximal luminal lineage during**
1128 **embryonic prostate development.**
1129 (**A**) Strategy for lineage-tracing of RUNX1$^+$ cells in UGS explant cultures. Tamoxifen was applied
1130 on day 0 and day 1 and washed out on day 2. (**B, C**) Co-immunostaining of RFP, RUNX1, CDH1 in
1131 UGS explants harvested at day 2 (**B**) and day 7 (**C**). Higher magnification images of proximal (i)
1132 and (ii) distal regions are shown for day 7. Arrows show RFP$^+$ RUNX1-low cells, arrowheads
1133 show RFP$^+$ RUNX1$^+$ cells. Scale bars: 200 µm (yellow) and 50 µm (white). (**C**) Quantification of
1134 the percentage of epithelial RUNX1$^+$ cells in the RFP subset at day 2 (n = 7) and day 7 (n = 3) of
1135 UGS explant cultures. Quantification was performed within the boundaries delimited in **B** by
1136 dotted lines. (**E, F**) Co-immunostaining of RFP, NKX3.1, CDH1 in UGS explants harvested at day 2
1137 (**E**) and day 7 (**F**). Higher magnification images of (i) proximal and (ii) distal regions are shown
1138 for day 7. Arrows show RFP$^+$ NKX3.1$^+$ cells, arrowheads show RFP$^+$ NKX3.1$^-$ cells. Scale bars: 200
1139 µm (yellow) and 50 µm (white). (**G**) Quantification of the percentage of epithelial NKX3.1$^+$ cells
1140 in the RFP subset at day 2 (n = 6) and day 7 (n = 4) of UGS explant cultures. Quantification was
1141 performed within the boundaries delimited in **F** by dotted lines. (**H, I**) Co-immunostaining of
1142 RFP, K4, CDH1 in UGS explants harvested at day 2 (**H**) and day 7 (**I**). Higher magnification images

1143 of (i) proximal and (ii) distal regions are shown for day 7. Arrows show RFP$^+$ K4 cells,

1144 arrowheads show RFP$^+$ K4$^+$ cells. Scale bars: 200 µm (yellow) and 50 µm (white). (**J**)

1145 Quantification of the percentage of epithelial K4$^+$ cells in the RFP subset at day 2 (*n* = 3) and day

1146 7 (*n* = 3) of UGS explant cultures. Quantification was performed within the boundaries

1147 delimited in **I** by dotted lines. Source files are available in Figure 7—source data 1.

1148

1149 **Figure 1—figure supplement 1. RUNX1 is enriched in the mouse prostate epithelium.**

1150 (**A**) Co-immunostaining of RUNX1, NKX3.1, CDH1 in the mouse DLP (top) and VP (bottom).

1151 Closed arrows indicate RUNX1$^+$ NKX3.1$^-$ cells, chevron arrows indicate rare RUNX1$^+$ NKX3.1$^+$

1152 cells, arrowheads show RUNX1$^-$ NKX3.1$^+$ cells. Scale bars: 50 µm. (**B**) Quantification of RUNX1

1153 and NKX3.1 nuclear intensity ($\log_{10}$) in CDH1+ epithelial cells by QBIC in proximal DLP (*n* = 3),

1154 distal DLP (*n* = 8), proximal VP (*n* = 3) and distal VP (*n* = 8). (**C**) H&E staining of the mouse AP.

1155 Higher magnification images of (i) proximal AP and (ii) distal regions are shown. Arrows show

1156 typical proximal luminal cells with condensed nuclei and cytoplasm, arrowheads show typical

1157 distal secretory luminal cells with enlarged cytoplasm and strong pink eosinophilic staining.

1158 Scale bars: 200 µm (blue) and 50 µm (black). Source files are available in Figure 1—figure

1159 supplement 1—source data 1.

1160

1161 **Figure 1—figure supplement 2. *Runx1* expression is mediated by the P2 promoter in the**

1162 **mouse prostate epithelium.**

1163 (**A**) Schematic diagrams of the P2-*Runx1*:RFP reporter allele (top), *Runx1* WT allele (middle), and

1164 P1-*Runx1*:GFP reporter allele (bottom). In P2-*Runx1*:RFP or P1-*Runx1*:GFP mice, expression of

1165 RFP or GFP is directed by *Runx1* proximal P2 or distal P1 promoter respectively. WT *Runx1*
1166 expression is directed by the remaining WT allele. (**B**) Flow-cytometry analysis of the epithelial
1167 EPCAM$^+$ fraction of WT, P2-*Runx1*:RFP and P1-*Runx1*:GFP mice. Percentages are indicated in
1168 each quadrant gates. (**C**) Confocal images indicating P2-*Runx1*:RFP signal in the glandular
1169 epithelium (top), while P1-*Runx1*:GFP (bottom) activity is detected in the surrounding stroma.
1170 Scale bar: 50 µm. (**D**) Flow-cytometry analysis of P2-*Runx1*:RFP mice, and corresponding
1171 quantification of the percentages of RFP$^+$ and RFP$^-$ cells in the basal and luminal fractions of DLP
1172 (*n* = 4 mice) and VP (*n* = 4 mice) lobes. Source files are available in Figure 1—figure supplement
1173 2—source data 1.
1174
1175 **Figure 1—figure supplement 3. Characterization of P2Runx1:RFP derived mouse prostate**
1176 **organoids.**
1177 (**A**) Organoid Forming Capacity (OFC) of RFP$^+$ and RFP$^-$ basal and luminal sorted cells from DLP
1178 (left) and VP (right) cultured for 7 days. *n* = 4 mice. (**B**) Quantification of organoid morphologies
1179 determined by brightfield assessment. *p* values are indicated only for statistically significant ($p <$
1180 0.05) comparisons between RFP$^+$ versus RFP$^-$ derived subsets. *n* = 4 mice. (**C**) Quantification of
1181 the type of organoids (pink: unipotent K5$^+$, green: unipotent K8$^+$, orange: multipotent K5$^+$ K8$^+$
1182 organoids) characterized by whole-mount immunostaining. *p* value is indicated for the
1183 proportion of K5$^+$K8$^+$ organoids between VP Luminal RFP$^+$ versus RFP$^-$ derived subset. Other
1184 comparisons were not statistically significant. *n* = 2 mice. (**D**) Quantification of organoid
1185 morphologies according to the type of organoids (unipotent K5$^+$, unipotent K8$^+$, multipotent K5$^+$
1186 K8$^+$). Results are shown for luminal proximal and distal AP derived organoids. *n* = 2 mice.

1187 Numbers of organoids quantified are shown above the graph. Two-way ANOVA using Tukey's
1188 multiple comparisons test was used for statistical analysis. (**E**) Quantification of the organoid
1189 area estimated from maximum projection of stacked images from basal (left) and luminal (right)
1190 fractions of the proximal AP. Numbers of organoids quantified are shown above the graph.
1191 Two-tailed Mann-Whitney test was used for statistical analysis. *n* = 2 mice. Source files are
1192 available in Figure 1—figure supplement 3—source data 1.
1193
1194 **Figure 2—figure supplement 1. Characterization of RUNX1 expression in the castrated mouse**
1195 **prostate.**
1196 (**A**) Flow cytometry analysis and corresponding quantifications of the basal and luminal EPCAM$^+$
1197 fraction from AP, DLP and VP lobes of castrated P2-*Runx1*:RFP mice (*n* = 3). (**B, C**) Co-
1198 immunostaining of RUNX1, NKX3.1, CDH1 in castrated DLP (**B**) and VP (**C**) lobes. Scale bars: 50
1199 µm (white). Source files are available in Figure 2—figure supplement 2—source data 1.
1200
1201 **Figure 3—figure supplement 1. Pre-processing of the scRNA-seq dataset of adult intact and**
1202 **castrated mouse prostates.**
1203 (**A**) UMAP visualization in MULTI-seq barcodes space for each independent experiment (Run 1:
1204 left, Run 2: middle, Run 3: right) before (top) and after (bottom) quality control and barcode
1205 filtration (see Methods for details). (**B**) UMAP visualization of the integrated batch-corrected
1206 dataset (*n* = 4,499 cells from 3 independent experiments). Colors represent different clusters.
1207 (**C**) UMAP visualization of the integrated batch-corrected dataset split and colored by individual
1208 experiment (Run 1: left, Run 2: middle, Run 3: right). (**D**, **E**) Example key marker genes used for

1209 cell type characterization. (**D**) UMAP visualization of the integrated batch-corrected dataset.
1210 Cells are colored by a gradient of log-normalized expression levels for each gene indicated. (**E**)
1211 Dot plot showing the expression of selected marker genes associated with each cluster. Cells
1212 corresponding to the prostatic clusters were kept for downstream analyses.
1213
1214 **Figure 3—figure supplement 2. Characterization of the scRNA-seq prostate epithelial subset.**
1215 (**A**-**D**) Number of cells present in the prostate epithelial subset. In **A** colors correspond to
1216 phenotypic sorted populations, in **B** treatment of origin, in **C** RFP FACS gate of origin, in **D**
1217 individual lobes. (**E, G**) UMAP visualization of prostate epithelial cells. Cells in **E** are colored by
1218 clusters. Clusters 0, 1 and 5 were merged together. In **F** and **G** colors represent phenotypic
1219 sorted populations. (**H-J**) Cells are colored by a gradient of log-normalized expression levels for
1220 each gene. Canonical epithelial markers are shown in **H**, luminal lineage markers in **I**, and basal
1221 lineage markers in **J**.
1222
1223 **Figure 3—figure supplement 3. Characterization of the scRNA-seq prostate epithelial dataset.**
1224 (**A**) Heatmap of the 10 most differentially upregulated genes per cluster. (**B**, **C**) Sankey diagrams
1225 summarizing the proportion of cells and between phenotypic groups. (**D**, **E**) Cells are colored by
1226 a gradient of log-normalized expression levels for each gene. (**D**) shows the expression of Ly6
1227 family members, and in **E** RUNX family members are shown.
1228
1229 **Figure 3—figure supplement 4. Gene Ontology and differential expression analysis within the**
1230 **scRNA-seq prostate epithelial dataset.**

1231 Bar plots of the 8 most significantly (g:Profiler adjusted p-value < 0.05) enriched gene ontology
1232 (GO) terms (GO:BP, Biological Processes) using the list of differentially upregulated genes
1233 specific to (**A**) Lum-A, (**B**) Lum-B, (**C**) Lum-C, (**D**) Lum-D, (**E**) Lum-E, (**F**) Lum-F, and (**G**) Basal
1234 clusters. (**H, I**) 15 most enriched GO terms (g:Profiler adjusted p-value < 0.05) for genes
1235 upregulated in the Lum-D cluster against combined Lum-A, Lum-B and Lum-C clusters in **H**.
1236 Results of the opposite comparison are shown in **I**. (**J**) Violin plots showing the expression levels
1237 of specific genes within the Lum-D cluster. Data are split and colored by treatment for each
1238 lobe. The expression of *Krt4*, *Tacstd2*/*Trop2* and *Runx1* does not vary upon treatment, while
1239 Androgen Receptor (AR) regulated genes such as *Psca* and *Tspan1* are downregulated after
1240 castration.
1241
1242 **Figure 4—figure supplement 1. Lineage tracing of RUNX1 expressing cells labelled in intact**
1243 **mice.**
1244 (**A**) Scheme of the tamoxifen labelling strategy to evaluate the labelling efficiency of *Runx1*
1245 expressing cells. (**B**) Flow-cytometry analysis of intact (*n* = 2), castrated (*n* = 2), and regenerated
1246 (*n* = 2) *Runx1*^{CreER} *Rosa26*$^{LSL\text{-}RFP}$ mice, and corresponding quantification of the percentage of RFP^{+}
1247 cells in the epithelial EPCAM^{+} fraction. (**C**) Estimated absolute number of epithelial RFP^{+} cells in
1248 intact (*n* = 5) and castrated (*n* = 5) and regenerated (*n* = 4) prostates based on IHC
1249 quantifications. Int: Intact, Cas: Castrated, Rgn: Regenerated. (**D**) Quantification of the
1250 percentage of epithelial RFP^{+} cells being K4^{+} or K4 in intact (*n* = 3), castrated (*n* = 4) and
1251 regenerated (*n* = 5) mice. (**F**) Co-immunostaining showing the enrichment of K4^{+} RFP labelled

1252 cells in the proximal region of the AP (top) and DLVP (bottom) prostate lobes. Scale bar: 50 µm.

1253 Source files are available in Figure 4—figure supplement 1—source data 1.

1254

1255 **Figure 5—figure supplement 1. Characterization of RUNX1 expression during prostate**

1256 **development *in vivo*.**

1257 (**A**) Co-immunostainings of the mouse urogenital sinus at E18.5 for RUNX1, NKX3.1, K4. p:

1258 proximal, d: distal. Scale bar: 50 µm. Dotted lines indicate the urogenital epithelium. (**B**) Co-

1259 immunostainings of the mouse urogenital sinus at E18.5 for RUNX1, NKX3.1, LY6D. p: proximal,

1260 d: distal. Scale bar: 50 µm. (**C**) Co-immunostaining of RUNX1, NKX3.1, K4 at postnatal (P) day 14.

1261 Higher magnification images of (p) proximal, (i) intermediate, and (d) distal regions are shown.

1262 Scale bars: 200 µm (yellow) and 50 µm (white). (**D**, **E**) Co-immunostainings at P14 for RUNX1,

1263 K5, K8 in **B** RUNX1, p63, CDH1 in **C**. p: proximal, i: intermediate, d: distal. Scale bar: 50 µm.

1264

1265 **Figure 5—figure supplement 2. Characterization of RUNX1 expression during prostate**

1266 **development in UGS explant cultures.**

1267 (**A**) Co-immunostaining of RUNX1, K5, K8 in UGS explants harvested at day 2 and day 7. p:

1268 proximal, d: distal. Scale bar: 50 µm. (**E**) Quantification of the percentage of $K5^+$, $K8^+$, $K5^+$ $K8^+$

1269 cells during UGS explant cultures at day 0 (*n* = 2 explants), day 1 (*n* = 3 explants), day 2 (*n* = 3

1270 explants), day 7 (*n* = 4 explants), showing a progressive reduction in the proportion of $K5^+$ $K8^+$

1271 double positive cells. (**C**) Co-immunostaining of RUNX1, NKX3.1, LY6D in UGS explants harvested

1272 at day 7. p: proximal, d: distal. Scale bar: 50 µm. (**D**) Co-immunostaining of RUNX1, NKX3.1, K4

1273 in UGS explants harvested at day 1 (top), 3 (middle) and 7 (bottom). Higher magnification

1274 images of (p) proximal, (i) intermediate, and (d) distal regions are shown for day 7. Scale bars:
1275 200 µm (yellow) and 50 µm (white). Dotted lines indicate the urogenital epithelium. (**E**) Co-
1276 immunostaining of RUNX1, Ki67, CDH1 in UGS explants harvested at day 2 and day 7. p:
1277 proximal, d: distal. Scale bar: 50 µm. Source files are available in Figure 5—figure supplement
1278 2—source data 1.
1279
1280 **Figure 6—figure supplement 1. Pre-processing of the scRNA-seq dataset of UGS explant**
1281 **cultures.**
1282 (**A**) UMAP visualization in MULTI-seq barcodes space before (top) and after (bottom) quality
1283 control and barcode filtration (see Methods for details). (**B**) UMAP visualization of the dataset
1284 colored by estimated cell cycle phase (top). Due to the strong underlying impact on clustering,
1285 the cell cycle effect was regressed out (bottom). (**C, D**) UMAP visualization of the dataset
1286 colored in **C** by experimental time point and in **D** by labeled populations. (**E**) Dot plot showing
1287 the expression of selected marker genes associated with each labelled population. (**F**) Bar plots
1288 of the 10 most significantly (g:Profiler adjusted p-value < 0.05) enriched gene ontology (GO)
1289 terms (GO:BP, Biological Processes) on the differentially upregulated genes specific to the
1290 'Hypoxic/Stressed' cluster. (**G**-**I**) UMAP visualization of the prostatic subset (from **D**), labelled by
1291 time points in **G**, clusters in **H**, estimated cell cycle phase in **I**. (**J**) Percentage of cells in the
1292 different estimated cell cycle phases in each clusters. (**K**) Diffusion maps representation of the
1293 prostatic subset using the first 2 diffusion components with (top) and without C9 (bottom). C9
1294 was excluded for downstream analyses due to its outlying profile.
1295

1296 **Figure 6—figure supplement 2. Characterization of the developing prostatic epithelium in the**

1297 **scRNA-seq dataset of UGS explant culture.**

1298 (**A**) Heatmap of the 10 most differentially upregulated genes per cluster. (**B**-**E**) PAGA

1299 representations with cluster nodes colored by a gradient representing the mean log-normalized

1300 expression levels of each genes indicated. (**B**) shows the expression of common prostate

1301 lineage markers, (**C**) shows known regulators of prostate development, (**D**) shows basal

1302 markers, (**E**) shows proliferation markers. (**F**) Box plots of per-cell AUC signature scores

1303 calculated using the 'AUCell' package for individual UGS explant clusters. Gene signatures were

1304 generated using the list of differentially upregulated genes previously obtained from our adult

1305 mouse prostate clusters. (**G**) Force directed visualization of the developing prostatic epithelium

1306 in UGS explant cultures. Color gradient represents AUC scores per cell.

1307

1308 **Figure 7—figure supplement 1. Lineage-tracing of RUNX1 expressing cells in UGS explants.**

1309 (**A, B**) Co-immunostaining of RFP, p63, CDH1 in UGS explants harvested at day 2 (**A**) and day 7

1310 (**B**). Higher magnification images of (i) proximal and (ii) distal regions are shown for day 7.

1311 Arrows show RFP^+ $p63^+$ cells, arrowheads show RFP^+ $p63^-$ cells. Scale bars: 200 µm (yellow) and

1312 50 µm (white). (**C**) Quantification of the percentage of epithelial RFP^+ $p63^+$ cells at day 2 (n = 7)

1313 and day 7 (n = 4) of UGS explant cultures. Quantification was performed within the boundaries

1314 delimited in **B** by dotted lines. (**D**) Co-immunostaining of RFP, K5, K8 in UGS explants harvested

1315 at day 2 (top) and day 7 (bottom). Higher magnification images of proximal (i) and (ii) distal

1316 regions are shown for day 7. Arrows show RFP^+ $K5^+$ $K8^+$ cells, chevron arrows show RFP^+ $K5^-$ $K8^+$,

1317 arrowheads show RFP^+ $K5^+$ $K8^-$ cells. Scale bars: 200 µm (yellow) and 50 µm (white).

1318 (**E**) Quantification of the percentage of epithelial $K5^+$ $K8^+$, $K5^-$ $K8^+$ cells and $K5^+$ $K8^-$ cells in the

1319 RFP subset at day 2 (*n* = 4) and day 7 (*n* = 3) of UGS explant cultures. Quantifications were

1320 performed within the boundaries delimited in **D** by dotted lines. (**F, G**) Co-immunostaining of

1321 RFP, *Nupr1* (mRNA), CDH1 in UGS explants harvested at day 2 (**F**) and day 7 (**G**). Higher

1322 magnification images of (i) proximal and (ii) distal regions are shown for day 7. Arrows show

1323 RFP^+ *Nupr1*$^+$ cells, arrowheads show RFP^+ *Nupr1*$^-$ cells. Scale bars: 200 µm (yellow) and 50 µm

1324 (white). **(J)** Quantification of the percentage of epithelial $K4^+$ cells in the RFP subset at day 2 (*n* =

1325 3) and day 7 (*n* = 4) of UGS explant cultures. Quantification was performed within the

1326 boundaries delimited in **G** by dotted lines. Source files are available in Figure 7—figure

1327 supplement 1—source data 1.

1328 **FIGURE SUPPLEMENTS**

1329 **Figure 1—figure supplement 1. RUNX1 is enriched in the mouse prostate epithelium.**

1330 **Figure 1—figure supplement 2. *Runx1* expression is mediated by the P2 promoter in the**

1331 **mouse prostate epithelium.**

1332 **Figure 1—figure supplement 3. Characterization of P2-*Runx1*:RFP derived mouse prostate**

1333 **organoids.**

1334 **Figure 2—figure supplement 1. Characterization of RUNX1 expression in the castrated mouse**

1335 **prostate.**

1336 **Figure 3—figure supplement 1. Pre-processing of the scRNA-seq dataset of adult intact and**

1337 **castrated mouse prostates.**

1338 **Figure 3—figure supplement 2. Characterization of the scRNA-seq prostate epithelial subset.**

1339 **Figure 3—figure supplement 3. Characterization of the scRNA-seq prostate epithelial dataset.**

1340 **Figure 3—figure supplement 4. Gene Ontology and differential expression analysis within the**

1341 **scRNA-seq prostate epithelial dataset.**

1342 **Figure 4—figure supplement 1. Lineage tracing of RUNX1 expressing cells labelled in intact**

1343 **mice.**

1344 **Figure 5—figure supplement 1. Characterization of RUNX1 expression during prostate**

1345 **development *in vivo*.**

1346 **Figure 5—figure supplement 2. Characterization of RUNX1 expression during prostate**

1347 **development in UGS explant cultures.**

1348 **Figure 6—figure supplement 1. Pre-processing of the scRNA-seq dataset of UGS explant**

1349 **cultures.**

1350 **Figure 6—figure supplement 2. Characterization of the developing prostatic epithelium in the**

1351 **scRNA-seq dataset of UGS explant culture.**

1352 **Figure 7—figure supplement 1. Lineage-tracing of RUNX1 expressing cells in UGS explants.**

1353 ## SUPPLEMENTARY FILES

1354 **Supplementary file 1. Quality control metrics and metadata of scRNAseq experiments**

1355 **Supplementary file 2. Genes differentially expressed between adult clusters**

1356 **Supplementary file 3. Genes differentially expressed in intact versus castrated Lum-D cells**

1357 **Supplementary file 4. Genes differentially expressed between UGS explants clusters**

1358 **Supplementary file 5. Gene lists used for the analysis of gene set activity**

1359

1360 ## SOURCE DATA FILES

1361 **Figure 1. source data 1.xlsx**

1362 **Figure 1. figure supplement 1. source data1 .xlsx**

1363 **Figure 1. figure supplement 2. source data1 .xlsx**

1364 **Figure 1. figure supplement 3. source data 1.xlsx**

1365 **Figure 2. figure supplement 1. source data 1.xlsx**

1366 **Figure 2. source data 1.xlsx**

1367 **Figure 4. source data 1.xlsx**

1368 **Figure 4. figure supplement 1. source data 1.xlsx**

1369 **Figure 5. figure supplement 2. source data 1.xlsx**

1370 **Figure 5. source data 1.xlsx**

1371 **Figure 7 - figure supplement 1. source data 1.xlsx**

1372 **Figure 7 - source data 1.xlsx**

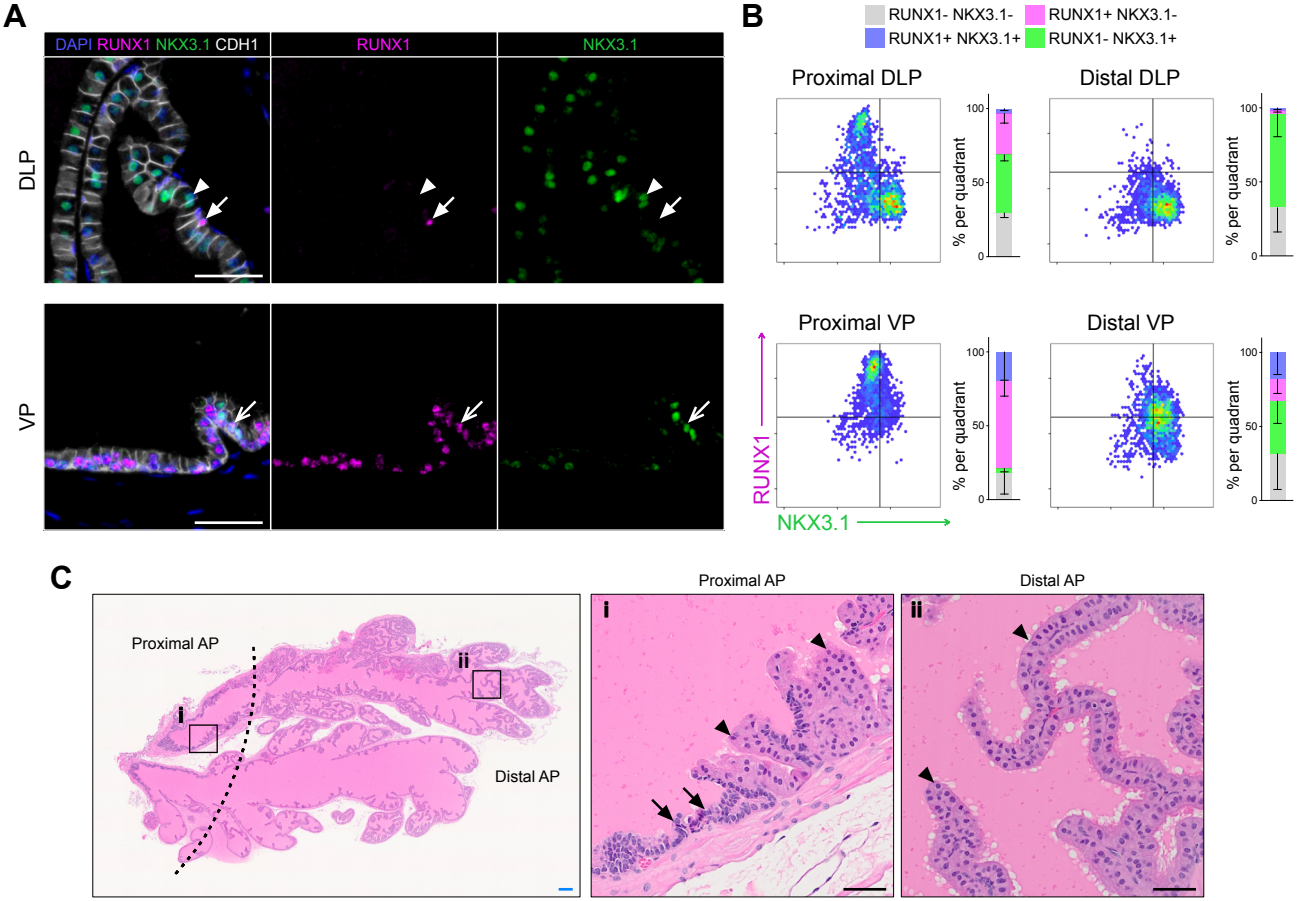
A
DAPI RUNX1 NKX3.1 CDH1
RUNX1
NKX3.1
DLP
VP
B
RUNX1- NKX3.1-
RUNX1+ NKX3.1-
RUNX1+ NKX3.1+
RUNX1- NKX3.1+
Proximal DLP
Distal DLP
Proximal VP
Distal VP
% per quadrant
100
50
0
RUNX1
NKX3.1
C
Proximal AP
Distal AP
i
ii

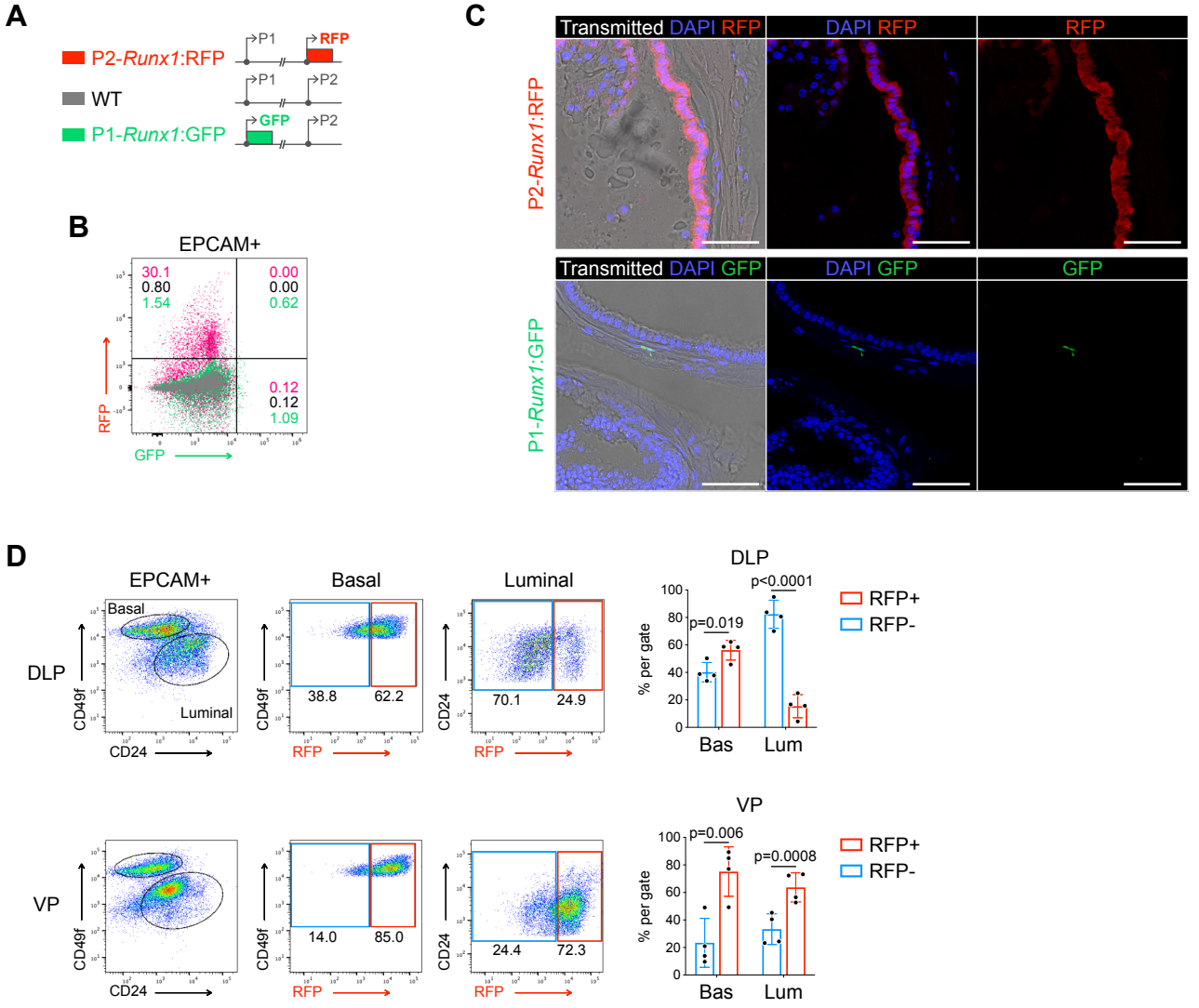
A
P2-Runx1:RFP
WT
P1-Runx1:GFP
P1
RFP
P2
GFP
B
EPCAM+
30.1
0.80
1.54
0.00
0.00
0.62
0.12
0.12
1.09
RFP
GFP
C
Transmitted DAPI RFP
DAPI RFP
RFP
P2-Runx1:RFP
Transmitted DAPI GFP
DAPI GFP
GFP
P1-Runx1:GFP
D
EPCAM+
Basal
Luminal
DLP
CD49f
CD24
38.8
62.2
70.1
24.9
RFP
VP
14.0
85.0
24.4
72.3
% per gate
p=0.019
p<0.0001
p=0.006
p=0.0008
Bas
Lum
RFP+
RFP-

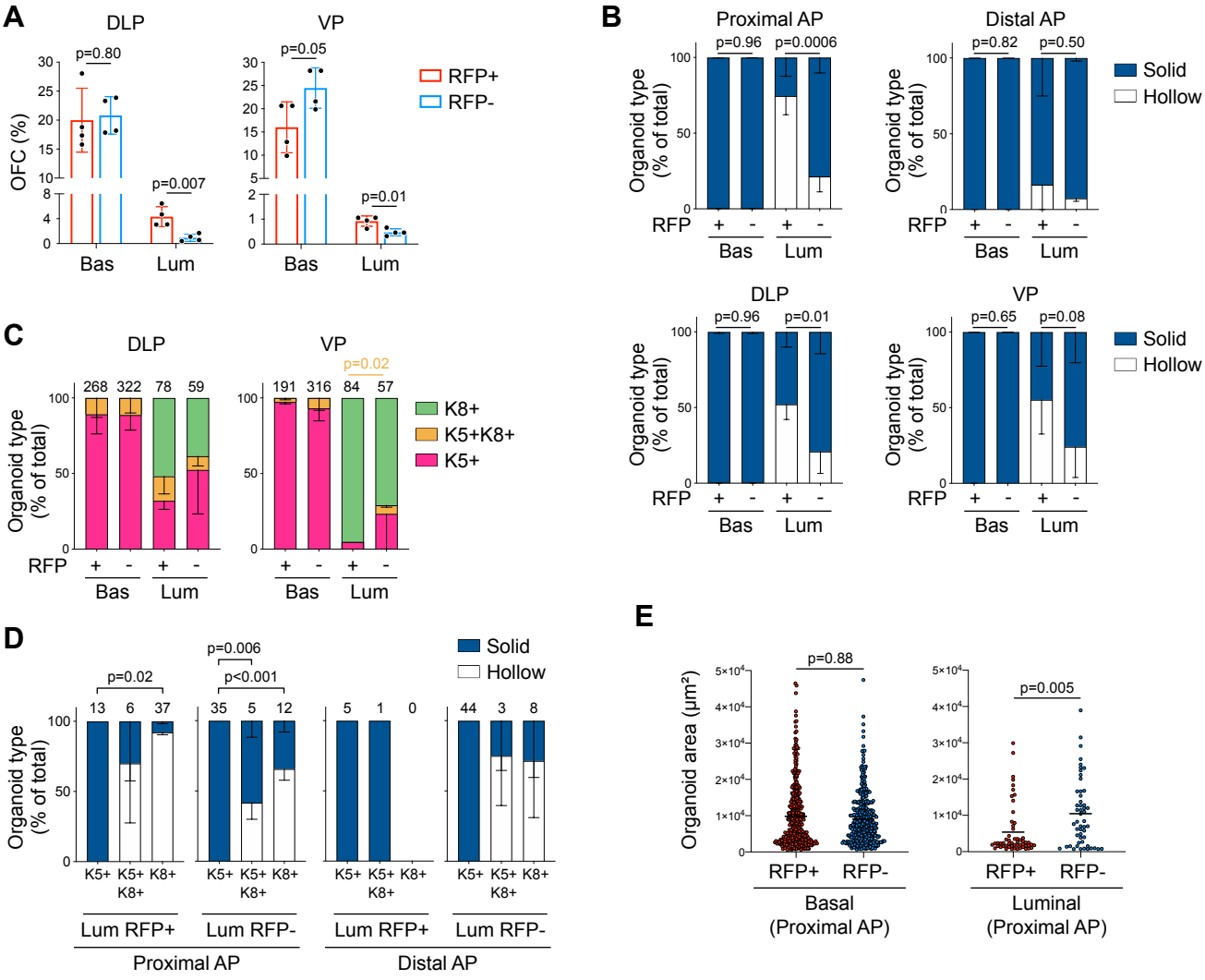
A
DLP
VP
OFC (%)
p=0.80
p=0.007
p=0.05
p=0.01
RFP+
RFP-
Bas
Lum
B
Proximal AP
Distal AP
DLP
VP
Organoid type (% of total)
p=0.96
p=0.0006
p=0.82
p=0.50
p=0.96
p=0.01
p=0.65
p=0.08
Solid
Hollow
RFP
C
268 322 78 59
191 316 84 57
p=0.02
K8+
K5+K8+
K5+
D
p=0.02
p=0.006
p<0.001
13 6 37
35 5 12
5 1 0
44 3 8
K5+ K5+ K8+
Lum RFP+
Lum RFP-
Proximal AP
Distal AP
E
Organoid area (µm²)
p=0.88
p=0.005
Basal (Proximal AP)
Luminal (Proximal AP)

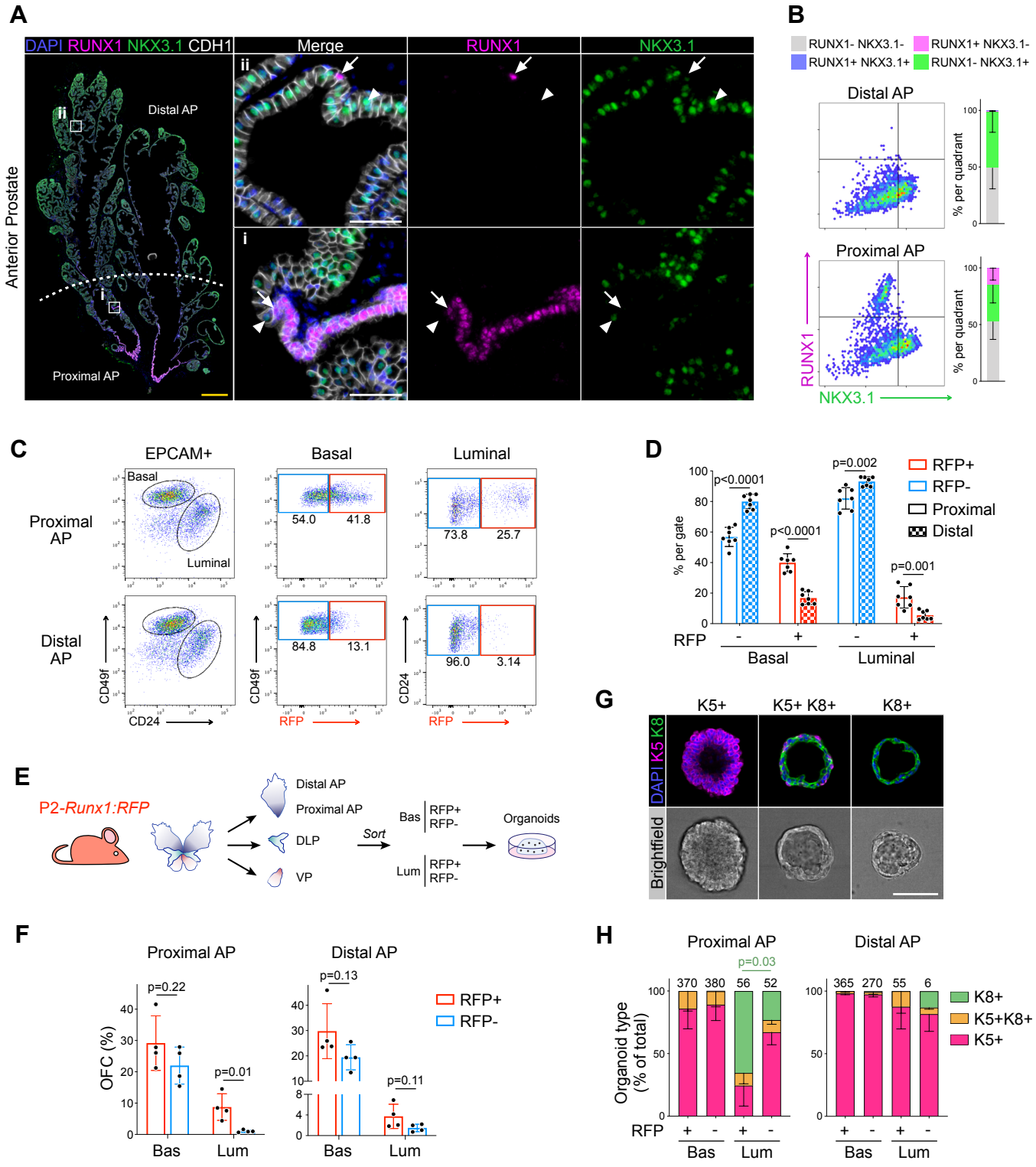
A
DAPI RUNX1 NKX3.1 CDH1
Merge
RUNX1
NKX3.1
Anterior Prostate
Distal AP
Proximal AP
ii
i
B
RUNX1- NKX3.1-
RUNX1+ NKX3.1-
RUNX1+ NKX3.1+
RUNX1- NKX3.1+
Distal AP
Proximal AP
% per quadrant
RUNX1
NKX3.1
C
EPCAM+
Basal
Luminal
Proximal AP
Distal AP
54.0
41.8
73.8
25.7
84.8
13.1
96.0
3.14
CD49f
CD24
RFP
D
% per gate
p<0.0001
p<0.0001
p=0.002
p=0.001
RFP+
RFP-
Proximal
Distal
RFP
Basal
Luminal
E
P2-Runx1:RFP
Distal AP
Proximal AP
DLP
VP
Sort
Bas
Lum
RFP+
RFP-
Organoids
F
Proximal AP
Distal AP
OFC (%)
p=0.22
p=0.01
p=0.13
p=0.11
RFP+
RFP-
Bas
Lum
G
K5+
K5+ K8+
K8+
DAPI K5 K8
Brightfield
H
Proximal AP
Distal AP
p=0.03
370
380
56
52
365
270
55
6
Organoid type (% of total)
K8+
K5+K8+
K5+
RFP
Bas
Lum

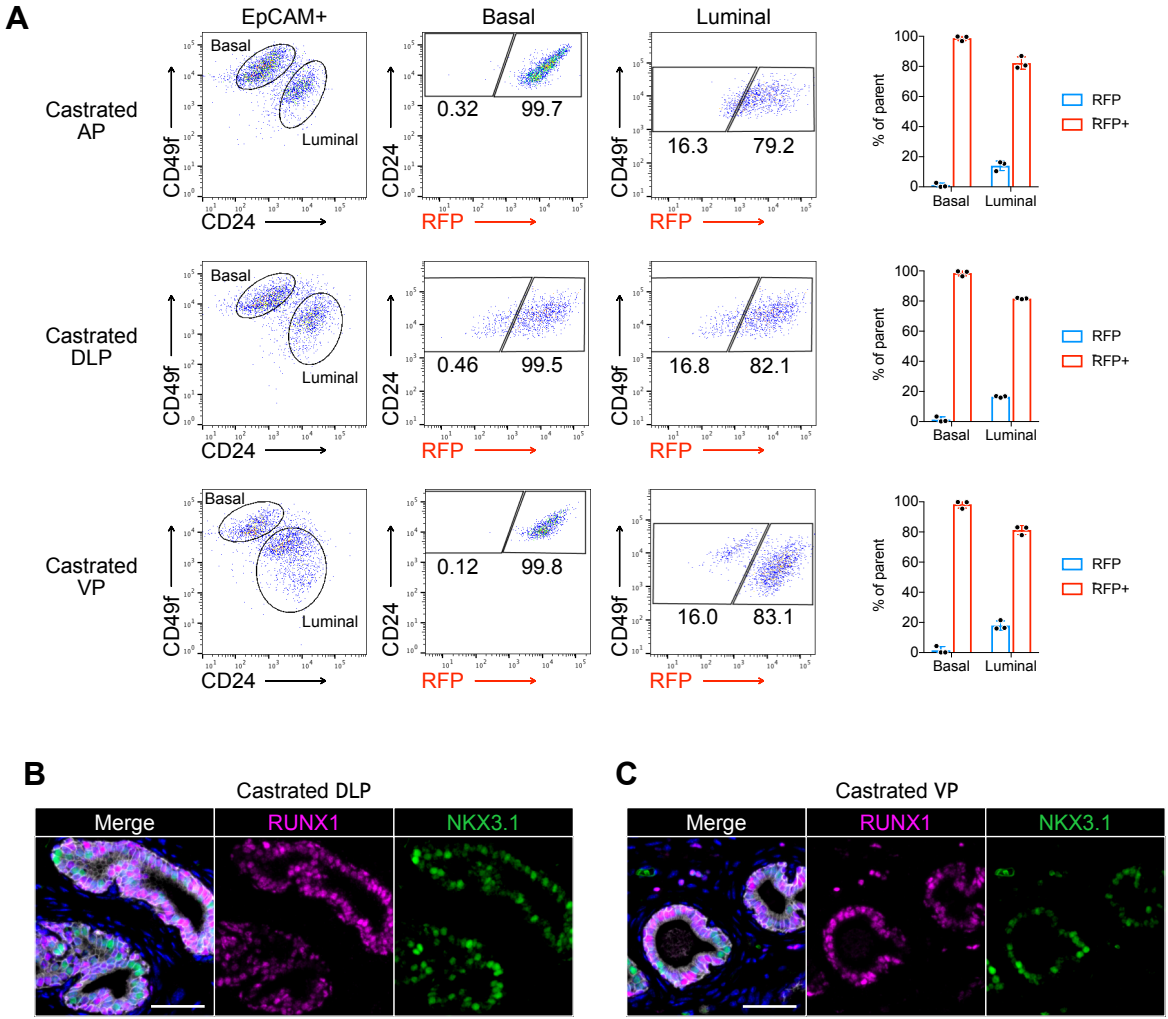
A
EpCAM+
Basal
Luminal
Castrated AP
Castrated DLP
Castrated VP
CD49f
CD24
RFP
0.32
99.7
16.3
79.2
0.46
99.5
16.8
82.1
0.12
99.8
16.0
83.1
% of parent
RFP
RFP+
B
Castrated DLP
Merge
RUNX1
NKX3.1
C
Castrated VP

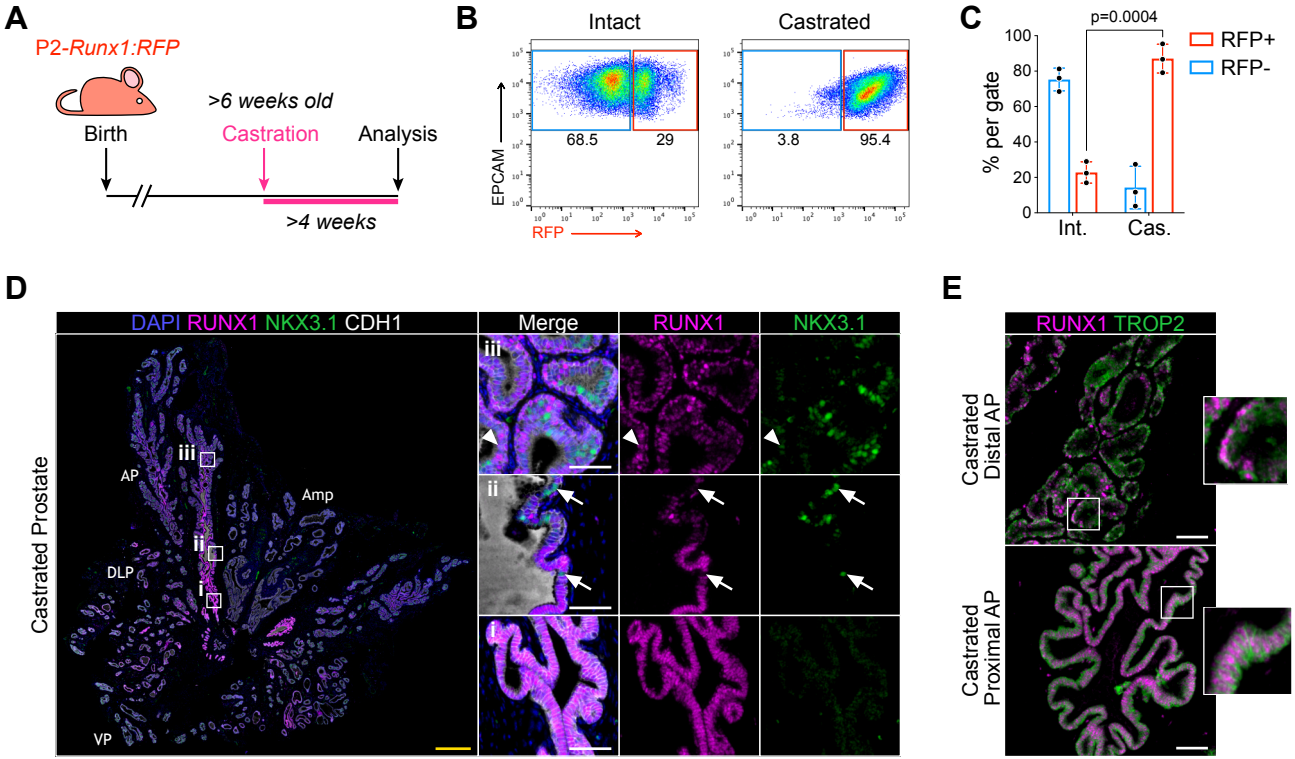
A
P2-Runx1:RFP
>6 weeks old
Birth
Castration
Analysis
>4 weeks
B
Intact
Castrated
EPCAM
RFP
68.5
29
3.8
95.4
C
p=0.0004
RFP+
RFP-
% per gate
Int.
Cas.
D
DAPI RUNX1 NKX3.1 CDH1
Merge
RUNX1
NKX3.1
Castrated Prostate
AP
DLP
VP
Amp
iii
ii
i
E
RUNX1 TROP2
Castrated Distal AP
Castrated Proximal AP

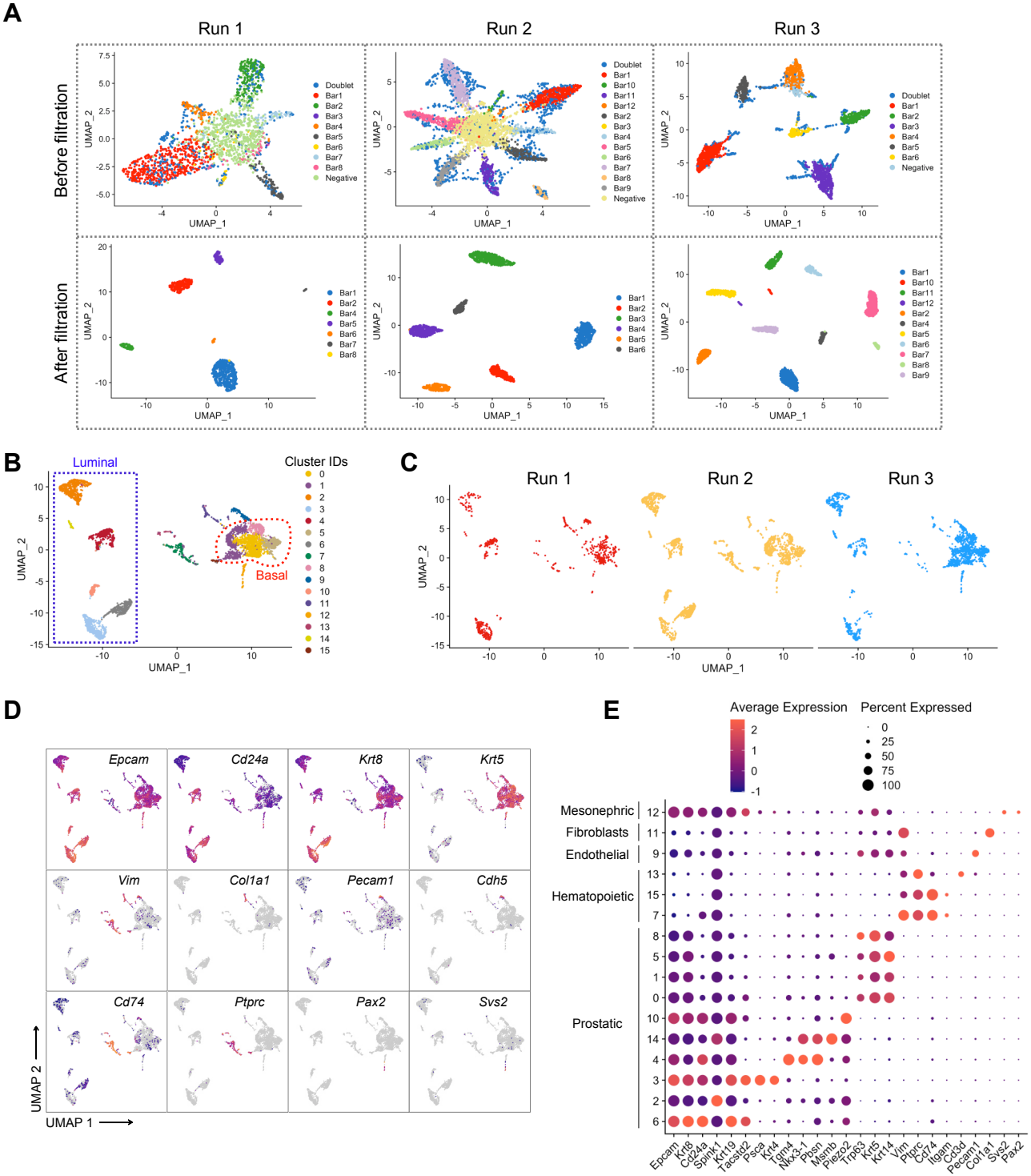
A
Run 1
Run 2
Run 3
Before filtration
After filtration
UMAP_1
UMAP_2
Doublet
Bar1
Bar2
Bar3
Bar4
Bar5
Bar6
Bar7
Bar8
Bar9
Bar10
Bar11
Bar12
Negative
B
Luminal
Basal
Cluster IDs
C
D
Epcam
Cd24a
Krt8
Krt5
Vim
Col1a1
Pecam1
Cdh5
Cd74
Ptprc
Pax2
Svs2
UMAP 2
UMAP 1
E
Average Expression
Percent Expressed
Mesonephric
Fibroblasts
Endothelial
Hematopoietic
Prostatic
Epcam
Krt8
Cd24a
Spink1
Krt19
Tacstd2
Psca
Krt4
Tgm4
Nkx3.1
Ppsn
Msmb
Piezo2
Trp63
Krt5
Krt14
Vim
Ptprc
Cd74
Itgam
Cd3d
Pecam1
Col1a1
Svs2
Pax2

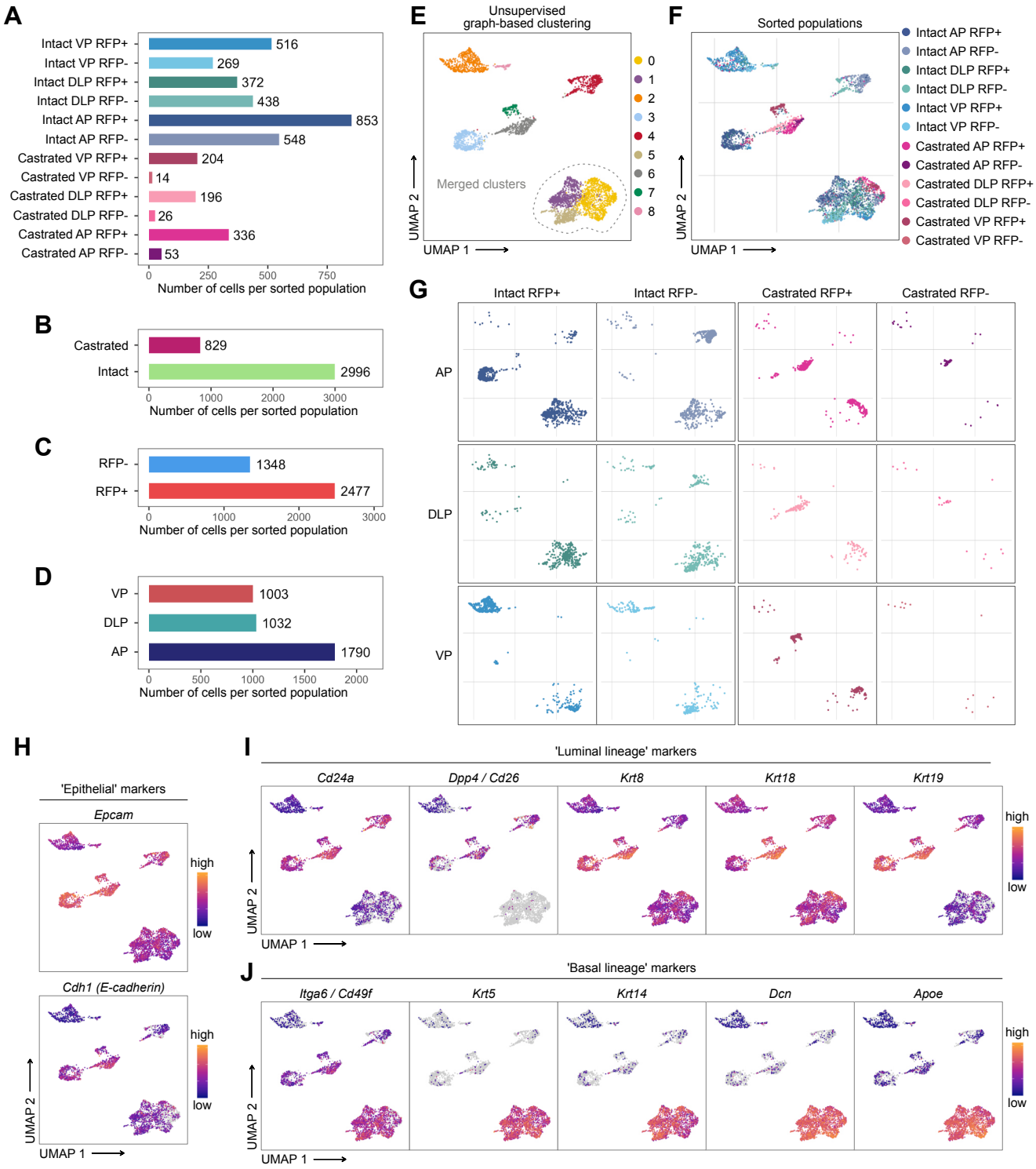
A
Intact VP RFP+ 516
Intact VP RFP- 269
Intact DLP RFP+ 372
Intact DLP RFP- 438
Intact AP RFP+ 853
Intact AP RFP- 548
Castrated VP RFP+ 204
Castrated VP RFP- 14
Castrated DLP RFP+ 196
Castrated DLP RFP- 26
Castrated AP RFP+ 336
Castrated AP RFP- 53
0 250 500 750
Number of cells per sorted population
B
Castrated 829
Intact 2996
0 1000 2000 3000
Number of cells per sorted population
C
RFP- 1348
RFP+ 2477
0 1000 2000 3000
Number of cells per sorted population
D
VP 1003
DLP 1032
AP 1790
0 500 1000 1500 2000
Number of cells per sorted population
E
Unsupervised graph-based clustering
Merged clusters
0 1 2 3 4 5 6 7 8
UMAP 2
UMAP 1
F
Sorted populations
Intact AP RFP+
Intact AP RFP-
Intact DLP RFP+
Intact DLP RFP-
Intact VP RFP+
Intact VP RFP-
Castrated AP RFP+
Castrated AP RFP-
Castrated DLP RFP+
Castrated DLP RFP-
Castrated VP RFP+
Castrated VP RFP-
UMAP 2
UMAP 1
G
Intact RFP+
Intact RFP-
Castrated RFP+
Castrated RFP-
AP
DLP
VP
H
'Epithelial' markers
Epcam
Cdh1 (E-cadherin)
high
low
UMAP 2
UMAP 1
I
'Luminal lineage' markers
Cd24a
Dpp4 / Cd26
Krt8
Krt18
Krt19
high
low
UMAP 2
UMAP 1
J
'Basal lineage' markers
Itga6 / Cd49f
Krt5
Krt14
Dcn
Apoe
high
low
UMAP 2
UMAP 1

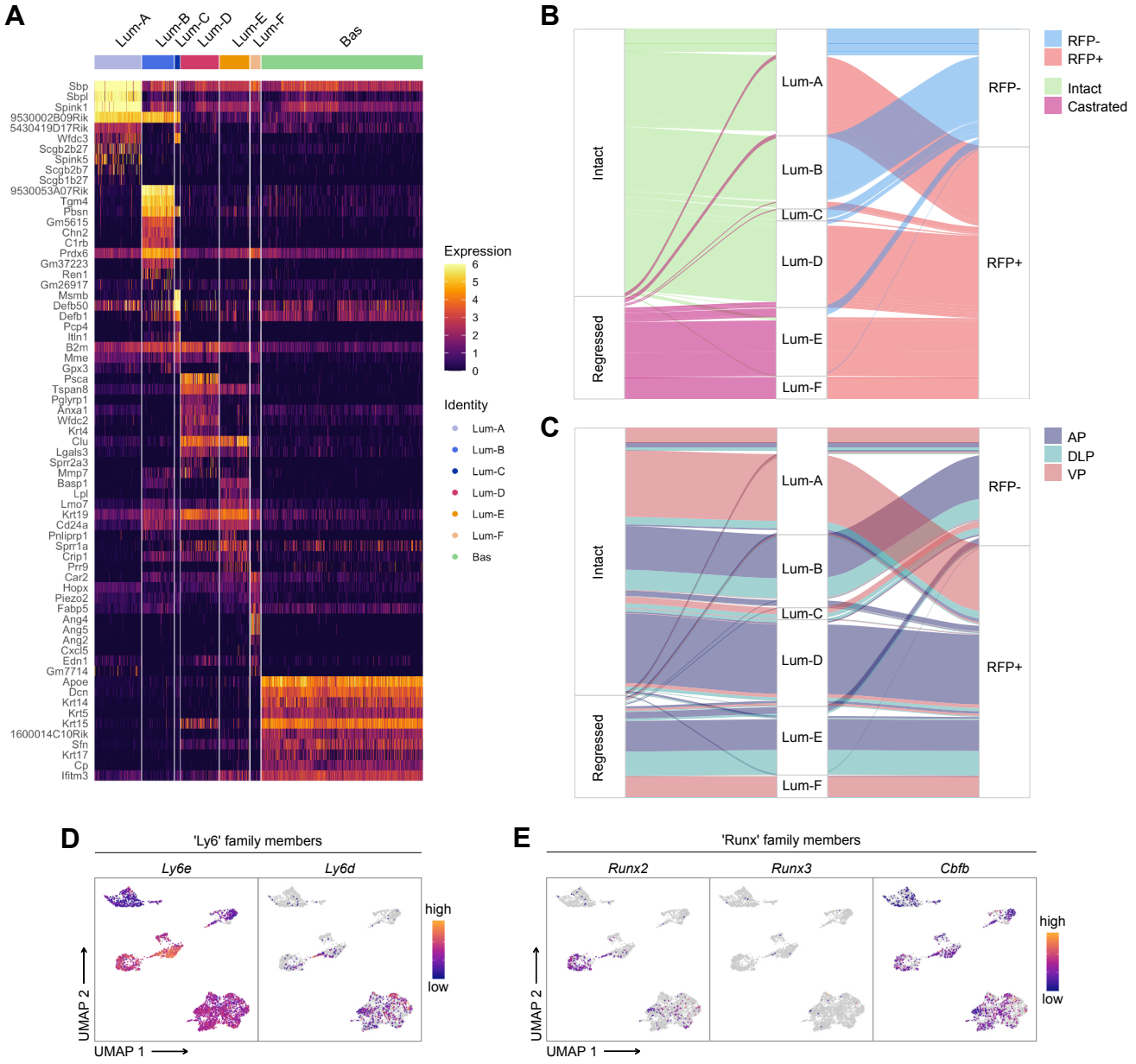
A
Lum-A
Lum-B
Lum-C
Lum-D
Lum-E
Lum-F
Bas
Sbp
Sbpl
Spink1
9530002B09Rik
5430419D17Rik
Wfdc3
Scgb2b27
Spink5
Scgb2b7
Scgb1b27
9530053A07Rik
Tgm4
Pbsn
Gm5615
Chn2
C1rb
Prdx6
Gm37223
Ren1
Gm26917
Msmb
Defb50
Defb1
Pcp4
Ttn1
B2m
Mme
Gpx3
Psca
Tspan8
Pglyrp1
Anxa1
Wfdc2
Krt4
Clu
Lgals3
Sprr2a3
Mmp7
Basp1
Lpl
Lmo7
Krt19
Cd24a
Pnliprp1
Sprr1a
Crip1
Prr9
Car2
Hopx
Piezo2
Fabp5
Ang4
Ang5
Ang2
Cxcl5
Edn1
Gm7714
Apoe
Dcn
Krt14
Krt5
Krt15
1600014C10Rik
Sfn
Krt17
Cp
Ifitm3
Expression
6
5
4
3
2
1
0
Identity
Lum-A
Lum-B
Lum-C
Lum-D
Lum-E
Lum-F
Bas
B
Intact
Regressed
Lum-A
Lum-B
Lum-C
Lum-D
Lum-E
Lum-F
RFP-
RFP+
RFP-
RFP+
Intact
Castrated
C
Intact
Regressed
Lum-A
Lum-B
Lum-C
Lum-D
Lum-E
Lum-F
RFP-
RFP+
AP
DLP
VP
D
'Ly6' family members
Ly6e
Ly6d
high
low
UMAP 2
UMAP 1
E
'Runx' family members
Runx2
Runx3
Cbfb
high
low
UMAP 2
UMAP 1

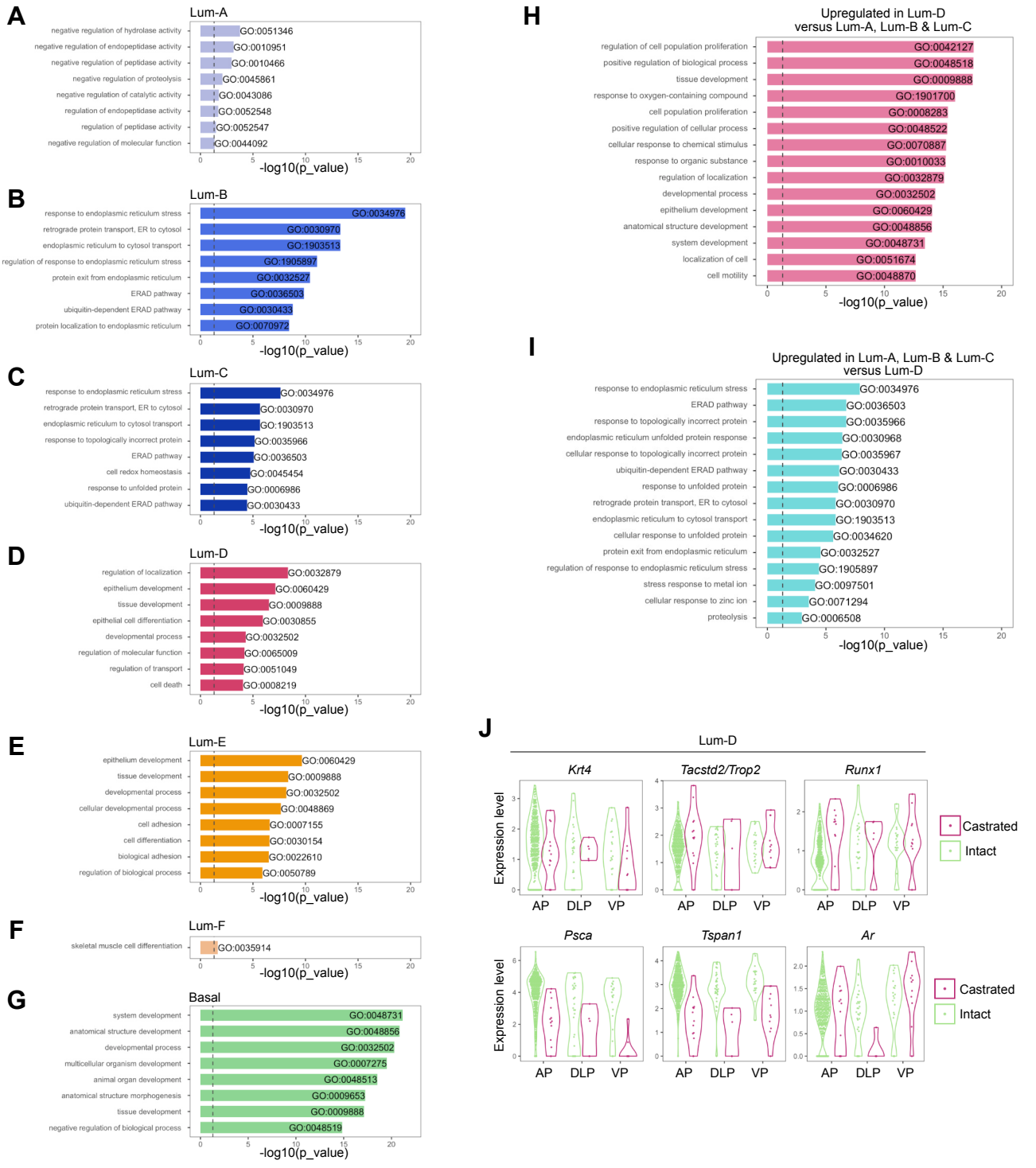
A
Lum-A
negative regulation of hydrolase activity
GO:0051346
negative regulation of endopeptidase activity
GO:0010951
negative regulation of peptidase activity
GO:0010466
negative regulation of proteolysis
GO:0045861
negative regulation of catalytic activity
GO:0043086
regulation of endopeptidase activity
GO:0052548
regulation of peptidase activity
GO:0052547
negative regulation of molecular function
GO:0044092
-log10(p_value)
B
Lum-B
response to endoplasmic reticulum stress
GO:0034976
retrograde protein transport, ER to cytosol
GO:0030970
endoplasmic reticulum to cytosol transport
GO:1903513
regulation of response to endoplasmic reticulum stress
GO:1905897
protein exit from endoplasmic reticulum
GO:0032527
ERAD pathway
GO:0036503
ubiquitin-dependent ERAD pathway
GO:0030433
protein localization to endoplasmic reticulum
GO:0070972
-log10(p_value)
C
Lum-C
response to endoplasmic reticulum stress
GO:0034976
retrograde protein transport, ER to cytosol
GO:0030970
endoplasmic reticulum to cytosol transport
GO:1903513
response to topologically incorrect protein
GO:0035966
ERAD pathway
GO:0036503
cell redox homeostasis
GO:0045454
response to unfolded protein
GO:0006986
ubiquitin-dependent ERAD pathway
GO:0030433
-log10(p_value)
D
Lum-D
regulation of localization
GO:0032879
epithelium development
GO:0060429
tissue development
GO:0009888
epithelial cell differentiation
GO:0030855
developmental process
GO:0032502
regulation of molecular function
GO:0065009
regulation of transport
GO:0051049
cell death
GO:0008219
-log10(p_value)
E
Lum-E
epithelium development
GO:0060429
tissue development
GO:0009888
developmental process
GO:0032502
cellular developmental process
GO:0048869
cell adhesion
GO:0007155
cell differentiation
GO:0030154
biological adhesion
GO:0022610
regulation of biological process
GO:0050789
-log10(p_value)
F
Lum-F
skeletal muscle cell differentiation
GO:0035914
-log10(p_value)
G
Basal
system development
GO:0048731
anatomical structure development
GO:0048856
developmental process
GO:0032502
multicellular organism development
GO:0007275
animal organ development
GO:0048513
anatomical structure morphogenesis
GO:0009653
tissue development
GO:0009888
negative regulation of biological process
GO:0048519
-log10(p_value)
H
Upregulated in Lum-D
versus Lum-A, Lum-B & Lum-C
regulation of cell population proliferation
GO:0042127
positive regulation of biological process
GO:0048518
tissue development
GO:0009888
response to oxygen-containing compound
GO:1901700
cell population proliferation
GO:0008283
positive regulation of cellular process
GO:0048522
cellular response to chemical stimulus
GO:0070887
response to organic substance
GO:0010033
regulation of localization
GO:0032879
developmental process
GO:0032502
epithelium development
GO:0060429
anatomical structure development
GO:0048856
system development
GO:0048731
localization of cell
GO:0051674
cell motility
GO:0048870
-log10(p_value)
I
Upregulated in Lum-A, Lum-B & Lum-C
versus Lum-D
response to endoplasmic reticulum stress
GO:0034976
ERAD pathway
GO:0036503
response to topologically incorrect protein
GO:0035966
endoplasmic reticulum unfolded protein response
GO:0030968
cellular response to topologically incorrect protein
GO:0035967
ubiquitin-dependent ERAD pathway
GO:0030433
response to unfolded protein
GO:0006986
retrograde protein transport, ER to cytosol
GO:0030970
endoplasmic reticulum to cytosol transport
GO:1903513
cellular response to unfolded protein
GO:0034620
protein exit from endoplasmic reticulum
GO:0032527
regulation of response to endoplasmic reticulum stress
GO:1905897
stress response to metal ion
GO:0097501
cellular response to zinc ion
GO:0071294
proteolysis
GO:0006508
-log10(p_value)
J
Lum-D
Krt4
Tacstd2/Trop2
Runx1
Psca
Tspan1
Ar
Expression level
AP
DLP
VP
Castrated
Intact

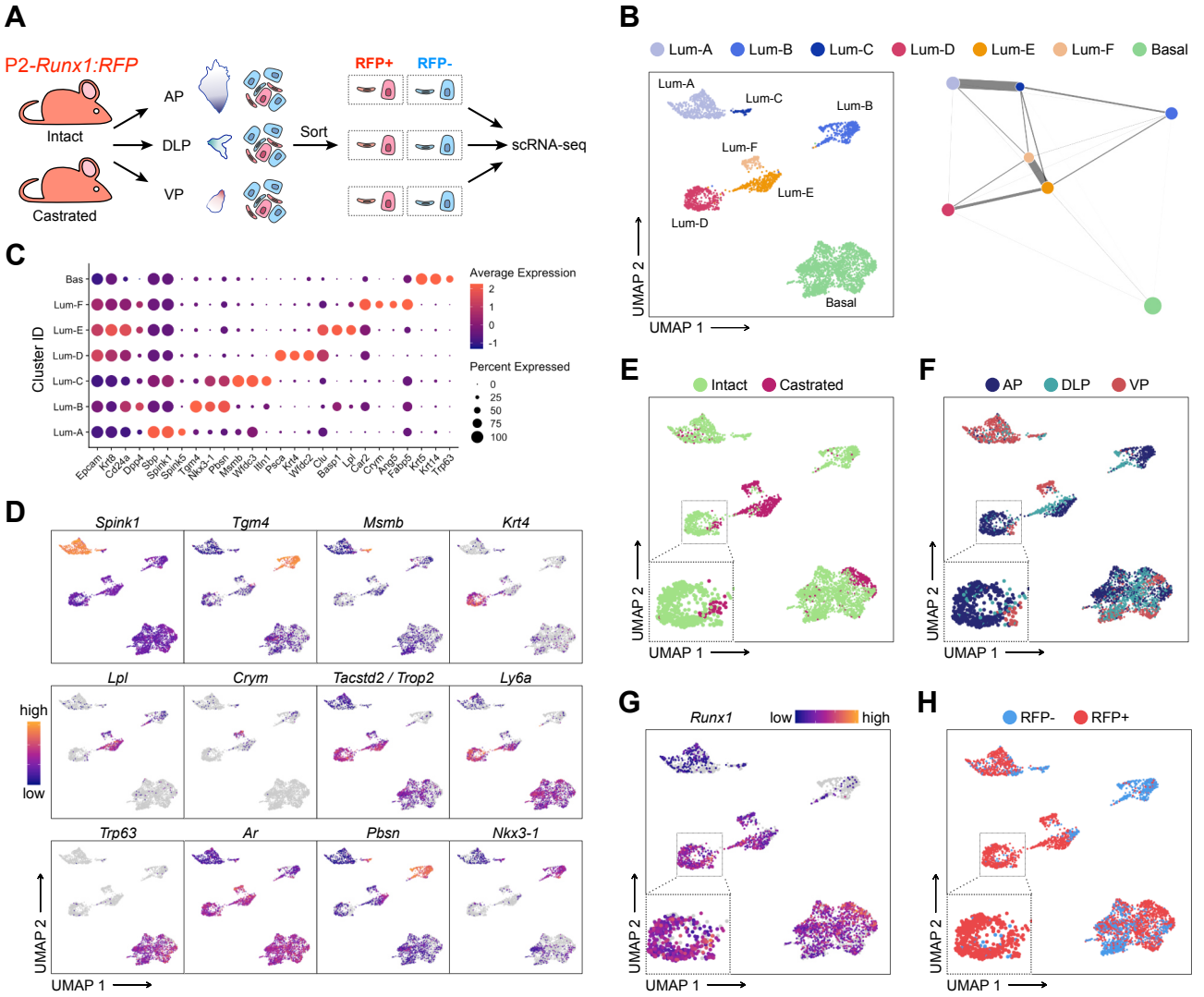
A
P2-Runx1:RFP
Intact
Castrated
AP
DLP
VP
Sort
RFP+
RFP-
scRNA-seq
B
Lum-A
Lum-B
Lum-C
Lum-D
Lum-E
Lum-F
Basal
UMAP 1
UMAP 2
C
Cluster ID
Bas
Lum-F
Lum-E
Lum-D
Lum-C
Lum-B
Lum-A
Epcam
Krt8
Cd24a
Dpp4
Sbp
Spink1
Spink5
Tgm4
Nkx3-1
Pbsn
Msmb
Wfdc3
Ibin1
Psca
Krt4
Wfdc2
Clu
Basp1
Lpl
Car2
Crym
Angp2
Fabp5
Krt5
Krt14
Trp63
Average Expression
2
1
0
-1
Percent Expressed
0
25
50
75
100
D
Spink1
Tgm4
Msmb
Krt4
Lpl
Crym
Tacstd2 / Trop2
Ly6a
Trp63
Ar
Pbsn
Nkx3-1
high
low
UMAP 2
UMAP 1
E
Intact
Castrated
UMAP 2
UMAP 1
F
AP
DLP
VP
UMAP 2
UMAP 1
G
Runx1
low
high
UMAP 2
UMAP 1
H
RFP-
RFP+
UMAP 2
UMAP 1

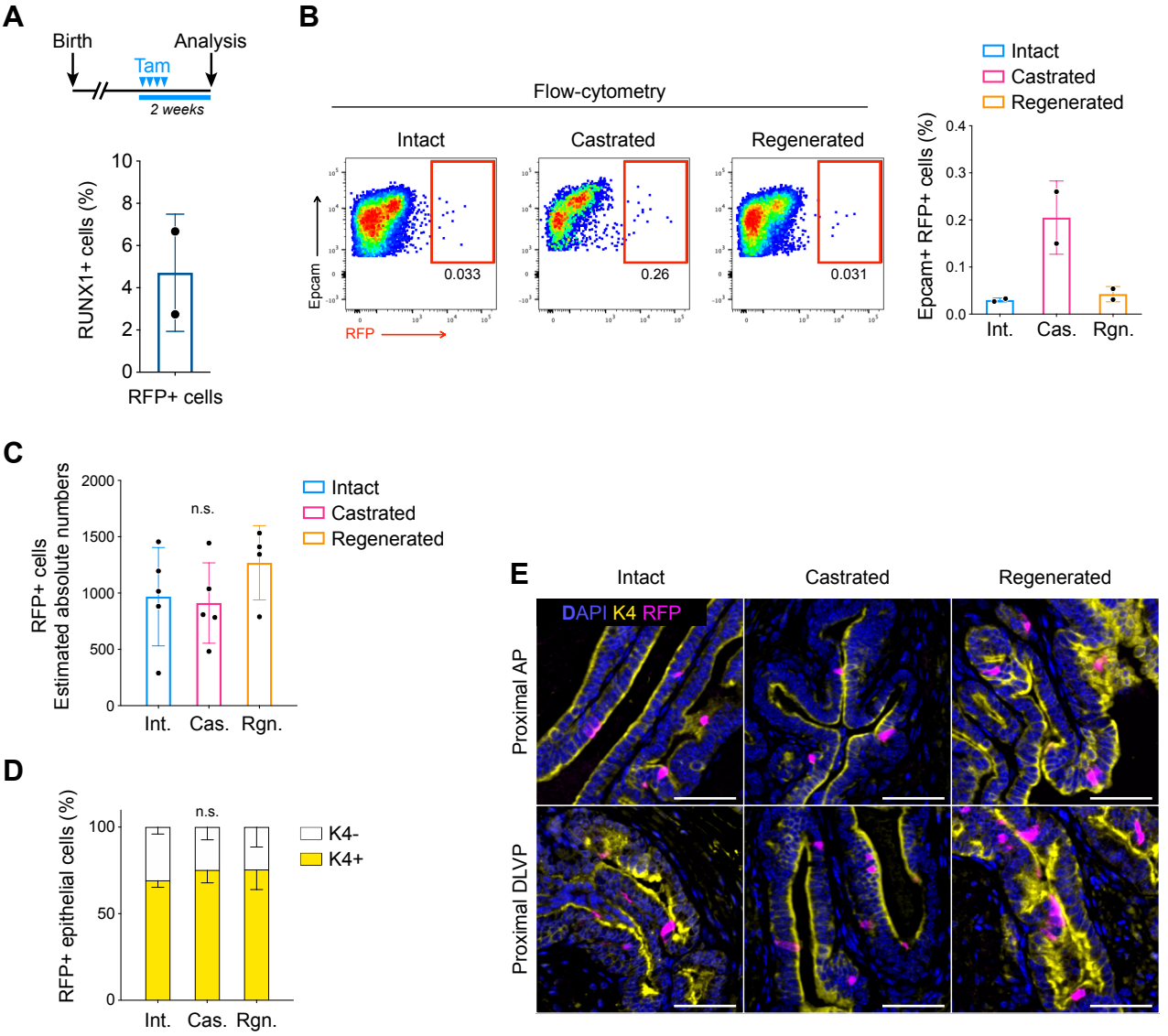
A
Birth
Analysis
Tam
2 weeks
RUNX1+ cells (%)
RFP+ cells
B
Flow-cytometry
Intact
Castrated
Regenerated
Epcam
RFP
0.033
0.26
0.031
Epcam+ RFP+ cells (%)
Int.
Cas.
Rgn.
C
RFP+ cells
Estimated absolute numbers
n.s.
D
RFP+ epithelial cells (%)
K4-
K4+
E
DAPI K4 RFP
Proximal AP
Proximal DLVP

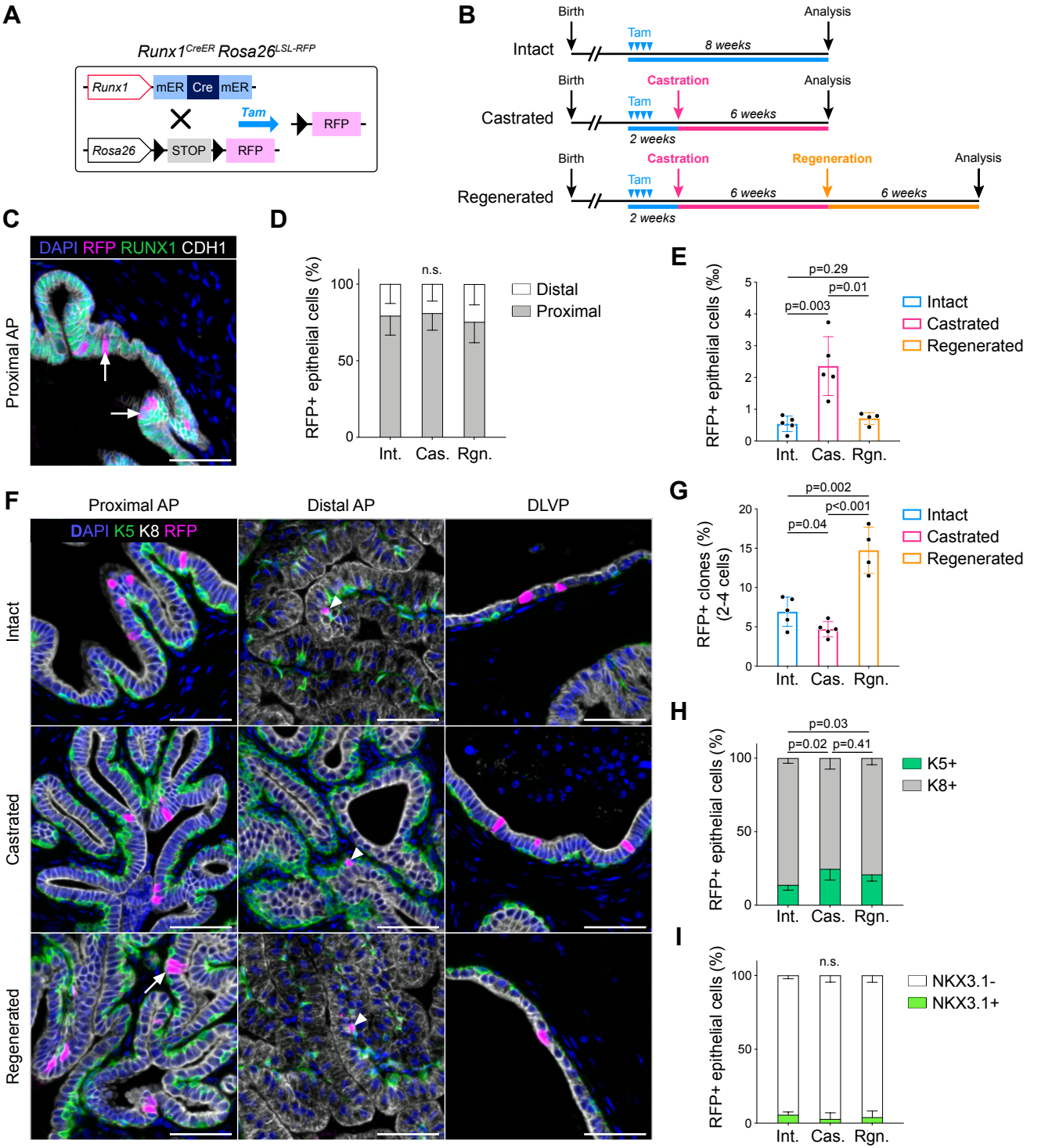
A
Runx1CreER Rosa26LSL-RFP
Runx1
mER
Cre
mER
Tam
RFP
Rosa26
STOP
RFP
B
Birth
Analysis
Intact
Tam
8 weeks
Castrated
Castration
6 weeks
2 weeks
Regenerated
Regeneration
6 weeks
6 weeks
2 weeks
C
DAPI RFP RUNX1 CDH1
Proximal AP
D
RFP+ epithelial cells (%)
n.s.
Distal
Proximal
Int. Cas. Rgn.
E
RFP+ epithelial cells (‰)
p=0.29
p=0.01
p=0.003
Intact
Castrated
Regenerated
Int. Cas. Rgn.
F
Proximal AP
Distal AP
DLVP
DAPI K5 K8 RFP
Intact
Castrated
Regenerated
G
RFP+ clones (%) (2-4 cells)
p=0.002
p<0.001
p=0.04
Intact
Castrated
Regenerated
Int. Cas. Rgn.
H
RFP+ epithelial cells (%)
p=0.03
p=0.02
p=0.41
K5+
K8+
Int. Cas. Rgn.
I
RFP+ epithelial cells (%)
n.s.
NKX3.1-
NKX3.1+
Int. Cas. Rgn.

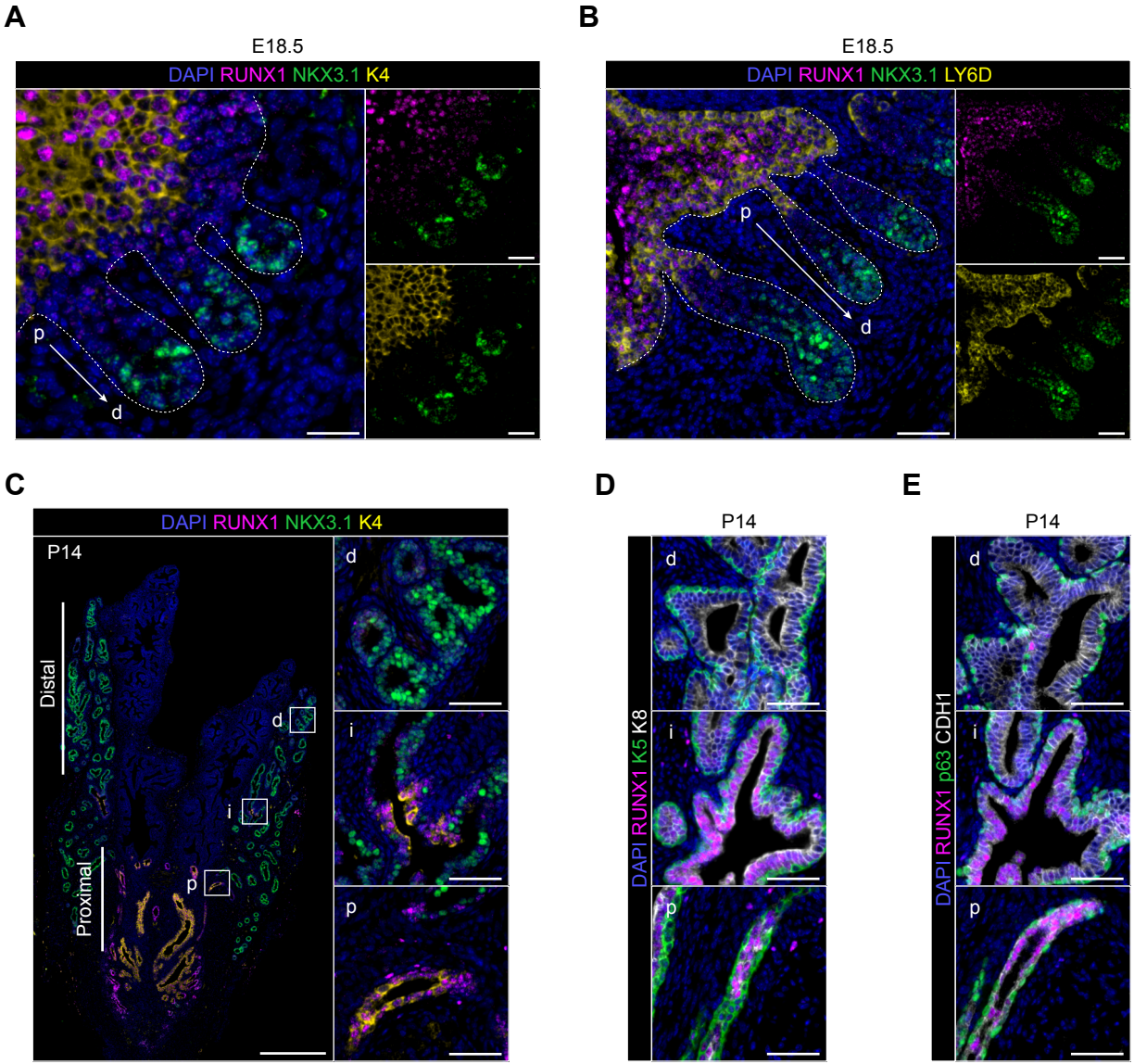
A
E18.5
DAPI RUNX1 NKX3.1 K4
p
d
B
E18.5
DAPI RUNX1 NKX3.1 LY6D
p
d
C
DAPI RUNX1 NKX3.1 K4
P14
Distal
Proximal
d
i
p
D
P14
DAPI RUNX1 K5 K8
d
i
p
E
P14
DAPI RUNX1 p63 CDH1
d
i
p

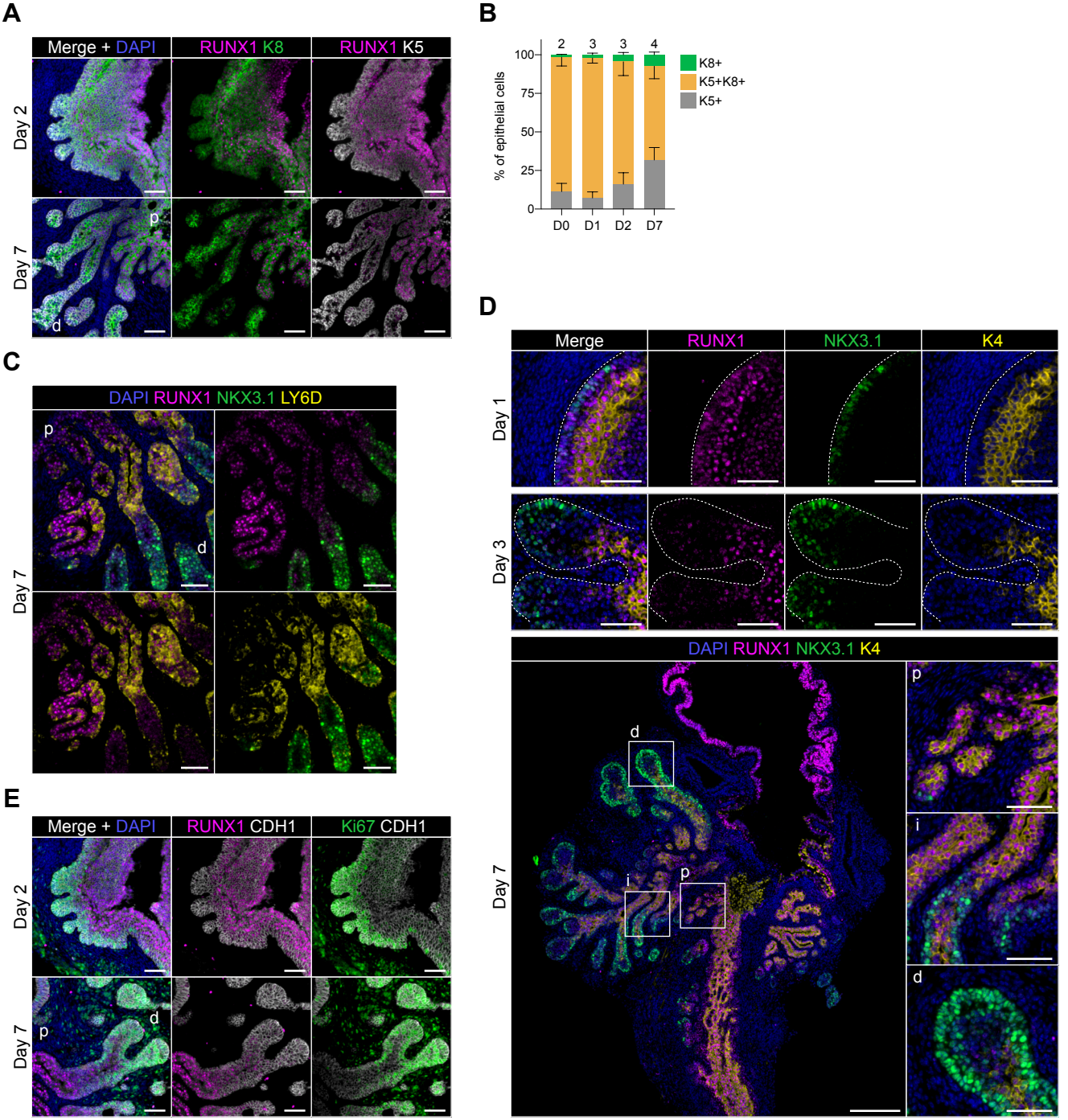
A
Merge + DAPI
RUNX1 K8
RUNX1 K5
Day 2
Day 7
p
d
B
% of epithelial cells
100
75
50
25
0
2
3
3
4
D0
D1
D2
D7
K8+
K5+K8+
K5+
C
DAPI RUNX1 NKX3.1 LY6D
Day 7
p
d
D
Merge
RUNX1
NKX3.1
K4
Day 1
Day 3
DAPI RUNX1 NKX3.1 K4
Day 7
d
i
p
E
Merge + DAPI
RUNX1 CDH1
Ki67 CDH1
Day 2
Day 7
p
d

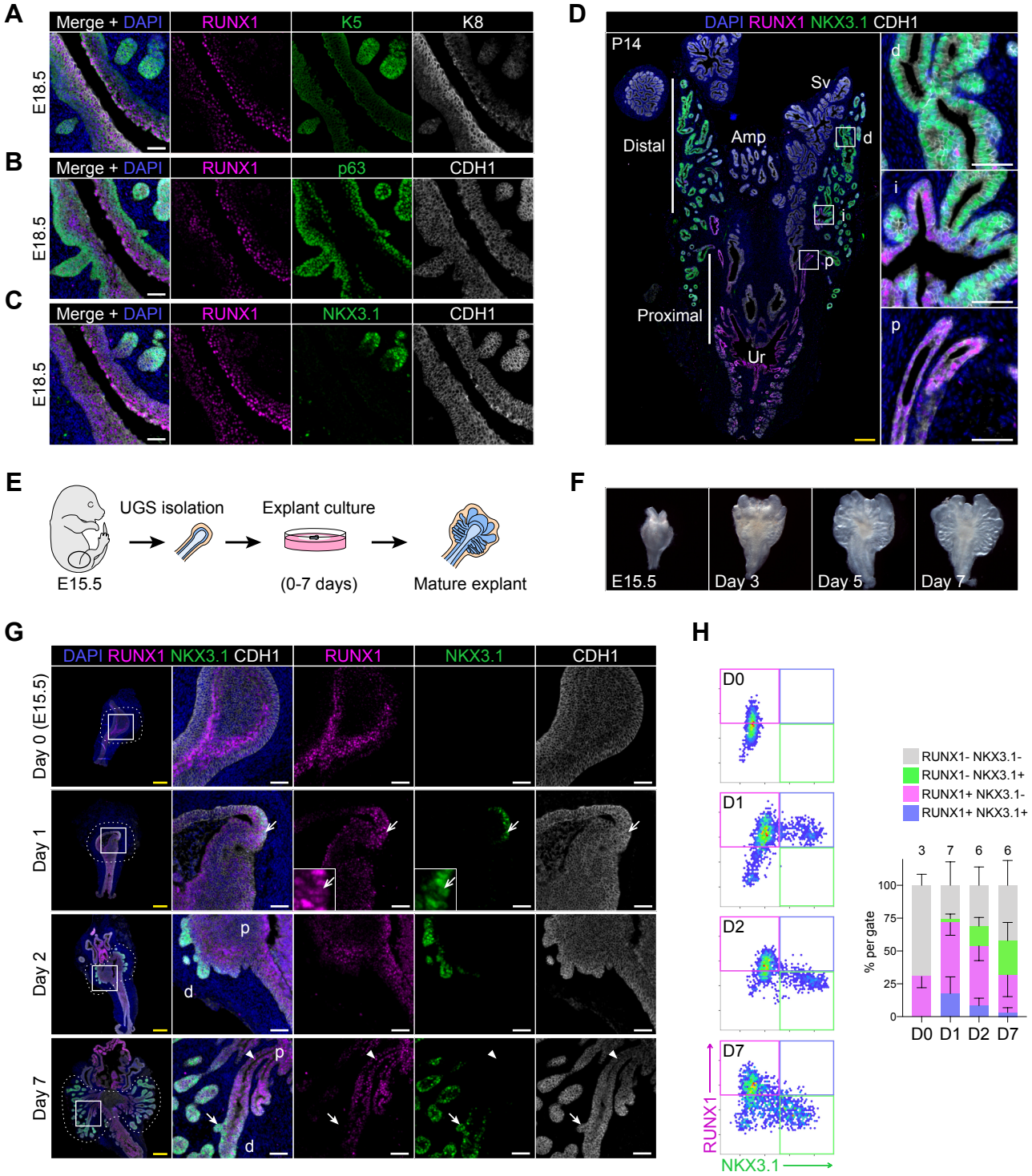
A
Merge + DAPI
RUNX1
K5
K8
E18.5
B
Merge + DAPI
RUNX1
p63
CDH1
E18.5
C
Merge + DAPI
RUNX1
NKX3.1
CDH1
E18.5
D
DAPI RUNX1 NKX3.1 CDH1
P14
Distal
Amp
Sv
d
i
p
Proximal
Ur
E
UGS isolation
Explant culture
E15.5
(0-7 days)
Mature explant
F
E15.5
Day 3
Day 5
Day 7
G
DAPI RUNX1 NKX3.1 CDH1
RUNX1
NKX3.1
CDH1
Day 0 (E15.5)
Day 1
Day 2
Day 7
p
d
H
D0
D1
D2
D7
RUNX1
NKX3.1
RUNX1- NKX3.1-
RUNX1- NKX3.1+
RUNX1+ NKX3.1-
RUNX1+ NKX3.1+
3
7
6
6
% per gate
100
75
50
25
0
D0 D1 D2 D7

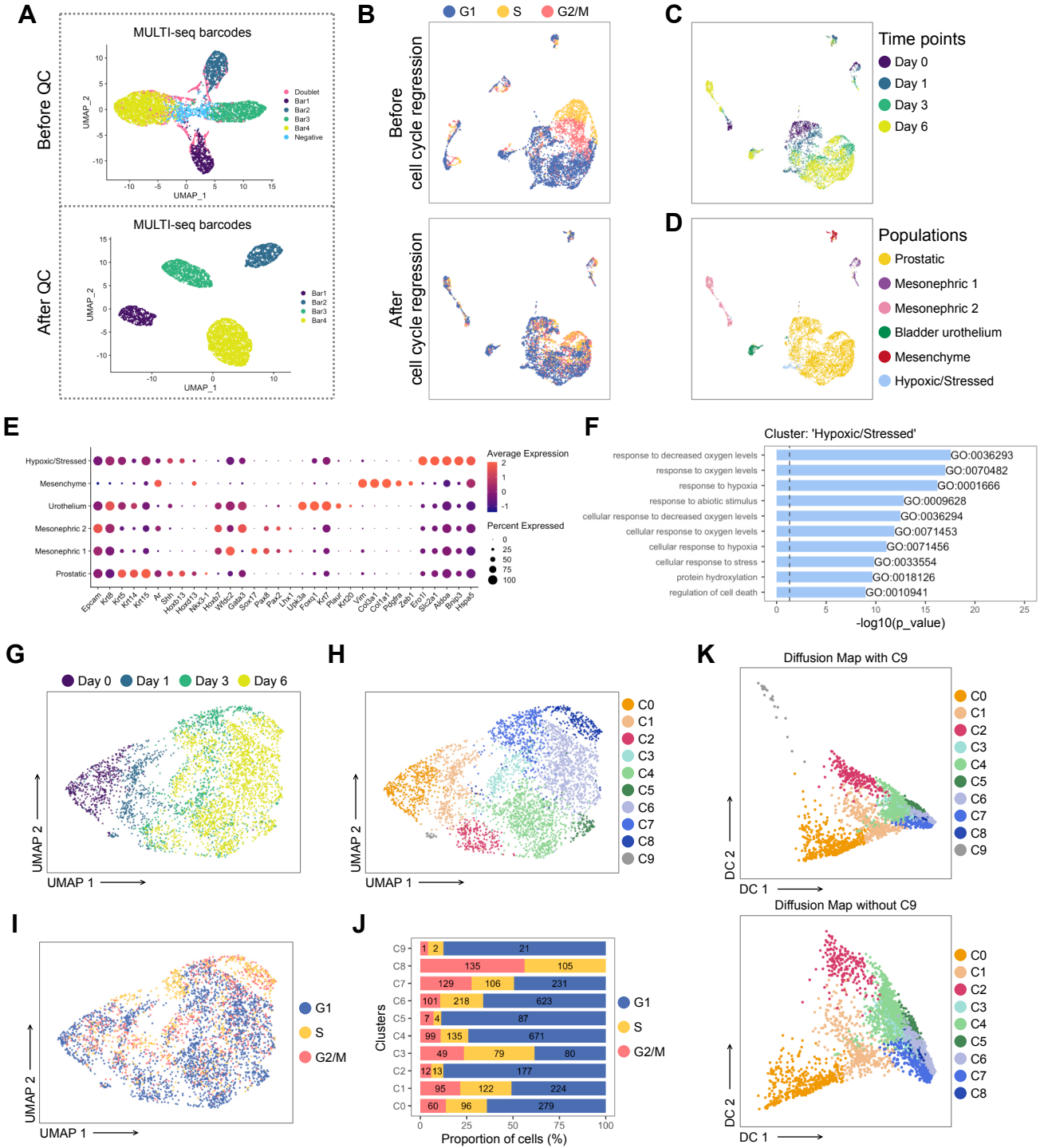
A
MULTI-seq barcodes
Before QC
After QC
UMAP_1
UMAP_2
Doublet
Bar1
Bar2
Bar3
Bar4
Negative
B
G1
S
G2/M
Before cell cycle regression
After cell cycle regression
C
Time points
Day 0
Day 1
Day 3
Day 6
D
Populations
Prostatic
Mesonephric 1
Mesonephric 2
Bladder urothelium
Mesenchyme
Hypoxic/Stressed
E
Hypoxic/Stressed
Mesenchyme
Urothelium
Mesonephric 2
Mesonephric 1
Prostatic
Epcam Krt8 Krt5 Krt14 Krt15 Ar Shh Hoxb13 Hoxd13 Nkx3-1 Hoxb7 Wldc2 Gata3 Gata3 Sox17 Pax8 Pax2 Lhx1 Upk3a Foxq1 Krt7 Plaur Krt20 Vim Col3a1 Col1a1 Pdgfra Zeb1 Ero1l Slc24a1 Aldoa Bnip3 Hspa8
Average Expression
Percent Expressed
F
Cluster: 'Hypoxic/Stressed'
response to decreased oxygen levels GO:0036293
response to oxygen levels GO:0070482
response to hypoxia GO:0001666
response to abiotic stimulus GO:0009628
cellular response to decreased oxygen levels GO:0036294
cellular response to oxygen levels GO:0071453
cellular response to hypoxia GO:0071456
cellular response to stress GO:0033554
protein hydroxylation GO:0018126
regulation of cell death GO:0010941
-log10(p_value)
G
Day 0
Day 1
Day 3
Day 6
UMAP 1
UMAP 2
H
C0
C1
C2
C3
C4
C5
C6
C7
C8
C9
K
Diffusion Map with C9
Diffusion Map without C9
DC 1
DC 2
I
G1
S
G2/M
J
Clusters
Proportion of cells (%)

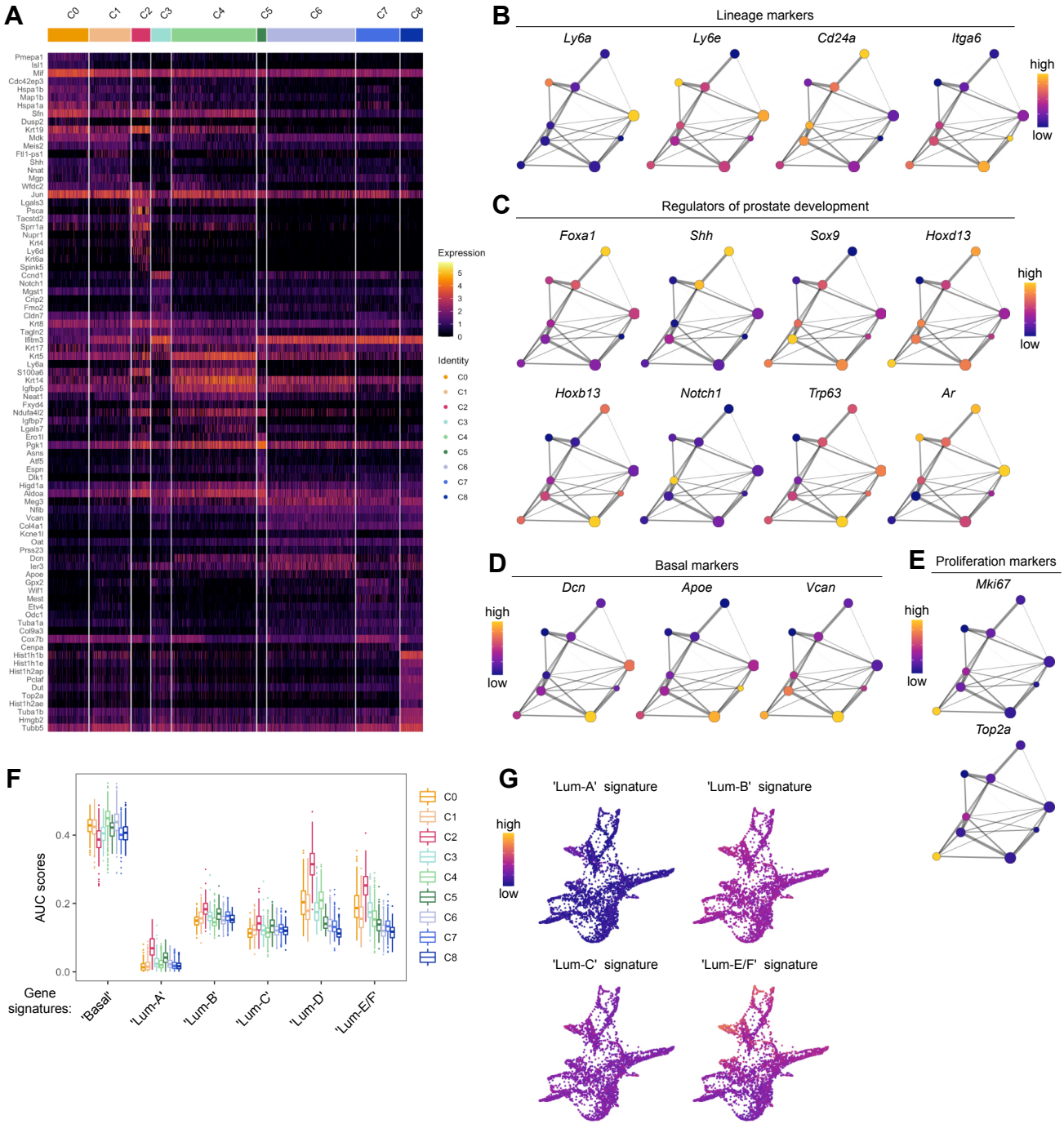
A
C0
C1
C2
C3
C4
C5
C6
C7
C8
Pmepa1
Isl1
Mif
Cdc42ep3
Hspa1b
Map1b
Hspa1a
Sfn
Dusp2
Krt19
Mdk
Meis2
Flt1-ps1
Shh
Ninal
Mgp
Wfdc2
Jun
Lgals3
Psca
Tacstd2
Sprr1a
Nupr1
Krt4
Ly6d
Krt6a
Spink5
Ccnd1
Notch1
Mgst1
Crip2
Fmo2
Cldn7
Krt8
Tagln2
Ifitm3
Krt17
Krt5
Ly6a
S100a6
Krt14
Igfbp5
Neat1
Fxyd4
Ndufa4l2
Igfbp7
Lgals7
Ero1l
Pgk1
Asns
Atf5
Espn
Dlk1
Higd1a
Aldoa
Meg3
Nfib
Vcan
Col4a1
Kcne1l
Oat
Prss23
Dcn
Ier3
Apoe
Gpx2
Wif1
Mest
Etv4
Odc1
Tuba1a
Col9a3
Cox7b
Cenpa
Hist1h1b
Hist1h1e
Hist1h2ap
Pclaf
Dut
Top2a
Hist1h2ae
Tuba1b
Hmgb2
Tubb5
Expression
5
4
3
2
1
0
Identity
C0
C1
C2
C3
C4
C5
C6
C7
C8
B
Lineage markers
Ly6a
Ly6e
Cd24a
Itga6
high
low
C
Regulators of prostate development
Foxa1
Shh
Sox9
Hoxd13
Hoxb13
Notch1
Trp63
Ar
high
low
D
Basal markers
Dcn
Apoe
Vcan
high
low
E
Proliferation markers
Mki67
Top2a
high
low
F
AUC scores
0.0
0.2
0.4
Gene signatures:
'Basal'
'Lum-A'
'Lum-B'
'Lum-C'
'Lum-D'
'Lum-E/F'
C0
C1
C2
C3
C4
C5
C6
C7
C8
G
'Lum-A' signature
'Lum-B' signature
'Lum-C' signature
'Lum-E/F' signature
high
low

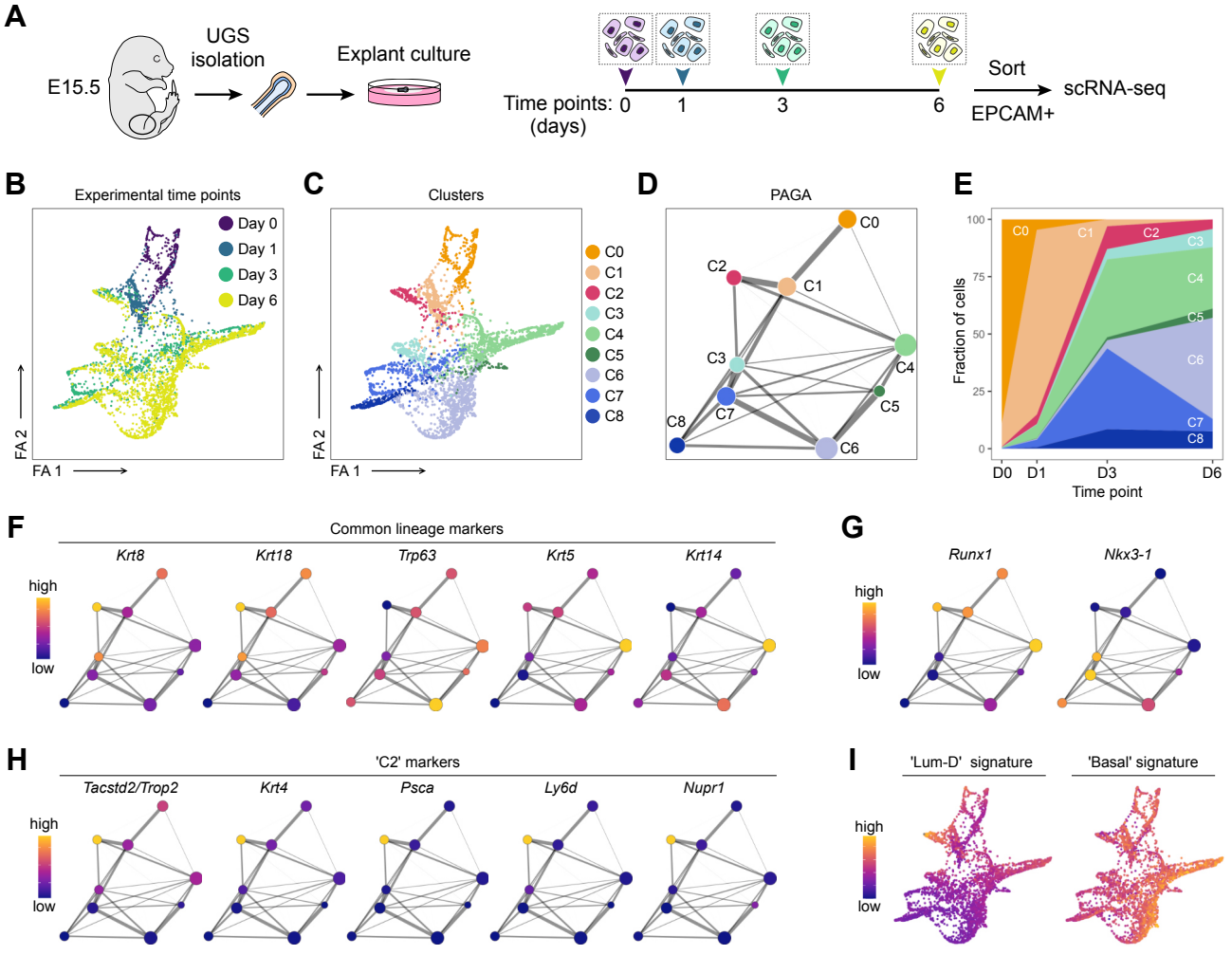
A
E15.5
UGS isolation
Explant culture
Time points: (days)
0
1
3
6
Sort
EPCAM+
scRNA-seq
B
Experimental time points
Day 0
Day 1
Day 3
Day 6
FA 1
FA 2
C
Clusters
C0
C1
C2
C3
C4
C5
C6
C7
C8
FA 1
FA 2
D
PAGA
C0
C1
C2
C3
C4
C5
C6
C7
C8
E
Fraction of cells
100
75
50
25
0
C0
C1
C2
C3
C4
C5
C6
C7
C8
D0
D1
D3
D6
Time point
F
Common lineage markers
Krt8
Krt18
Trp63
Krt5
Krt14
high
low
G
Runx1
Nkx3-1
high
low
H
'C2' markers
Tacstd2/Trop2
Krt4
Psca
Ly6d
Nupr1
high
low
I
'Lum-D' signature
'Basal' signature
high
low

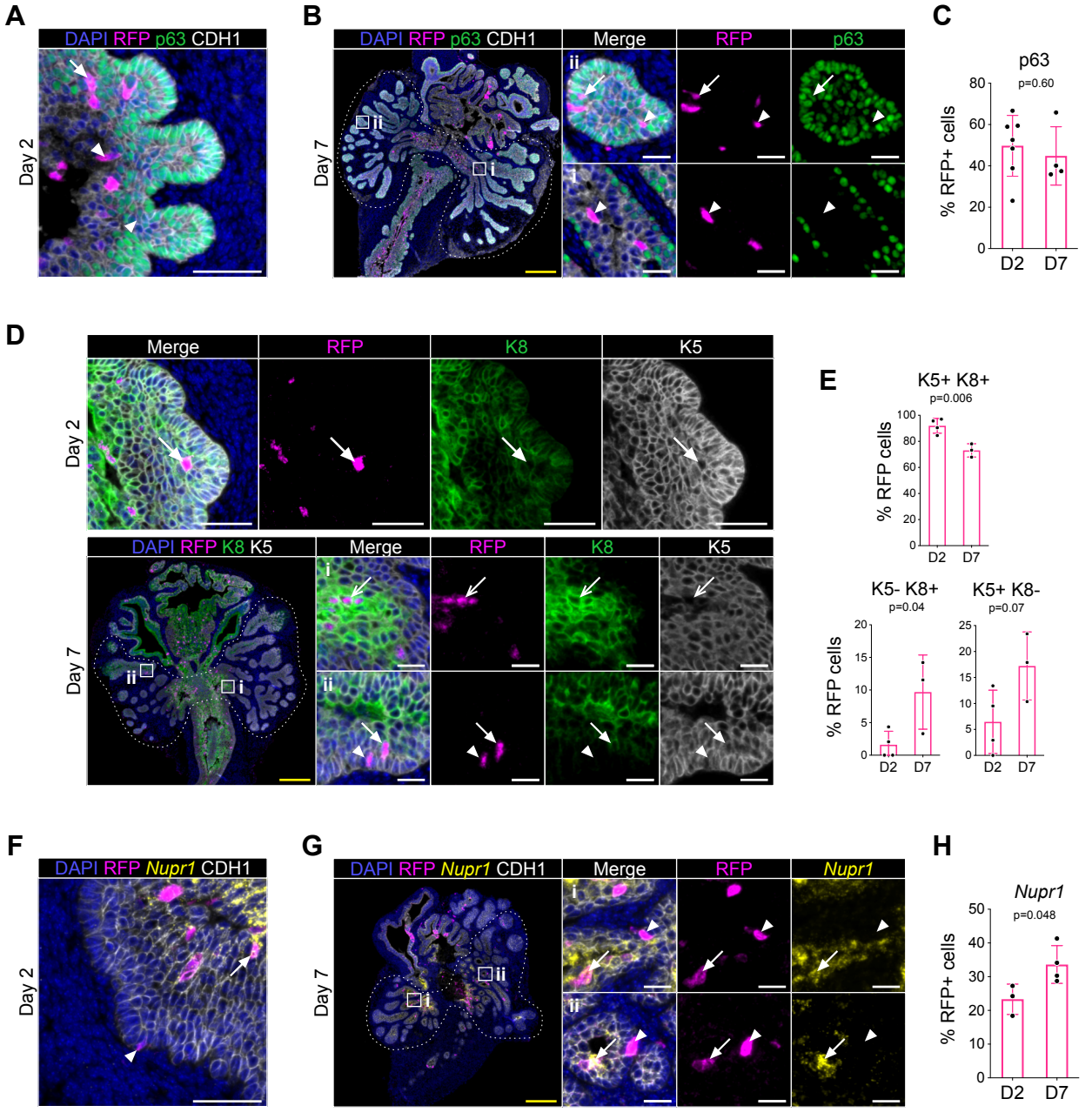
A
DAPI RFP p63 CDH1
Day 2
B
DAPI RFP p63 CDH1
Merge
RFP
p63
Day 7
ii
i
C
p63
p=0.60
% RFP+ cells
80
60
40
20
0
D2
D7
D
Merge
RFP
K8
K5
Day 2
DAPI RFP K8 K5
Merge
RFP
K8
K5
Day 7
ii
i
E
K5+ K8+
p=0.006
% RFP cells
100
80
60
40
20
0
D2
D7
K5- K8+
p=0.04
K5+ K8-
p=0.07
% RFP cells
20
15
10
5
0
25
20
15
10
5
0
D2
D7
F
DAPI RFP Nupr1 CDH1
Day 2
G
DAPI RFP Nupr1 CDH1
Merge
RFP
Nupr1
Day 7
i
ii
H
Nupr1
p=0.048
% RFP+ cells
50
40
30
20
10
0
D2
D7

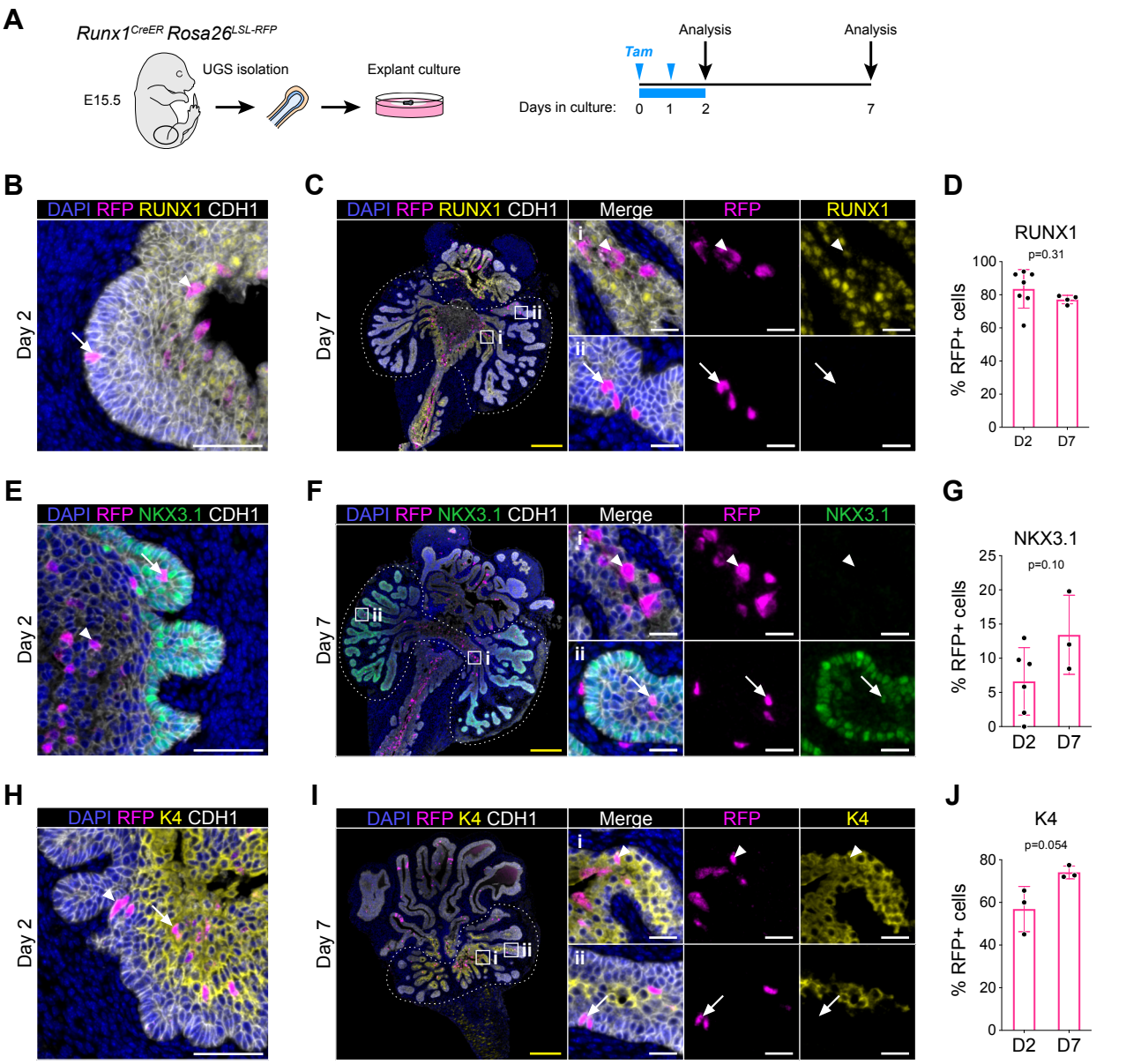
A
Runx1CreER Rosa26LSL-RFP
E15.5
UGS isolation
Explant culture
Tam
Analysis
Analysis
Days in culture:
0
1
2
7
B
DAPI RFP RUNX1 CDH1
Day 2
C
DAPI RFP RUNX1 CDH1
Merge
RFP
RUNX1
Day 7
i
ii
D
RUNX1
p=0.31
% RFP+ cells
D2
D7
E
DAPI RFP NKX3.1 CDH1
Day 2
F
DAPI RFP NKX3.1 CDH1
Merge
RFP
NKX3.1
Day 7
G
NKX3.1
p=0.10
% RFP+ cells
D2
D7
H
DAPI RFP K4 CDH1
Day 2
I
DAPI RFP K4 CDH1
Merge
RFP
K4
Day 7
J
K4
p=0.054
% RFP+ cells
D2
D7